Asymmetrische SQUIDs und nanoSQUIDs: Quanteninterferometer unter neuartigen Bedingungen

Dissertation
der Mathematisch-Naturwissenschaftlichen Fakultät
der Eberhard Karls Universität Tübingen
zur Erlangung des Grades eines
Doktors der Naturwissenschaften
(Dr.rer.nat.)

vorgelegt von
Joachim Nagel
aus Heidenheim

Tübingen
2012

Tag der mündlichen Qualifikation:	6. September 2012
Dekan:	Prof. Dr. Wolfgang Rosenstiel
1. Berichterstatter	Prof. Dr. Dieter Kölle
2. Berichterstatter	Prof. Dr. Reinhold Kleiner

Abstract

The development of nano-sized direct current (dc) superconducting quantum interference devices (SQUIDs) is an intensive field of research, driven by the need for sensitive measurement techniques for the investigation of small spin systems ranging from the mTesla up to the Tesla range. This work gives a contribution to this field. Both low-T_c (T_c is the transition temperature) SQUIDs and gradiometers based on Nb/HfTi/Nb superconductor/ normal metal/ superconductor (SNS) type Josephson junctions and high-T_c dc SQUIDs based on $YBa_2Cu_3O_7$ (YBCO) grain boundary junctions (GBJs) have been investigated. Since the rms spin sensitivity $S_\mu^{1/2}$ can be optimized by nano-patterning of the SQUIDs, advanced patterning techniques, i.e., electron-beam lithography and focused ion beam milling have been used in order to reduce the size of the SQUIDs, yielding linewidths well below $1\,\mu$m. For both types of SQUIDs we implemented a galvanically coupled coil, where part of the SQUID loop is used to apply a magnetic flux without the need of an external coil.

The SQUIDs have been characterized with respect to their transport and noise characteristics at temperature $T = 4.2\,\mathrm{K}$. In low magnetic fields ($\leq 1\,\mathrm{mT}$), for the SNS type SQUIDs, a flux noise $S_\Phi^{1/2} = 250\,\mathrm{n}\Phi_0/\mathrm{Hz}^{1/2}$ in the white noise regime and a maximum coupling factor $\phi_\mu \sim 8.5\,\mathrm{n}\Phi_0/\mu_\mathrm{B}$, calculated by a new method developed in this work, yielding a spin sensitivity $S_\mu^{1/2} = 29\,\mu_B/\mathrm{Hz}^{1/2}$, was achieved. We demonstrated the reliable operation of such SQUIDs in magnetic fields up to $\sim 50\,\mathrm{mT}$. For higher fields we observed jumps in the voltage across the SQUID, which prevented a reliable operation. By combining the nanoSQUID with a low-temperature magnetic force microscope (LTMFM), we were able to correlate the jumps with the entrance of Abrikosov vortices into the superconducting leads of the SQUID. With this combined setup of a LTMFM and the nanoSQUID, for the first time we were able to measure the magnetic coupling $\Phi_\mu(\vec{r})$ between the magnetic moment $\vec{\mu}$ of a nano-magnet, i.e. a Ni nano-tube, and the SQUID loop as a function of the position $\vec{r}$ of the nano-tube. The results of this experiment were in good agreement with the numerical calculations of $\Phi(\vec{r})$ based on the London equations.

For the YBCO nanoSQUIDs we developed a fabrication technique based focused ion beam milling, capable to pattern GBJs with a width below 100 nm without significant degradation of the critical current density j_c. The first generation of such nanoSQUIDs had a good $S_\Phi^{1/2} = 4\,\mu\Phi_0/\mathrm{Hz}^{1/2}$ and maximum $\phi_\mu \approx 10\,\mathrm{n}\Phi_0/\mu_\mathrm{B}$, yielding a rms spin sensitivity $S_\mu^{1/2} = 390\,\mu_B/\mathrm{Hz}^{1/2}$ at low magnetic fields. Subsequently improved SQUIDs with an galvanically coupled coil yielded $S_\mu^{1/2} = 62\,\mu_B/\mathrm{Hz}^{1/2}$ in

low magnetic fields and only slightly reduced $S_\mu^{1/2} = 110\,\mu_B/\mathrm{Hz}^{1/2}$ even at high magnetic fields up to $\mu_0 H = 1\,\mathrm{T}$.

In parallel to the investigation of nanoSQUIDs, a second approach in order to improve the sensitivity of SQUIDs has been investigated. Numerical simulations revealed that a significant improvement of $S_\Phi^{1/2}$ up to a factor of 3 can be achieved by strong asymmetries in the resistance of the two Josephson junctions of a dc SQUID. The theoretical predictions have been investigated experimentally with SQUIDs based on a Nb/Al-AlO_x/Nb trilayer fabrication process using a combination of photolithography and Ar ion etching. An asymmetric SQUID where one junction was shunted with an external resistor R_{shunt} and the other junction was unshunted and a corresponding symmetric SQUID have been measured with respect to their transport and noise properties at $T = 4.2\,\mathrm{K}$. The results of these measurements were in very good agreement with numerical simulation, confirming an improvement of $S_\Phi^{1/2}$ by a factor of ~ 3 due to the resistance asymmetry. For nanoSQUIDs, this approach could further improve the spin sensitivity beyond technological and physical limitations of the miniaturization.

Kurzfassung

Die Entwicklung von dc SQUIDs mit Abmessungen auf der nanometer Skala ist ein aktives Feld der Forschung, getrieben durch die Notwendigkeit sensitiver Messmethoden für die Untersuchung von kleinen Spinsystemen in niedrigen und hohen Magnetfeldern im Bereich von mTesla bis Tesla. Diese Arbeit leistet einen Beitrag zu diesem Feld. Niedertemperatur dc SQUIDs und Gradiometer, basierend auf Nb/HfTi/Nb Supraleiter/normal leitendes Metall/Supraleiter (SNS) Josephson Kontakten und Hochtemperatur SQUIDs mit $YBa_2Cu_3O_7$ (YBCO) Korngrenzenkontakten wurden untersucht. Da die Spinsensitivität $S_\mu^{1/2}$ durch Mikro- und Nanostrukturierung der SQUIDs optimiert werden kann, wurden anspruchsvolle Strukturierungsmethoden wie Elektronenstrahl Lithographie und fokussiertes Ionenstrahl ätzen verwendet, um die Linienbreiten der SQUIDs unter $1\,\mu$m zu reduzieren. Für beide Arten von SQUIDs konnte eine galvanisch gekoppelte Spule implementiert werden, für die ein Teil des SQUID Rings für das Anlegen eines magnetischen Flusses verwendet wird, wodurch eine externe Spule eingespart werden kann.

Die SQUIDs wurden bezüglich ihrer Transport- und Rauscheigenschaften bei einer Temperatur von 4.2 K untersucht. In niedrigen Magnetfeldern ($\leq 1\,$mT) wurde für die SNS SQUIDs ein Flussrauschen $S_\Phi^{1/2} = 250\,\mathrm{n}\Phi_0/\mathrm{Hz}^{1/2}$ im Bereich weißen Rauschens, ein mit einer im Rahmen dieser Arbeit entwickelten Methode berechneter maximaler Kopplungsfaktor $\phi_\mu \sim 8.5\,\mathrm{n}\Phi_0/\mu_\mathrm{B}$ und eine daraus resultierend rms Spinsensitivität von $S_\mu^{1/2} = 29\,\mu_B/\mathrm{Hz}^{1/2}$ erreicht. Die SQUIDs wurden in Magnetfeldern bis zu $\sim 50\,$mT betrieben. Für höhere Felder traten Sprünge in der Spannung über das SQUID auf, wodurch eine zuverlässige Funktionsweise nicht mehr gegeben war. Durch die Kombination eines nanoSQUIDs und eines Tieftemperatur-Magnetischen-Kraft-Mikroskops (TTMKM) konnten diese Sprünge mit dem Eindringen von Abrikosov Vortices in die supraleitenden Zuleitungen des SQUIDs korreliert werden. In diesem kombinierten System bestehend aus TTMKM und nanoSQUID konnten wir erstmalig die magnetische Kopplung $\Phi_\mu(\vec{r})$ zwischen dem magnetischen Moment $\vec{\mu}$ eines Nanomagneten, in unserem Fall ein Ni Nanoröhrchen, und des SQUID Rings in Abhängigkeit von der Position $\vec{r}$ des Nanoröhrchens vermessen. Die Ergebnisse dieses Experiments waren in guter Übereinstimmung mit den numerischen Berechnungen von $\Phi_\mu(\vec{r})$, denen die London Gleichungen zugrunde liegen.

Für YBCO nanoSQUIDs entwickelten wir eine Fabrikationsmethode, die es ermöglicht Korngrenzenkontakte mit einer Breite kleiner als 100 nm ohne signifikante Degradation der kritischen Stromdichte j_c herzustellen. Die erste Generation solcher nanoSQUIDs zeigte ein gutes Flussrauschen $S_\Phi^{1/2} = 4\,\mu\Phi_0/\mathrm{Hz}^{1/2}$ in niederen Mag-

netfeldern und ein maximales $\phi_\mu \approx 10\,\mathrm{n}\Phi_0/\mu_\mathrm{B}$, woraus sich eine Spinsensitivität $S_\mu^{1/2} = 390\,\mu_B/\mathrm{Hz}^{1/2}$ ergab. Für nachfolgende, verbesserte SQUIDs bei denen eine galvanisch gekoppelte Spule integriert wurde, ergab sich $S_\mu^{1/2} = 62\,\mu_B/\mathrm{Hz}^{1/2}$ in niederen Magnetfeldern und in Magnetfeldern bis $\mu_0 H = 1\,\mathrm{T}$ ein nur leicht degradiertes $S_\mu^{1/2} = 110\,\mu_B/\mathrm{Hz}^{1/2}$.

Parallel zu den Untersuchungen an nanoSQUIDs wurde ein zweiter Ansatz zur Verbesserung der Sensitivität von SQUIDs untersucht. Numerische Simulationen haben gezeigt, dass eine signifikante Verbesserung um einen Faktor 2 des rms Flussrauschens $S_\Phi^{1/2}$ durch starke Asymmetrien in den Widerständen der Josephson Kontakte eines dc SQUIDs erreicht werden kann. Diese theoretischen Vorhersagen wurden experimentell an SQUIDs untersucht, die basierend auf einer Nb/Al-AlO_x/Nb Trilagen-Technologie mittels einer Kombination von Photolithographie und Argon Ionenätzen hergestellt wurden. Es wurden Messungen bezüglich der Transpot- und Rauscheigenschaften an einem asymmetrischen SQUID (bei dem nur einer der Josephson Kontakte mit einem externen Widerstand R_shunt parallel geschaltet wurde) und dem entsprechenden symmetrische SQUID bei einer Temperatur von $T = 4.2\,\mathrm{K}$ durchgeführt. Die Ergebnisse dieser Messungen waren in sehr guter Übereinstimmungen mit den numerischen Simulationen und bestätigten eine Verbesserung von $S_\Phi^{1/2}$ um einen Faktor ~ 3 aufgrund der Asymmetrie im Widerstand. Für nanoSQUIDs könnte dadurch eine weitere Verbesserung der Spinsensitivität erreicht werden, die über die technologischen und physikalischen Einschränkungen der Miniaturisierung hinausgeht.

List of publications

The publications of this cumulative thesis are listed below. The publications are attached at the very end of the thesis. Publications 1-5 are summarized in chapter 2, publications 6 and 7 are not included in this cumulative thesis.

Appended publications

Published:

Publication 1 **J. Nagel**, K.B. Konovalenko, M. Kemmler, M. Turad, R. Werner, E. Kleisz, S. Menzel, R. Klingeler, B. Büchner, R. Kleiner, and D. Koelle,
Resistively shunted $YBa_2Cu_3O_7$ grain boundary junctions and low-noise SQUIDs patterned by a focused ion beam down to 80 nm linewidth,
Supercond. Sci. Technol. **24**, 015015, 2011

Publication 2 **J. Nagel**, O.F. Kieler, T. Weimann, R. Wölbing, J.Kohlmann, A.B. Zorin, R. Kleiner, D. Koelle, and M. Kemmler,
Superconducting quantum interference devices with submicron Nb/HfTi/Nb junctions for investigation of small magnetic particles,
Appl. Phys. Lett. **99**, 032506, 2011

Publication 3 M. Rudolph, **J. Nagel**, J.M. Meckbach, M. Kemmler, M. Siegel, K.Ilin, D. Koelle, and R. Kleiner,
Direct current superconducting quantum interferometers with asymmetric shunt resistors,
Appl. Phys. Lett. **101**, 052602, 2012

Close to submission:

Publication 4 **J. Nagel**, A. Buchter, F. Xue, O.F. Kieler, T. Weimann, J. Kohlmann, A. B. Zorin, D. Rüffer, E. Russo-Averchi, R. Huber, P. Berberich, A. Fontcuberta i Morral, D. Grundler, R. Kleiner, D. Koelle, M. Poggio, and M. Kemmler,
Nanoscale multifunctional sensor formed by a Ni nanotube and a scanning Nb nanoSQUID,
unpublished, 2012

Publication 5 T. Schwarz, **J. Nagel**, R. Wölbing, R. Kleiner, D. Koelle, and M. Kemmler,
Low-noise nanoSQUIDs operating in Tesla magnetic fields — towards detection of small spin systems with single-spin resolution,
unpublished, 2012

Publications not included in this thesis

Publication 6 J. Tomaschko, V. Leca, **J. Nagel**, T. Selistrovski, R. Kleiner, and D. Koelle,
Phase-sensitive evidence for $d_{x^2-y^2}$-pairing symmetry in the parent-structure high-T_c cuprate superconductor $Sr_{1-x}La_xCuO_2$,
submitted to Phys. Rev. Lett., arXiv:1203.5237, 2012

Publication 7 P. Bushev, D. Bothner, **J. Nagel**, M. Kemmler, K.B. Konovalenko, A. Lörincz, K. Ilin, M. Siegel, D. Koelle, R. Kleiner, and F. Schmidt-Kaler,
Trapped electron coupled to superconducting devices,
Eur. Phys. J. D **63**, 9–16, 2011

Contents

Introduction

Ever since the pioneering work of Frenkel and Dorfman in 1930 [1] predicting a single domain behaviour of small ferromagnetic samples and the more detailed analysis of Stoner and Wohlfarth in 1948 [2] and Neel in 1949 [3], there has been a continuous interest in the experimental investigation of small magnetic particles (SMPs). Morrish and Yu confirmed these theories in 1956 by direct measurement of single domain switching in a micron-sized $\gamma - Fe_2O_3$ sample using a quartz-fiber torsion balance [4]. The huge influence of these theories for todays understanding of magnetism emphasizes the importance of experiments to confirm such theories. Since that time, continuous progress of theoretical concepts, the discovery of new materials as well as improved fabrication techniques for SMPs demand for constant improvements of the sensitivity of such measurements. A currently very active field of research for instance is the investigation of single-molecule or single chain magnets [5, 6, 7]. Even macroscopic sized crystals made of such molecules show at low temperatures $\leq 5\,\mathrm{K}$ and magnetic fields of $\approx 1\,\mathrm{T}$ quantum tunneling of the magnetization. This remarkable property has for instance been proposed to offer an opportunity to test the Copenhagen interpretation of quantum mechanics by investigation of the transition between small particles described only by quantum mechanics to macroscopic objects with purely classical properties [6]. Besides such fundamental research, many applications for SMPs have been proposed like quantum computing, spintronic devices or high density storage devices.

Nowadays besides various types of detection methods like Kerr effect [8], Lorentz microscopy [9], magneto-optic spin detection [10, 11] or scanning-tunneling-microscopy-assisted electron-spin resonance [12, 13], most frequently magnetic (resonance) force microscopy (M(R)FM) [14, 15, 16] is used for the investigation of SMPs. Despite the striking sensitivity and spatial resolution of MRFM (even single spin detection has been demonstrated [16]), with this spectroscopic measurement technique no hysteresis curves of the magnetization of SMPs can be beasured. For such measurements, two well known magnetic field sensor types namely Hall bars [17, 18, 19] and superconducting quantum interference devices (SQUIDs) [20, 21, 22, 23] have been adapted. Even though both sensor types have been used for measurements of SMPs, up to now the ultimate goal of single spin detection has not been demonstrated. The aim of this work was the investigation and optimization of direct current (dc) nanoSQUIDs in order to improve their minimum spin resolution under the restriction of operation in high magnetic fields. Up to now, most of the SQUIDs have been optimized for the detection of homogeneous magnetic fields, usually in a magnetically and electrically shielded environment with residual fields well below

the earth magnetic field. In contrast, the novel application of measurements on SMP often demands for highly sensitive sensors, capable to detect the spatially confined dipole field of a very small number of spins in huge magnetic fields up to the Tesla range. These highly unfavorable conditions pose a major challenge for the design, the fabrication process and the materials used for this new species of SQUIDs. In the following, the main requirements and our approaches how to account for them are summarized.

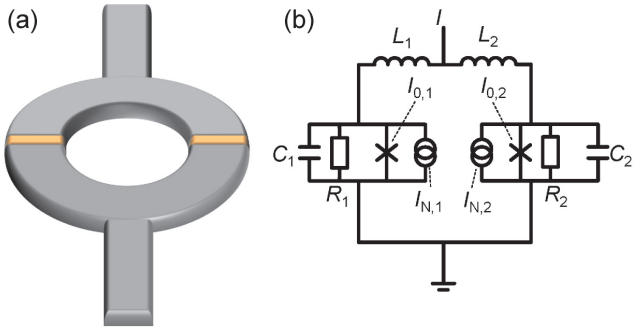

Figure 0.1: (a) Schematic drawing of a dc SQUID; Josephson junctions are indicated by orange structures. (b) Equivalent circuit of a dc SQUID (crosses indicate the tunnel junctions) with $R_{1(2)}$ the resistance, $C_{1(2)}$ the capacitance, $I_{0,1(2)}$ the critical current and $I_{N,1(2)}$ the noise current of Josephson junction 1(2). $L_{1(2)}$ is the inductance of the SQUID arms.

A dc SQUID consists of two Josephson junctions (JJs) [24] embedded into a superconducting ring (see Fig. 0.1(a)). Since the voltage drop across such a device depends strongly on the amount of magnetic flux inside the ring, SQUIDs are well suited for the detection of magnetic fields. In fact they are the most sensitive sensors for changes of magnetic flux available at the time of writing. In principle, SQUIDs are capable to detect any quantity, that can be transformed into magnetic flux, which is why the most common application for SQUIDs (besides measurement of magnetic fields) is low-noise amplification of small voltages. The sensitivity of a SQUID is given by the root mean square (rms) flux noise $S_\Phi^{1/2}$ which limits the minimum detectable change of flux inside the SQUID loop for 1 s of measurement time. State of the art for a commercially available SQUID is $S_\Phi^{1/2} \approx 1\,\mu\Phi_0/\mathrm{Hz}^{1/2}$, with $\Phi_0 \approx 2.07 \times 10^{-15}\mathrm{Tm}^2$ the magnetic flux quantum [25]. Since the quantity to be measured with a nanoSQUID is no longer a homogeneous magnetic field but a dipole field of a nanometer sized magnetic sample, the sensitivity is not only limited by $S_\Phi^{1/2}$ only, but also by the amount of flux Φ coupled to the nanoSQUID loop by a SMP [26], which is given by the coupling factor $\phi_\mu = \Phi/\mu$, with μ the magnetic moment of a point-like magnetic moment. Therefore the figure of merit for nanoSQUIDs is the spin sensitivity $S_\mu^{1/2} = S_\Phi^{1/2}/\phi_\mu$, usually given in units of

$\mu_B/\mathrm{Hz}^{1/2}$, with $\mu_B = 9.274 \times 10^{-24}\,\mathrm{J/T}$ the Bohr magneton. In order to improve $S_\mu^{1/2}$ one has to optimize both, $S_\Phi^{1/2}$ **and** ϕ_μ.

Within the resitively and capacetively shunted junction (RCSJ) model [27] (see Fig. 0.1(b)), the dependence of $S_\Phi^{1/2}$ on the electrical and geometrical properties of a symmetric SQUID ($I_{0,1} = I_{0,2} = I_0$, $R_1 = R_2 = R$, $C_1 = C_2 = C$ and $L_1 = L_2 = L/2$) in the limit of small thermal fluctuations $\Gamma \equiv 2\pi k_B T/I_0\Phi_0 \ll 1$ (i.e. high critical current I_0, low temperature T and small inductance L, $k_B \approx 1.38\times10^{-23}\,\mathrm{J/K}$ is the Boltzmann constant) is well described by [27]:

$$S_\Phi^{1/2} = (4(1 + 2I_0L/\Phi_0)k_BTL\Phi_0/(I_0R))^{1/2}. \tag{0.1}$$

According to Eq. 0.1, $S_\Phi^{1/2}$ can be reduced by minimizing L, by lowering T, and by maximizing the characteristic voltage $V_c = I_0R$. While the optimization of V_c can be done for virtually any SQUID by optimizing the junction properties (I_0, R), the minimization of L demands for nano-patterning of the SQUID loop and therefore for nanoSQUIDs. Even though the reduction of the SQUID inductance is very effective for the optimization of $S_\Phi^{1/2}$, there are two limitations which have to be considered. First, due to topological reasons, the junction size limits the linewidth of the loop at the position of the JJs. In order to provide sufficiently high critical currents of the SQUID, high current densities of the JJs are needed. Second, besides technological limitations, with a reduction of the linewidth of the loop below the London penetration depth λ_L the gain in reduced geometric inductance will be destroyed by a significant increase of the kinetic inductance $L_{\mathrm{kin}} = \mu_0\lambda_L^2 l/wt$ (with $\mu_0 = 4\pi \times 10^{-7}\,\mathrm{Vs/Am}$, w the width, t the film thickness and l the length of the loop) [28].

To overcome these potential limitations, a second approach in order to optimize $S_\Phi^{1/2}$ was investigated within this thesis. Detailed numerical studies of dc SQUIDs revealed that well-chosen asymmetries in L, C, I_0 and in particular R may improve $S_\Phi^{1/2}$ [29, 30, 31]. The technologically most simple solution for a ultra-high asymmetry of R is to use strongly underdamped tunnel junctions and to shunt only one of the two Josephson junctions. The asymmetry in R for such a SQUID is then limited only by the residual resistance of the quasiparticles of the unshunted tunnel junction (which is determined by the quality of the tunnel barrier), yielding a ratio $R_1/R_2 = 1/10000$ and above. Even though, there seems to be a trend in the numerical simulations that the sensitivity of SQUIDs improves with increasing asymmetry of R, for numerical reasons, the limit of ultra-high R asymmetry can not be analyzed. Therefore, the question whether or not the idea of leaving one junction unshunted improves the noise figures of dc SQUIDs has to be answered by experiments. If this is the case, this simple "trick" could be applied whenever the noise performance of a symmetric SQUID has to be improved. For the nanoSQUIDs, for instance, an improvement of S_Φ might be possible beyond the limits of miniaturization.

Up to now, the approaches for the improvement of the noise performance of a SQUID have been considered. As already mentioned, in order to improve the spin sensitivity, one has in addition to consider the magnetic coupling between a dipole field and the SQUID loop. Considering the two situations plotted in Fig. 0.2, the

coupling ϕ_μ between a SMP and the SQUID can be maximized by minimizing either the area of the SQUID loop (for the blue SMP at the center of the loop) or the area cross-section $S = wt$ of the superconducting line (for the green SMP on top of the loop). Since the inductance of the SQUID depends strongly on the geometrical properties of the SQUID loop, the optimization of ϕ_μ and $S_\Phi^{1/2}$ can not be solved independently. While the reduction of S would enhance ϕ_μ, for linewidths below the London penetration depth λ_L a significant amount of kinetic inductance L_{kin} will be added to the total inductance of the SQUID and therefore worsen $S_\Phi^{1/2}$.

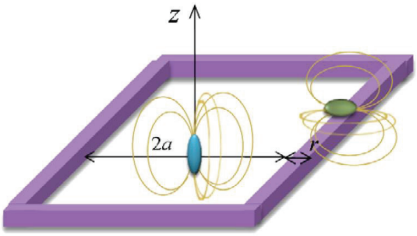

Figure 0.2: Comparison of the coupling of a SMP at the center (blue) and on top (green) of the SQUID loop [32]

This optimization procedure gets even more complicated if one considers the typical coercive fields of SMPs which are on the order of some 100 mT up to T [22]. To prevent Abrikosov vortices from entering the superconducting leads of the SQUID, again the miniaturization of the superconducting ring is inevitable [33, 34]. For the optimization of a nanoSQUID all these factors have to be considered and the optimum geometry strongly depends on the used materials, junction technologies and magnetic field ranges at which the sensor will be operated.

There have been many realizations of nanoSQUIDs using different types of nanopatterning methods, e.g., electron-beam lithography [20, 35], focused ion beam milling [36, 23], atomic force microscopy anodization [37, 38], self-aligned shadow evaporation[39], cross type junctions [40] or even carbon nanotube based junctions [41]. Most of these SQUIDs are based on constriction type Josephson junctions (cJJs) [42]. The main advantage of using cJJs for nanoSQUIDs is the high coupling at the position of the cJJ and rather easy fabrication techniques due to the single layer process. Even though some of these nanoSQUIDs had impressive flux noise properties ($0.2\,\mu\Phi_0/\mathrm{Hz}^{1/2}$ have been reported [23]), the low reproducibility of the cJJ properties and the limited temperature range of operation are major drawbacks of cJJ type SQUIDs. Furthermore, the strong interconnection between ϕ_μ and the width of the junction does not allow for an independent optimization of the junction properties and ϕ_μ, and the limitation to a single superconducting layer prohibits more complex SQUID designs gradiometric SQUIDs.

To overcome the disadvantages of cJJ type SQUIDs, in this this work we investigate the suitability of nanoSQUIDs based on conventional JJs, i.e. low-T_c superconductor/normal metal /superconductor (SNS) type Nb/HfTi/Nb and high-T_c

$YBa_2Cu_3O_7$ (YBCO) grain boundary junctions (GBJs). Both junction types yield very high critical current densities $j_c > 10^5\,\mathrm{A/cm^2}$ (at $T = 4.2\,\mathrm{K}$), providing sufficiently high critical currents even for junction sizes well below $1\,\mu\mathrm{m}$. While SNS type junctions are already intrinsically shunted, for the YBCO GBJs a thin Au layer on top of the GB provides non-hysteretic current voltage characteristics (IVC). Therefore, for both technologies no additional, space consuming external shunt is needed.

For the SNS type junctions a reliable fabrication process for junction widths down to 40 nm has been developed by the Physikalisch Technische Bundesanstalt (PTB) in Braunschweig [43, 44] and series arrays of up to $\sim$ 10000 junctions have been fabricated and are used as Josephson arbitrary waveform synthesizers which serve as alternating current voltage standards [45, 46] Since this fabrication process meets all the above mentioned requirements, a collaboration with the PTB was started in order to adapt this technology for the realization of spin sensitive nanoSQUIDs. The 3 dimensional structure of such Josephson junctions and two spatially separated Nb layers offers a high degree of freedom in the design layout of the SQUIDs. Due to the rather low upper critical field $B_{c2} < 1\,\mathrm{T}$ of Nb (as compared to the high-T_c SQUIDs) the field range of these SQUIDs will be limited to intermediate fields of some 100 mT.

The second approach for nanoSQUIDs is based on YBCO grain boundary junctions, The YBCO GBJ nanoSQUIDs are still based on a single superconducting layer, and therefore do not allow for complex SQUID designs, but the high upper critical field $B_{c2} > 30\,\mathrm{T}$ makes them promising candidates for high field applications in the Tesla range. Furthermore, it is possible to implement an additional constriction in the bulk YBCO SQUID loop which allows for the separation and independent optimization of coupling and the junction properties.

This thesis summarizes the work on both YBCO and SNS type nanoSQUIDs, as well as the results of measurements on asymmetric dc SQUIDs based on Nb/Al-AlO_x/Nb junctions. This work is organized in 3 chapters: **Chapter 1** summarizes the experimental techniques which have been used in order to perform the presented measurements. **Chapter 2** briefly summarizes the publications on measurements of the YBCO (**Publication 1**, **Publication 5**), the SNS type (**Publication 2**, **Publication 4**) and asymmetric (**Publication 3**) SQUIDs in low magnetic fields. Furthermore, measurements of the high field properties of the YBCO (**Publication 5**) type SQUIDs are summarized in this chapter. The publications are attached in the very end of this cumulative thesis.

Chapter 1

Experimental techniques

The experiments presented in this work (in particular the noise measurement of the SQUIDs) demanded for highly sophisticated measurement techniques, which are summarized in this chapter.

1.1 Measurements in low magnetic fields

The low magnetic field measurement setup enables a characterization of the samples under highly idealized conditions, i.e. shielding of external electro-magnetic waves and magnetic fields. Based on the measurements performed in this setup, we are able to determine the sensitivity of the SQUIDs without any external influences, an important requirement for the optimization of the devices.

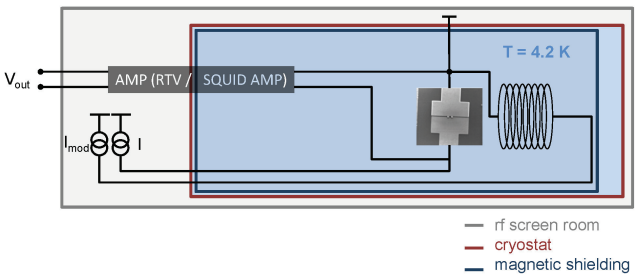

Figure 1.1: Schematic of the low-magnetic-field setup for noise measurements. The voltage was amplified either at room temperature with a high input impedance amplifier or with a SQUID amplifier at $T = 4.2\,\mathrm{K}$.

Fig. 1.1 shows a schematic of the low-field measurement setup. A radio frequency (rf) screening room shields the sample from external electro-magnetic radiation. The sample is mounted on a dipstick and cooled to $T = 4.2\,\mathrm{K}$ inside a liquid He dewar. A

cup made of Cryoperm® 10 surrounds the sample and serves as magnetic shielding; the residual magnetic field is on the order of $B_{\mathrm{res}} \approx 100\,\mathrm{nT}$. An external magnetic field up to $B_a \approx 1\,\mathrm{mT}$ can be applied by a coil perpendicular to the plane of the SQUID. All currents are applied by battery powered, low-noise current sources. For measurements of the dc properties of the devices, a high input impedance amplifier at room temperature (RTA) with a rms equivalent input voltage noise of $S_{V,\mathrm{RTA}}^{1/2} = 6\,\mathrm{nV/Hz^{1/2}}$ is used. Even though the RTA is a reliable, easy to use tool for voltage measurements, it is not capable to detect the very small rms voltage noise on the order $S_{V,\mathrm{SQUID}}^{1/2} \approx 100\,\mathrm{pV/Hz^{1/2}}$ and below of the SQUIDs that are investigated in this work. In order to overcome the limitations of a RTA, a cryogenic voltage amplifier, i.e a SQUID amplifier is used for the noise measurements. In the following the properties, advantages and disadvantages of such an amplifier are discussed, detailed calculations can be found in **Appendix A** of this thesis .

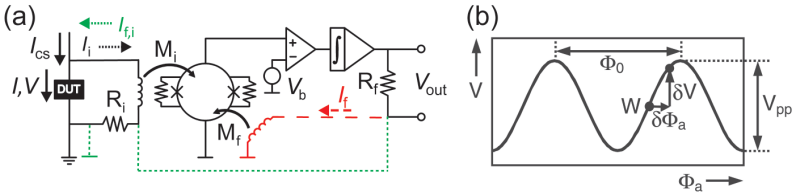

Figure 1.2: (a) Schematic of the most common used SQUID amplification schemes (red dashed line: FLL, green dotted line: VLL). (b) V vs. Φ_a characteristics of a SQUID at constant I, with working point W [27].

In order to amplify the voltage V of a device under test (DUT) with a SQUID one first has to transform the voltage into a magnetic flux. This is done via an input coil in parallel to the DUT. An input resistor R_i in series to the input coil transforms V into a current through the input coil (see Fig. 1.2(a)). The input coil is coupled to a SQUID via the mutual inductance M_i and therefore applies a magnetic flux Φ_a to the SQUID that is proportional to V. For a SQUID operated at the optimal working point W (see Fig. 1.2(b)), a small change $\delta\Phi_a$ leads to a linear change δV of the SQUID voltage. For input voltages that do not exceed the linear range of the V vs. Φ_a curve, this so called open loop (OL) configuration already acts as a rather simple cryogenic amplifier. For typical values of a commercially available SQUID amplifier [25] like $M_i = 1\,\Phi_0/\mu\mathrm{A}$, a transfer function (i.e. the slope of the V vs. Φ_a curve), $V_\Phi = 100\,\mu\mathrm{V}/\Phi_0$ and $R_i = 1\,\Omega$ this would lead to a voltage gain

$$G = V_{\mathrm{out}}/V = V_\Phi M_i/R_i \tag{1.1}$$

of 100. The equivalent rms input voltage noise of such an amplifier (assuming a rms flux noise of the SQUID $S_\Phi^{1/2} = 1\,\mu\Phi_0/\mathrm{Hz^{1/2}}$ and $T = 4.2\,\mathrm{K}$) is

$$S_{V,\mathrm{amp}}^{1/2} = (4k_BTR_i + S_\Phi V_\Phi^2/G^2)^{1/2} \approx 15\,\mathrm{pV/Hz^{1/2}}, \tag{1.2}$$

almost solely limited by R_i. A major drawback of such OL amplification is the low input resistance (for low frequencies determined by R_i), which leads to a lower bias current I of the DUT than the applied current I_{cs}, due to the current divider I/I_i.

For many applications (like in this work) an extended linear range of the amplifier as well as a higher voltage gain is needed. The most common solution for this task is the use of an electronic feedback technique. Fig. 1.2(a) shows a schematic of the two most commonly used configurations, i.e flux locked loop (FLL) (red dashed line) and voltage locked loop (VLL) (green dotted line). In the FLL configuration, the voltage of the SQUID is fed to an operational amplifier, integrated, and a current through the feedback coil which is coupled via the mutual inductance M_f to the SQUID is fed back in order to compensate the flux produced by the voltage of the DUT. This feedback keeps the SQUID always at the working point W and therefore linearizes the output signal even for input signals much higher than the linear range of the V vs. Φ_a characteristics.

The gain of the FLL is

$$G = R_f M_i/(R_i M_f), \tag{1.3}$$

which is $G = 10^5$ for typical values $R_f = 10\,\mathrm{k\Omega}$, $R_i = 1\,\Omega$, $M_i = 1\,\Phi_0/\mu\mathrm{A}$ and $M_f = 10\,\Phi_0/\mu\mathrm{A}$. The equivalent rms input voltage noise for a FLL is

$$S_{V,\mathrm{amp}}^{1/2} = (4k_B T R_i + R_i^2/M_i^2 S_\Phi)^{1/2}, \tag{1.4}$$

limited to $S_{V,\mathrm{amp}}^{1/2} \approx 15\,\mathrm{pV}$ for $R_{\mathrm{DUT}} = 0$. The input impedance of the FLL is (same as for OL) determined by R_i and therefore rather low. In **Publication 3** we present a technique in order to compensate the low input impedance of the FLL.

In the VLL configuration, the feedback current is applied to the input resistor R_i in order to compensate the voltage of the DUT. As a consequence, the current through the input coil equals 0 and Φ_a is constant for all frequencies the SQUID electronic is able to control. This leads to a high input impedance of the VLL. The voltage gain can be calculated to

$$G = -R_f/R_i, \tag{1.5}$$

which is $G = 10^4$ for a typical feedback resistance $R_f = 10\,\mathrm{k\Omega}$ and input resistance $R_i = 1\,\Omega$. The equivalent rms input noise of a VLL is

$$S_{V,\mathrm{amp}}^{1/2} = (4k_B T R_i + (R_i + R_{\mathrm{DUT}})^2/M_i^2 S_\Phi^2)^{1/2}. \tag{1.6}$$

Even though the high input impedance of the VLL is a major advantage over the FLL, Eq. 1.6 reveals a severe problem for noise measurements with a VLL. In contrast to the noise of the FLL, for the VLL the noise produced by the SQUID depends on R_{DUT} (second term of Eq. 1.6). For this reason, the measurement of devices with a nonlinear resistance and a very low voltage noise on the order of $S_{V,\mathrm{AMP}}$, gets complicated since a simple subtraction of a constant amplifier noise is not possible. Since this is exactly the case for the noise measurements presented in this work, all noise measurements were performed in the FLL. A second drawback of the VLL

compared to the FLL is the galvanic coupling of the feedback electronics and the DUT. In some cases this causes unavoidable ground loops, which add a significant amount of voltage noise (in particular at $f = 50\,\mathrm{Hz}$) to the DUT's voltage.

The striking sensitivity of this measurement setup not only allows for noise measurements but also for other types of measurements which demand for low noise amplifiers. For instance, in Ref. [47] we use the SQUID amplifier as a very sensitive detector for the critical current of a SQUID with a voltage criterion of 50 nV.

1.2 Measurements in high magnetic fields

Even though, the results of measurements performed with the low-field setup are essential for the optimization of the SQUIDs with respect to their sensitivity, no information on the performance of the SQUIDs in high magnetic fields can be obtained. For this purpose a second measurement setup was built (see Fig. 1.3).

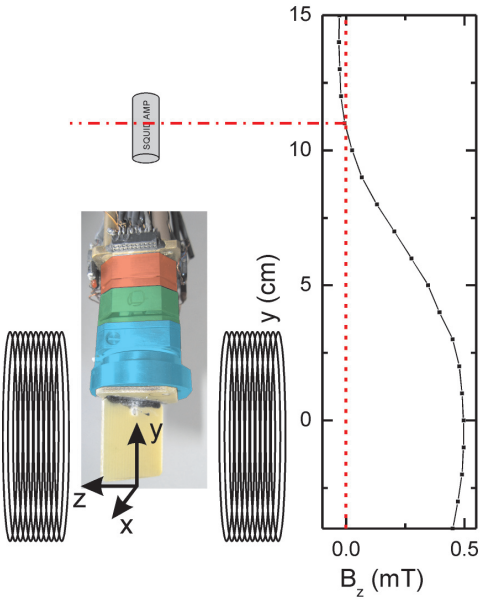

Figure 1.3: Schematic (not to scale) of the high field setup. The split coil produces magnetic fields in z-direction up to 7 T. The sample can be aligned via two goniometers along the x- (red) and z-axis (green) and a rotator around the y-axis (blue) with respect to the applied field. The graph shows B_z of the split coil as a function of y; the SQUID amplifier inside a Nb shielding (gray) is mounted at the $B_z = 0$ point.

Magnetic fields up to 7 T can be applied with a superconducting split coil. First results of YBCO SQUIDs operated at $B_z = 2\,\mathrm{T}$ measured within this setup are presented in Ref. [48]. For noise measurements, a SQUID amplifier was installed. Since the Nb shielding of this SQUID amplifier only works up to some 100 mT, the position of the SQUID amplifier was carefully adjusted to the zero crossing point of the magnetic field of the split coil (see Fig. 1.3). Even for magnetic fields up to $B_z \approx 1.5\,\mathrm{T}$ (at the center of the split coil), measurements with the SQUID amplifier were possible.

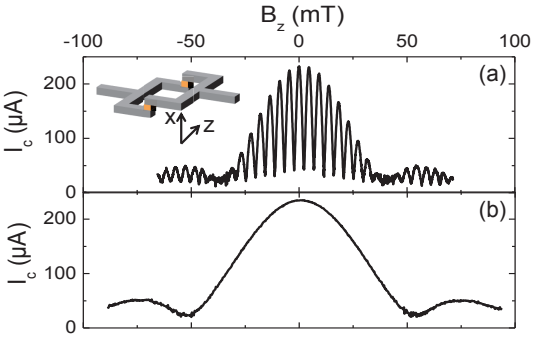

Figure 1.4: (a) critical current I_c vs. magnetic field B_z in case of the not aligned SQUID. (b) I_c vs. B_z after the alignment procedure.

The sample is mounted on top of two goniometers and a rotator, enabling a precise alignment with respect to the applied magnetic field. An example of such an alignment is shown in Fig. 1.4. For the not-aligned SQUID (Fig. 1.4(a)), the Fraunhofer modulation of the critical current I_c of the Josephson junctions is superimposed by oscillations caused by flux penetrating the SQUID loop due to a residual x-component of the magnetic field. Subsequent alignment of the SQUID increases the period of the SQUID oscillations until, for sufficiently good alignment, only the Fraunhofer pattern of the Josephson junctions remains (Fig. 1.4(b)).

Contributions

- **Publication 1:**

  The publication was done in collaboration with the groups of S. Menzel, R. Klingeler and B. Büchner at the Leibniz-Institut für Festkörper- und Werkstoffforschung (IFW) in Dresden. The YBCO films were grown by M. Turad (PhD-Student) and R. Werner (PhD-Student). K. Konovalenko (Postdoc) prepatterned the film by photolithography and Ar ion milling. The final FIB milling was done at the IFW Dresden by E. Kleisz (Technician). M. Kemmler (Postdoc) assisted with the development of the measurement setup and the sample design. My contribution was the building of the measurement setup, sample design, the transport and noise measurements and their interpretation, and the theoretical calculations of the coupling factor.

- **Publication 2:**

  The publication was done in collaboration with the group of J. Kohlmann and A.B. Zorin at the Physikalisch Technische Bundesanstalt (PTB) in Braunschweig. O.F. Kieler (Scientist) and T. Weimann (Scientist) fabricated the nanoSQUIDs. R. Wölbing (Diploma thesis) assisted by the transport measurements. M. Kemmler assisted with the transport and noise measurements and the interpretation of the results and the sample design. I was in charge of the sample design, transport and noise measurements, the analysis and interpretation of the results, and the theoretical calculation of the coupling factor.

- **Publication 3:**

  This work was done in collaboration with the group of K. Ilin and M. Siegel at the Karlsruhe institute of technology (KIT) in Karlsruhe. J.M. Meckbach (PhD-student) fabricated the symmetric and asymmetric SQUIDs. M. Rudolph (Diploma thesis) performed the transport and noise measurements under my supervision. M. Kemmler assisted with the interpretation an planing of the experiments. My contribution was the planing of the experiment, the sample design, assistance for the noise measurements, data analysis and interpretation.

- **Publication 4:**

  The transport and noise measurements presented in this work were done by T. Schwarz (PhD-student). R. Wölbing performed the numerical simulations

of the coupling factor and for the optimized geometry presented in the last part of the publication. M. Kemmler assisted with the planing of the experiments, the sample design and the interpretation of the results. My contribution was the building of the measurement setup, the sample design, the interpretation of the results and assistance during the transport and noise measurements.

Publication 5:

This work was done in collaboration with the Department of Physics at the university of Basel, the PTB in Braunschweig, the Laboratoire des Matériaux Semiconducteurs of the Ecole Polytechnique Fédérale in Lausanne (EPFL), the Physik-Department E11 at the Technische Universität in München (TUM) and the Faculté Sciences et Technique de l'Ingénieur in Lausanne (STI). The contributions dispersed as follows:

- A. Buchter, F. Xue, M. Poggio:
  Planning of the experiment and all MFM related measurements.
- O.F. Kieler, T. Weimann, J. Kohlmann, A.B. Zorin (PTB):
  Fabrication of the nanoSQUID.
- D. Rüffer, E. Russo-Averchi, A. Fontcuberta i Morral (EPFL):
  Fabrication of the Ni nanotube.
- R. Huber, P. Berberich, D. Grundler:
  Fabrication of the Ni nanotube.

M. Kemmler made numerical simulations of the coupling between the Ni nanotube and the SQUID. My contribution was the planning and the organization of the experiment. All SQUID related measurements have been performed by M. Kemmler and me . The analysis and the interpretation of the results were done by me.

Chapter 2

Summary of publications

2.1 Publication 1: Resistively shunted $YBa_2Cu_3O_7$ grain boundary junctions and low-noise SQUIDs patterned by a focused ion beam down to 80 nm linewidth

The aim of this work was both to explore the limitation of the miniaturization of YBCO GBJs and the realization and the characterization of first nanoSQUIDs consisting of such junctions.

At a first glance, dc SQUIDs based on high-T_c superconductors might seem to be inappropriate for the ambitious goal of ultra-sensitive measurements on small spin systems, because measurements performed by various groups on different high-T_c dc SQUIDs consistently showed a much higher white noise level in the experiment as compared to theoretical simulations [49]. Most probable reasons for this observation might be an underestimate of the inductance due to a high contribution of the kinetic inductance L_{kin}, the presence of resonances caused by parasitic capacitances and inductances, random telegraph noise either due to critical current fluctuations, caused by defects in the tunnelling barrier or the motion of Abrikosov vortices, at frequencies much higher than the bandwidth of the measurement systems or a non-sinusoidal current-phase relation of the grain boundary junctions.

These sources for a degraded sensitivity might be partly or completely be eliminated by a miniaturization of the SQUIDs. A smaller SQUID loop reduces the geometric inductance of the SQUID and therefore counteracts L_{kin} as long as the London penetration depth is not undercut. The smaller inductance in addition to smaller stray capacitances of nano-sized junction increase the frequency of parasitic resonances, i.e. a shift towards higher voltages in the current voltage characteristics. If the voltage across the SQUID at the optimum bias point is below the voltage of the resonances, no enhancement of the noise level is expected. Furthermore, the number of defects in a tunnelling barrier is proportional to its area. Hence, a smaller width of the GBJ reduces the probability of fluctuations with a high characteristic frequency

caused by a defect. Simultaneously, the number of vortices in the superconducting areas is reduced by the miniaturization. A deviation of the sinusoidal current-phase relation of an ideal Josephson junction can be explained by the $d_{x^2-y^2}$-wave symmetry of the order parameter in YBCO and faceting of the grain boundary [50, 51]. For junctions where the width is on the order of $10 - 100\,\mathrm{nm}$, i.e. below the typical length of a facet [52, 53, 54], the current-phase relation is expected to be sinusoidal again. Therefore it is not clear whether YBCO **nano**SQUIDs still exhibit enhanced noise figures. Even if it turns out that the sensitivity of the high-T_c nanoSQUIDs in **low** magnetic fields is not as good as compared to low-T_c nanoSQUIDs, the huge upper critical field $> 30\,\mathrm{T}$ of YBCO enables experiments in magnetic fields, where the superconductivity in low-T_c superconductors breaks down.

Previous attempts for the reduction of the width of YBCO GBJs to the sub-μm range revealed a strong degradation of the critical current density j_c for junction widths w below 500 nm [55, 56]. In these works a combination of electron beam lithography and ion beam etching was used for the patterning of the GBJs. The most probable explanation for the degradation of j_c is the creation of defects in the crystallographic order of the YBCO and loss of oxygen at the border of the GBJs due to the ion milling. In particular in the vicinity of the grain boundary, where the crystallographic order is already disturbed, these effects are very severe.

In the first part of the publication we demonstrate a new patterning technique where the crucial final nano-patterning step of the junctions is performed by optimized "soft" focused ion beam (FIB) milling. In brief, the fabrication process is as follows. Starting with a $SrTiO_3$ symmetric [001] tilt bicrystal substrate we deposited a 50 nm thick c-axis orientated epitaxially grown YBCO film using pulsed laser deposition, followed by in-situ evaporation of a Au thin film. The Au film served as a protection layer during the final FIB milling and later on as a resistive shunt for the GBJs in order to provide a nonhysteretic current-voltage characteristics (IVC). Using photolithography and Ar ion etching, we then patterned $8\,\mu$m wide bridges straddling the grain boundary. In a final patterning step we used FIB milling in order to further reduce the width w of the GBJs. For the FIB milling we carefully minimized the ion exposure time and avoided direct ion irradiation of the part of the grain boundary not to be cut.

With this fabrication process, a series of GBJs in the range $80\,\mathrm{nm} \leq \mathrm{w} \leq 7.8\,\mu$m was patterned. All of these junctions showed resistively-and-capacitively-shunted junction(RCSJ)-like IVCs and yielded high critical current densities j_c well above $10^5\,\mathrm{Acm}^{-2}$ (at $T = 4.2\,\mathrm{K}$) even for the smallest junctions with $w = 80\,\mathrm{nm}$.

In the second part of the publication we present measurements of first nanoSQUIDs fabricated with the new patterning scheme. The SQUIDs were characterized with respect to their transport and noise properties at $T = 4.2\,\mathrm{K}$ in a magnetically and electrically shielded environment. While for the transport measurements a simple four point measurement arrangement with voltage amplifiers at room temperature could be used, the small rms voltage noise of the nanoSQUIDs demanded for a more sophisticated readout scheme. Therefore we used a dc SQUID amplifier in order to

amplify the voltage noise of the nanoSQUIDs (see chapter 1.1 for details). Under these conditions, the nanoSQUIDs showed a low rms flux noise of $4\,\mu\Phi_0/\mathrm{Hz}^{1/2}$.

In the last part of the publication , we derive a general expression of the magnetic coupling $\phi_\mu(\hat{e}_\mu, \vec{r})$ between a point-like magnetic moment $\vec{\mu}$ pointing in $\hat{e}_\mu$-direction at position $\vec{r}$ and a SQUID by simple energy arguments. In contrast to previous theoretical models [26, 57], where the SQUID is approximated by a filamentary circular current distribution, the derived expression allows for the calculation of the coupling factor for any given current distribution of the circulating current I in a SQUID. This enables us to determine ϕ_μ, taking the real SQUID geometry and the superconductivity into account by calculating the 2-dimensional current distribution of I with a simulation software based on Maxwell and London equations [58]. The measured $S_\Phi^{1/2}$ together with the calculated ϕ_μ yield a minimum spin sensitivity $S_\mu^{1/2} = 390\,\mu_B/\mathrm{Hz}^{1/2}$ which to our knowledge is the best value achieved so far using high-T_c SQUIDs.

2.2 Publication 2: Superconducting quantum interference devices with submicron Nb/HfTi/ Nb junctions for investigation of small magnetic particles

Most of the available low-T_c dc SQUIDs are based on Nb with Nb/Al-AlO_x/Nb superconductor/ insulator/ superconductor (SIS) type trilayer Josephson junctions, shunted with an external metal resistor. This technology allows for a reliable design of the SQUID parameters, i.e. the critical current I_0, the resistance R, the capacitance C and the inductance L. The two separated Nb layers offer a high degree of freedom in the layout and complex devices like gradiometric SQUIDs or series arrays of SQUIDs can easily be realized. In contrast to SQUIDs based on high-T_c superconductors, the transport and noise performance of Nb SQUIDs are well described by numerical simulations based on the Langevin equations. Unfortunately, for the realization of nanoSQUIDs, this junction technology has some severe drawbacks. First, the current density of standard SIS type junctions is smaller than $\approx 20\,\mathrm{kA}$ [59], which is quite low for sub-micron junctions. For higher current densities, the probability of superconducting shorts in the insulating layer increases. Second, the external shunt resistor that is needed to provide nonhysteretic IVCs is very space consuming and would strongly limit the miniaturization. For these reasons, the almost solely used approach in order to fabricate nanoSQUIDs are SQUIDs based on constriction type junctions. A big advantage of this type of junctions is the high coupling factor ϕ_μ between a magnetic dipole and the SQUID loop at the position of the junction. Furthermore, the fabrication process is quite simple, due to the single superconducting layer. However, in practice it turns out, that a reproducible adjustment of the parameters I_0, R, C of such junctions is very difficult. For this reason, often the temperature is used in order to optimize I_0, which strongly limits the temperature range at which such nanoSQUIDs are most sensitive.

In this manuscript we demonstrate a different approach based on more conventional Nb/HfTi/Nb SNS type trilayer junctions that still yield all the advantages of the above mentioned SIS process but circumvents the drawbacks of the Nb/Al-AlO_x/Nb technology.

The fabrication of the nanoSQUIDs was done by the PTB in Braunschweig by means of a reliable and reproducible trilayer fabrication process based on electron beam lithography and Ar ion etching [43, 44], allowing for SNS type JJs with widths well below $1\,\mu\mathrm{m}$. The normal metal interlayer provides very high critical current densities $j_c = 200 - 300\,\mathrm{kA/cm^2}$ at temperature $T = 4.2\,\mathrm{K}$ Furthermore, these junctions do not need an external shunt resistor, since the normal metal interlayer intrinsically shunts the junctions, providing nonhysteretic current-voltage characteristics.

Measurements of three nanoSQUIDs with different layouts, one with a gradiometric design (see Fig. 2.1(b)) and two magnetometer-type (see Fig. 2.1(a)) with

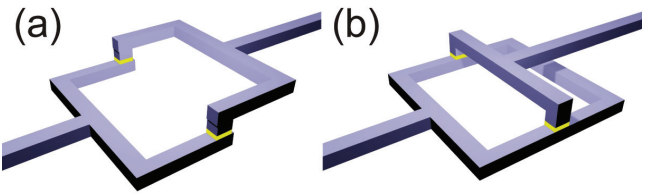

Figure 2.1: Schematic view of the magnetometer (a) and gradiometric SQUID (b) presented in **Publication 2**. Yellow areas indicate the HfTi interlayer, blue indicates the Nb top and bottom electrodes.

and without washer[1], are presented. The loop diameter of the SQUIDs was on the order of 1 μm, the JJs had an area of $200 \times 200\,\mathrm{nm}$. The IVC of all SQUIDs was non-hysteretic with critical currents $I_0 \approx 180\,\mu\mathrm{A}$, resistances $R \approx 230\,\mathrm{m\Omega}$, yielding a characteristic voltages $V_c \approx 40\,\mu\mathrm{V}$. From numerical simulations based on the RCSJ model we determined the screening parameter $\beta_L = 2I_0L/\Phi_0 \approx 0.2$, yielding a very small SQUID inductance of $L \approx 2\,\mathrm{pH}$. For all SQUIDs we found a very low rms flux noise $250\,\mathrm{n}\Phi_0/\mathrm{Hz}^{1/2} < \mathrm{S}_\Phi^{1/2} < 300\,\mathrm{n}\Phi_0/\mathrm{Hz}^{1/2}$ in the white noise limit. From the measured $S_\Phi^{1/2}$ and numerical calculations of the magnetic coupling between a point-like magnetic moment and the SQUID we estimate a rms spin sensitivity $S_\mu^{1/2} = 44\,\mu_B/\mathrm{Hz}^{1/2}$ for the gradiometric, and $S_\mu^{1/2} = 29\,\mu_B/\mathrm{Hz}^{1/2}$ for the magnetometer type nanoSQUID. With the results of these first SQUIDs, the already impressive spin sensitivity can be further improved, e.g. by miniaturization of both, the size of the junctions and the SQUID loop. In addition, a constriction in the superconducting leads of the SQUID loop could further increase ϕ_μ. Even though a factor of 30 lower spin sensitivity is still a quite challenging task, we demonstrated the huge potential of this new approach of using a more conventional type of junctions than constriction type junctions in order to reach the goal of single spin resolution.

[1] A washer is a purposely extended linewidth of the SQUID loop in order to increase the field sensitivity of a SQUID

2.3 Publication 3: Direct current superconducting quantum interferometers with asymmetric shunt resistors

For more than 40 years, dc SQUIDs consisting of a superconducting ring separated by two Josephson junctions have been investigated and optimized with respect to their noise performance. Even though there are indicators, that asymmetries in the junctions properties might enhance the noise performance at least for a not optimized symmetric SQUID [60, 61], it is commonly believed that ultra-low sensitivity can only be achieved by an optimized SQUID with symmetric junctions. However, up to now this opinion is more or less based on gut instinct, since neither a detailed numeric analysis including all possible asymmetries of a SQUID nor an experimental comparison of optimized devices with and without asymmetries has been performed.

In the first part of the manuscript we show extensive numerical simulations based on the Langevin equations which reliably describe the SQUID dynamics. The simulations considered asymmetries in the critical current, the capacitance and in the resistance of the two junctions. Furthermore, we accounted for an asymmetry in the inductance of the two SQUID arms. For a given asymmetry, the energy resolution $\epsilon = S_\Phi/2L$, where S_Φ is the flux noise and L is the inductance of the SQUID has been optimized with respect to the bias current I and external flux Φ_a. This was done for a series of all possible asymmetries (and combinations of different asymmetries) ranging from a symmetric to a highly asymmetric device. Surprisingly, the results of this analysis were contradictory to the statement that asymmetries worsen the sensitivity of SQUIDs. In particular for a high asymmetry in the resistance of the two junctions we found a reduction of ϵ by a factor of 4 for the asymmetric SQUID as compared to the symmetric one.

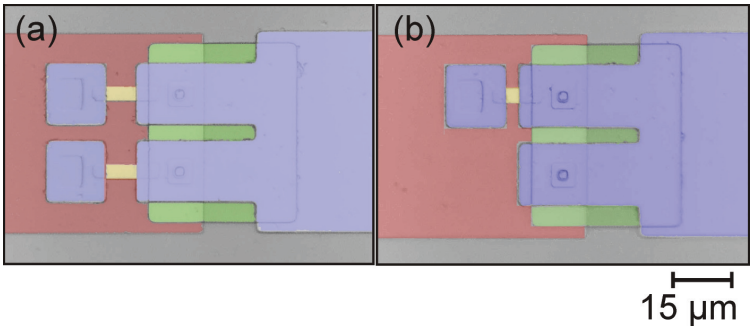

Figure 2.2: Optical image of (a) a symmetric SQUID and (b) an asymmetric SQUID, where only one of the two junctions is shunted by a Pd layer (yellow). The top (blue) and bottom (red) electrode are separated by two circular junctions and a SiO_x (green) layer.

The most easy way to realize such a high resistance asymmetry is to shunt only one of the two tunnel junctions, while leaving the other junction unshunted (see Fig. 2.2). The resistance of the unshunted junction is then determined by the residual resistance of the tunneling barrier which depends on the quality of the insulating layer. With this simple, yet novel idea a high ration $R_1/R_2 = 1/10000$ can easily be realized.

In the second part of the manuscript transport and noise measurements of an asymmetric and the corresponding (i.e. similar critical current I_0, resistance R and inductance L) symmetric SQUID at $T = 4.2\,\mathrm{K}$ in a magnetically and electrically shielded environment are presented. The SQUIDs are based on standard Nb/Al-AlO_x/Nb trilayer Josephson junctions with a Pd layer serving as external shunt resistor and have been fabricated at the Karlsruhe institute of technology (KIT) by a combination of standard photolithography, reactive ion etching and Ar ion etching. We show that both, dc properties as well as noise figures of the asymmetric SQUID are in very good agreement with the numerical simulations. For the presented SQUIDs we achieved $\epsilon = 32\,\hbar$ for the asymmetric SQUID and $\epsilon = 110\,\hbar$ for the corresponding symmetric SQUID ($\hbar$ is Planck's constant divided by 2π), i.e. a factor of 3.4 improvement of ϵ due to the resistance asymmetry. While the absolute value of the energy resolution ϵ of an asymmetric SQUID can still be optimized by a smaller SQUID inductance, in normalized units this is the best value ever measured for a dc SQUID.

2.4 Publication 4: Nanoscale multifunctional sensor formed by a Ni nanotube and a scanning Nb nanoSQUID

Publication 4 summarizes the results of the experimental determination of the coupling factor ϕ_μ of a SNS type dc nanoSQUID. While the measurement of the SQUID sensitivity, i.e. the rms flux noise $S_\Phi^{1/2}$ was performed for some nanoSQUIDs, up to now the coupling factor ϕ_μ was determined by numerical or analytical calculations only. In order to validate these calculations we combined a low-temperature magnetic force microscope (LTMFM) with one of our Nb/HfTi/Nb nanoSQUIDs. The nanoSQUID had a sandwich-type geometry, i.e. the top Nb line was directly on top of the bottom Nb line, separated by the two HfTi interlayers (c.f. Fig. 2.3). Additional leads in the bottom Nb line allowed for the on chip modulation of the SQUID via a current I_{mod} (see Fig. 2.3). Preliminary measurements determined the rms flux noise of the SQUID (without external magnetic fields) to $S_\Phi^{1/2} = 220\,\mathrm{n}\Phi_0/\mathrm{Hz}^{1/2}$.

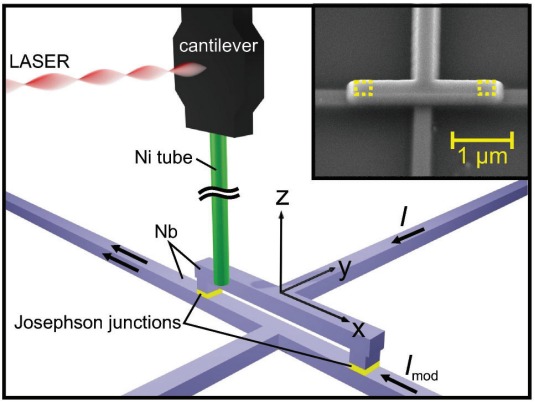

Figure 2.3: Schematic of the experimental setup for the determination of the spatial dependence of the magnetic coupling between a nano-tube (green) attached to a Si cantilever (dark grey) and a nanoSQUID (blue). The cantilever motion is detected via a LASER beam (red) and an optical interferometer (not shown).

Figure 2.3 shows a schematic of the experiment. A Ni nano-tube (green) was fixed to a Si cantilever (dark grey) of a LTMFM. The motion of the cantilever was detected by a LASER interferometer [62]. The nanoSQUID (blue) was mounted in vacuum on top of a 3D piezo-electric positioning stage at the bottom of a continuous-flow ^{3}He cryostat. Magnetic fields were applied via a superconducting coil in $z-$direction.

In previous measurements of the SQUID in high magnetic fields, we observed a large jump in the voltage across the SQUID at homogeneous magnetic fields $\mu_0 H_z \approx 50\,\mathrm{mT}$. In the first part of the manuscript we present MFM images of the SQUID

for $H_z = 0$ and $\mu_0 H_z \geq 50\,\mathrm{mT}$, i.e. before and after the jump in the voltage. These images related the jump to the entrance of a single Abrikosov vortex in the superconducting leads, very close to the SQUID loop. This is a very important information for further improvement of the high field suitability of the nanoSQUIDs.

Before the measurement of the spatial dependence of the flux Φ coupled to the SQUID loop by the nano-tube at position $\vec{r}$, the magnetization of the nano-tube was saturated in $z-$direction by a homogeneous magnetic field $\mu_0 H_z = -150\,\mathrm{mT}$. In order to prevent Abrikosov vortices from entering the superconducting leads of the SQUID, this was done at $T = 14\,\mathrm{K}$. After cooling the SQUID to $T = 4.3\,\mathrm{K}$ at $H_z = 0$, we applied a bias current I and a current I_{mod} across the modulation line (c.f. Fig. 2.3) of the SQUID in order to operate the SQUID at its optimum working point. While moving the nano-tube with respect to the SQUID, I_{mod} was adjusted by a software controlled feedback procedure in order to keep the SQUID at a constant voltage, i.e. in a flux-locked loop. In this way, we determined $\Phi(\vec{r})$ for a large section of the 3 dimensional half-space above the SQUID.

We compare the measurements to simulations based on our calculation method of $\phi_\mu(\vec{r})$ (c.f. **Publication 1**) and taking the geometry of the nano-tube into account. The calculated $\Phi(\vec{r})$ were in good qualitative agreement with the experimental data, however, for absolute agreement we had to assume a by a factor of 2.1 lower magnetic moment $m = M_s V$ (M_s is the saturation magnetization, V the Ni Volume) of the tube than expected. Besides this deviation, which might be related to smaller effective Ni volume (due to magnetically dead layers or voids in the Ni layer) or a lower saturation magnetization of the Ni, the measurements confirmed our calculation method of $\phi_\mu(\vec{r})$.

2.5 Summary of Publication 5: Low-noise nanoSQUIDs operating in Tesla magnetic fields — towards detection of small spin systems with single-spin resolution

The striking argument for the use of high-T_c superconductors for nanoSQUIDs is the very high upper critical field that is needed in order to supress their superconducting properties. In this manuscript, for the first time we present flux noise measurements of a SQUID operated at a magnetic field of 1 T.

This work is the continuation of **Publication 1**. The nanoSQUIDs have been fabricated by the same process as described in the summary of **Publication 1**.

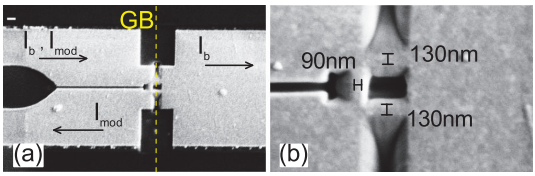

Figure 2.4: SEM images of the nanoSQUID. The grain boundary is indicated by the dashed yellow line. In (a) the direction of the modulation and bias currents I_{mod} and I_b are indicated by arrows. In (b) the dimensions of the most narrow sections of the nanoSQUID are indicated. [63]

The main difference between the nanoSQUIDs of this work and those of **Publication 1** is an additional constriction of $\approx 90\,\mathrm{nm}$ width in the superconducting part of the SQUID loop (c.f. Fig. 2.4). The purpose of this constriction is twofold. First, it enables us to apply a flux to the SQUID by sending a current I_{mod} through the constriction without the need of an external coil. Second, a magnetic particle placed on top of this constriction will strongly couple to the SQUID. Therefore, the coupling is separated from the Josephson junctions without a significant change of the device properties. This separation is only possible due to the conventional junction type and can not be done for constriction type junctions, since an additional constriction would serve as a third junction and therefore strongly influence the characteristics of the SQUID.

In the first part of the publication, we present transport and noise measurements of the SQUID. By comparison of the measured and the numerically simulated critical current vs. flux dependence we proof, that the additional constriction does not act as a Josephson junction. The rms spectral flux noise density $S_\Phi^{1/2}$ measured without external magnetic field showed a pronounced $1/f$ dependence up to a frequency of $f \sim 3\,\mathrm{kHz}$ (see Fig. 2.5). For higher frequencies we determined the white noise level $S_\Phi^{1/2}(0\,\mathrm{T}) = 1.3\,\mu/\Phi_0/\mathrm{Hz}^{1/2}$ (see Fig. 2.5(a)). This is a factor of 3 lower than for the SQUID presented in **Publication 1** and can be attributed to a higher characteristic

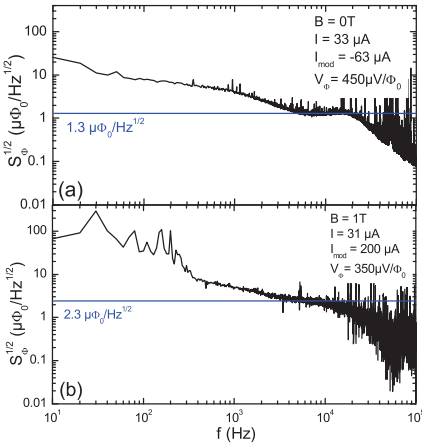

Figure 2.5: Noise spectra of the nanoSQUID at optimum working point. The blue line indicates the white noise level (a) at $B = 0\,\mathrm{T}$ ($S_\Phi^{1/2} = 1.3\,\mu\Phi_0/\mathrm{Hz}^{1/2}$) and (b) at $B = 1\,\mathrm{T}$ ($S_\Phi^{1/2} = 2.3\,\mu\Phi_0/\mathrm{Hz}^{1/2}$). [63]

voltage $V_c = 130\,\mu\mathrm{V}$ due to a thinner Au layer and a smaller SQUID inductance $L = 36\,\mathrm{pH}$ due to a smaller loop size. In order to determine the noise performance in higher magnetic fields, we applied a homogeneous magnetic field $\mu_0 H = 1\,\mathrm{T}$ parallel to the SQUID loop. Even at this background field, the critical current of the SQUID was only slightly reduced by a factor of 1.3. We measured a very low $S_\Phi^{1/2}(1\,\mathrm{T}) = 2.3\,\mu/\Phi_0/\mathrm{Hz}^{1/2}$ (see Fig. 2.5(b)), i.e. less than twice the value at zero field. With the calculated coupling factor $\phi_\mu = 9.2\,\mathrm{n}\Phi_0/\mu_\mathrm{B}$ for a magnetic particle placed on top of the constriction, we get a rms spin sensitivity $S_\mu^{1/2}(0\,\mathrm{T}) = 141\,\mu_\mathrm{B}/\mathrm{Hz}^{1/2}$ at zero field and a slightly worse but still excellent $S_\mu^{1/2}(1\,\mathrm{T}) = 250\,\mu_\mathrm{B}/\mathrm{Hz}^{1/2}$ at a magnetic field of 1 T. Even though nanoSQUIDs have been operated in magnetic fields up to 7 T [64] this is a remarkable result, since in contrast to the cited publication we demonstrate besides a high remaining critical current a high sensitivity of the nanoSQUID at high magnetic fields.

In the second part of the paper, we present a detailed study on how to optimize the geometry of the YBCO SQUIDs for best spin sensitivity. This analysis is based on experimental results of the presented SQUIDs, numerical simulations of the SQUID inductance and numerical simulations of the noise performance. The results of this analysis show, that for an optimized nanoSQUID based on YBCO single spin detection seems to be feasible.

Summary and outlook

The aim of this thesis was the investigation and optimization of nano-patterned SQUIDs for measurements of small magnetic particles in low and high magnetic fields. Therefore, two approaches, i.e., SQUIDs based on high-T_c YBCO grain boundary junctions and on SNS type Nb/HfTi/Nb junctions have been investigated. For both types of SQUIDs, transport and noise measurements at low and high magnetic fields and temperature $T = 4.2\,\mathrm{K}$ have been performed.

For the YBCO SQUIDs we first had to develop a reliable fabrication process for GBJs with widths on the order of 100 nm. This was achieved by a focused ion beam based patterning process, where a thin Au film protected the subjacent YBCO in the uncut regions. With this fabrication process junctions with widths down to 80 nm were realized without significant loss of the critical current density j_c. The remaining Au on top of the GB served as a resistive shunt for the junction in order to preserve an overdamped IVC at $T = 4.2\,\mathrm{K}$. The first SQUIDs fabricated with this patterning process had a low rms flux noise $S_\Phi^{1/2} = 4\,\mu\Phi_0/\mathrm{Hz}^{1/2}$ and we calculated a coupling factor $\phi_\mu \approx 10\,\mathrm{n}\Phi_0/\mu_\mathrm{B}$, yielding a good rms spin sensitivity $S_\mu^{1/2} = 390\,\mu_B/\mathrm{Hz}^{1/2}$.

Based on these first results, we optimized the design of the SQUIDs, i.e., higher characteristic voltage V_c due to higher resistance of the Au layer and implementation of an additional constriction in the bulk YBCO which served as "on chip" modulation coil and for the separation of the position with highest coupling and the GBJ. Under idealized conditions (electronically and magnetically shielded environment), the optimization of the SQUIDs reduced $S_\Phi^{1/2}$ by a factor of 3 to $1.3\,\mu\Phi_0/\mathrm{Hz}^{1/2}$ without reduction of ϕ_μ, resulting in an improved $S_\mu^{1/2} = 110\,\mu_B/\mathrm{Hz}^{1/2}$ (as compared to the previous SQUIDs). We demonstrated the operation of such SQUIDs at homogeneous magnetic fields up to 1 T with slightly increased $S_\Phi^{1/2} = 2.3\,\mu\Phi_0/\mathrm{Hz}^{1/2}$ due to stronger $1/f$ fluctuations, which are probably caused by the entrance of Abrikosov vortices into the superconducting leads.

For the first generation of low-T_c nanoSQUIDs based on Nb/HfTi/Nb SNS type Josephson junctions we realized both magnetometers and gradiometric SQUIDs with junction sizes below $200 \times 200\,\mathrm{nm}^2$. Both types of devices had a very low $250\,\mathrm{n}\Phi_0/\mathrm{Hz}^{1/2} \leq \mathrm{S}_\Phi^{1/2} \leq 300\,\mathrm{n}\Phi_0/\mathrm{Hz}^{1/2}$ in an electrically and magnetically shielded environment. We calculated a maximum $\phi_\mu = 8.5\,\mathrm{n}\Phi_0/\mu_\mathrm{B}$, which together with $S_\Phi^{1/2}$ results in a spin sensitivity $S_\mu^{1/2} \geq 29\,\mu_B/\mathrm{Hz}^{1/2}$ for the magnetometers and $S_\mu^{1/2} \geq 44\,\mu_B/\mathrm{Hz}^{1/2}$ for the gradiometric SQUIDs. A second generation of nanoSQUIDs, optimized for applications in higher magnetic fields and with an implemented coil

on chip has been fabricated. Under ideal conditions, we measured a slightly lower $S_\Phi^{1/2} = 220\mathrm{n}\Phi_0/\mathrm{Hz}^{1/2}$ as for the magnetometers of the first generation. We demonstrated a reliable operation up to magnetic fields of $B_{\max} = 60\,\mathrm{mT}$. For higher magnetic fields, we observed jumps in the voltage across the SQUIDs. We identified the origin of these jumps with the entrance of Abrikosov vortices in the superconducting leads near the SQUID loop by low-temperature magnetic force microscopy.

Besides the flux imaging, we used the combined system of the LTMFM and the nanoSQUID for first measurements of a nano-magnet (a Ni nano-tube) under "'real"' conditions. In this setup, we experimentally determined the flux $\Phi(\vec{r})$ coupled into the SQUID loop as a function of the particle position $\vec{r}$, demonstrating a flexible and non-destructive *in situ* tool for the challenging task of placing a small particle to the position of highest coupling. Comparison of the measured $\Phi(\vec{r})$ with our simulations are in good agreement, confirming the validity of our numerical calculations of the coupling factor ϕ_μ.

In parallel to the investigation of nanoSQUIDs a fundamental analysis based on the Langevin equations (including asymmetries in the SQUID parameters) in order to improve the sensitivity of dc SQUIDs was performed. These simulations showed that in particular a strong asymmetry of the shunt resistors of the two Josephson junctions improves the noise figures of a dc SQUID as compared to its symmetric counterpart. In order to demonstrate the validity of our analysis, we performed transport and noise measurements on a Nb/Al-AlO_x/Nb dc SQUID where only one of the two Josephson junctions was shunted — this is a novel approach for generating a maximum resistance asymmetry in a dc SQUID while still retaining nonhysteretic current voltage characteristics. For comparison we also investigated a symmetric SQUID with the same total resistance. For these devices we find a factor > 3 improved energy resolution for the asymmetric SQUID as compared with the symmetric device, in very good agreement with the numerical simulations.

Even though the SNS and the YBCO type nanoSQUIDs yielded excellent noise figures and could already be used as sensitive sensors in exciting experiments with nano-magnets, further improvements in order to enhance the spin sensitivity and the high-field suitability are possible. For the SNS type SQUIDs, for instance, the characteristic voltage $V_c \approx 50\,\mu\mathrm{V}$ was rather low, due to the small resistance of the HfTi interlayer. It has been shown [65, 66] that – dependent on the doping level x and the film thickness – $\mathrm{Nb}_x\mathrm{Si}_{1-x}$ offers a literally unlimited degree of freedom for the adjustment of V_c. Therefore, it should be possible to optimize V_c by exchanging of the HfTi by $\mathrm{Nb}_x\mathrm{Si}_{1-x}$ as interlayer, yielding strong improvements of the rms flux noise $S_\Phi^{1/2}$. Since the linewidth of the SNS type SQUIDs $w = 250\,\mathrm{nm}$ was well above the London penetration depth of Nb $\lambda_L = 90\,\mathrm{nm}$, further reduction of w would improve both the high field suitability as well as the coupling factor ϕ_μ. For the YBCO SQUIDs the film thickness was below λ_L which adds a significant amount of kinetic inductance to the SQUID total inductance. In **Publication 5** we present a detailed analysis of the SQUID parameters for an optimization of $S_\mu^{1/2}$ with the result that for the presented geometry a YBCO film thickness $t \approx 2\lambda_L$ would enhance $S_\mu^{1/2}$ close to single spin resolution. Whether YBCO nanoSQUIDs with such thick films would be suitable for high-field applications remains as an

open question and has to be investigated. Further improvement could be achieved by removing the shunting Au film on top of one grain boundary junction, which – due to the resistance asymmetry – could lower $S_\Phi^{1/2}$ and therefore $S_\mu^{1/2}$ by a factor ~ 3, as we showed in **Publication 3**.

Appendix A: SQUID amplifier

In this Appendix, the equations for the Gain and the rms input voltage noise of different SQUID amplifier connection schemes are derived. Refer to Fig. 1.2(a) for notations.

Flux Locked Loop (FLL)

The input voltage of the DUT is

$$V_{\text{in}} = IR_{\text{DUT}}. \tag{A.1}$$

The output voltage of the amplifier is

$$V_{\text{out}} = I_f R_f. \tag{A.2}$$

The current across the DUT I is

$$I = \frac{R_i}{R_{\text{DUT}} + R_i} I_{\text{cs}} \tag{A.3}$$

and the input current I_i is

$$I_i = \frac{R_{\text{DUT}}}{R_{\text{DUT}} + R_i} I_{\text{cs}} = \frac{R_{\text{DUT}}}{R_i} I. \tag{A.4}$$

Starting with the condition for the FLL

$$\Phi_i = \Phi_f, \tag{A.5}$$

and using the relation $\Phi = MI$, we calculate the Gain of the FLL:

$$\begin{aligned} M_i I_i &= M_f I_f \\ R_f M_i \frac{R_{\text{DUT}}}{R_i} I &= R_f I_f M_f \\ \frac{R_f}{R_i} V_{\text{in}} M_i &= V_{\text{out}} M_f \end{aligned}$$

$$\rightarrow G = \frac{V_{\text{out}}}{V_{\text{in}}} = \frac{R_f M_i}{R_i M_f}. \tag{A.6}$$

The equivalent input voltage noise of the amplifier consists of two components: the Johnson noise of the input resistor $S_{V,i} = 4k_BTR_i$ and the noise produced by the SQUID $S_{V,\mathrm{SQUID}}$. Starting with Eq.: A.5 and replacing flux by rms flux noise, voltage by rms voltage noise and dividing the result by the Gain, we calculate $S^{1/2}_{V,\mathrm{SQUID}}$:

$$\begin{aligned} \Phi_i &= I_f M_f \\ R_f \Phi_i &= V_{\mathrm{out}} M_f \end{aligned}$$

$$\rightarrow S^{1/2}_{V,\mathrm{SQUID}} = \frac{R_i}{M_i} S^{1/2}_{\Phi}. \tag{A.7}$$

Voltage Locked Loop (VLL)

See section 2.5 for definition of V_{out}, I and I_i; since in VLL the current I_i is compensated by the SQUID electronics $I = I_{\mathrm{cs}}$ and therefore $V_{\mathrm{in}} = I_{\mathrm{cs}} R_{\mathrm{DUT}}$. Starting with the condition for the VLL

$$I_i = -I_{f,i}, \tag{A.8}$$

we calculate the gain of the VLL:

$$\begin{aligned} R_f \frac{R_{\mathrm{DUT}}}{R_i + R_{\mathrm{DUT}}} I_{\mathrm{cs}} &= -R_f \frac{R_i}{R_i + R_{\mathrm{DUT}}} I_f \\ R_f V_{\mathrm{in}} &= -R_i V_{\mathrm{out}} \end{aligned}$$

$$\rightarrow G = -\frac{R_f}{R_i}. \tag{A.9}$$

Starting with Eq.: A.8 and replacing flux by rms flux noise, voltage by rms voltage noise and dividing the result by the Gain, we calculate $S^{1/2}_{V,\mathrm{SQUID}}$:

$$\begin{aligned} M_i I_i &= -M_i I_{f,i} \\ \Phi_i &= -M_i \frac{R_i}{R_{\mathrm{DUT}} + R_i} I_f \\ R_f \Phi_i &= -M_i \frac{R_i}{R_{\mathrm{DUT}} + R_i} V_{\mathrm{out}} \end{aligned}$$

$$\rightarrow S^{1/2}_{V,\mathrm{SQUID}} = \frac{R_{\mathrm{DUT}} + R_i}{M_i} S^{1/2}_{\Phi}. \tag{A.10}$$

Appendix B: List of acronyms

List of acronyms in the order of their appearance in the text:

dc	direct current
SQUID	Superconducting QUantum Interference Device
SNS	Superconductor/Normal metal/Superconductor
YBCO	$YBa_2Cu_3O_7$
GBJ	Grain Boundary Junction
LTMFM	Low Temperature Magnetic Force Microscope
TTMKM	Tieftemperatur Magnetisches Kraft Mikroskop
SMP	Small Magnetic Particle
MRFM	Magnetic Resonance Force Microscope
JJ	Josephson Junction
rms	rout mean square
RCSJ	Recistively and Capacetively Shunted Junction
cJJ	constriction type Josephson Junction
IVC	current-voltage characteristics
PTB	Physikalisch Technische Bundesanstalt
rf	radio frequency
RTA	Room Temperature Amplifier
DUT	Device Under Test
OL	Open Loop
FLL	Flux Locked Loop
VLL	Voltage Locked Loop
FIB	Focused Ion Beam
SIS	Superconductor/Insulator/Superconductor
LASER	Light Amplification by Stimulated Emission of Radiation
3D	3 Dimensional

Bibliography

[1] J. Frenkel and J. Dorfman. Spontaneous and induced magnetisation in ferromagnetic bodies. *Nature*, pages 274–275, 1930. 1

[2] E. C. Stoner and E. P. Wohlfarth. A mechanism of magnetic hysteresis in heterogeneous alloys. *Philosophical Transactions of the Royal Society of London. Series A, Mathematical and Physical Sciences*, 240(826):599–642, 1948. 1

[3] L Néel. *Ann. Geophys.*, 5:99, 1949. 1

[4] A. H. Morrish and S. P. Yu. Magnetic measurements on individual microscopic ferrite particles near the single-domain size. *Phys. Rev.*, 102:670–673, May 1956. 1

[5] L. Thomas, F. Lionti, R. Ballou, D. Gatteschi, R. Sessoli, and B. Barbara. Macroscopic quantum tunnelling of magnetization in a single crystal of nanomagnets. *Nature*, 383(6596):145–147, September 1996. 1

[6] D. Gatteschi and R. Sessoli. Quantum tunneling of magnetization and related phenomena in molecular materials. *Angewandte Chemie International Edition*, 42(3):268–297, 2003. 1

[7] L. Bogani, A. Vindigni, R. Sessoli, and D. Gatteschi. Single chain magnets: where to from here? *J. Mater. Chem.*, 18:4750–4758, 2008. 1

[8] N. Bardou, B. Bartenlian, C. Chappert, R. Megy, P. Veillet, J. P. Renard, F. Rousseaux, M. F. Ravet, J. P. Jamet, and P. Meyer. Magnetization reversal in patterned co(0001) ultrathin films with perpendicular magnetic anisotropy. *Journal of Applied Physics*, 79(8):5848–5850, 1996. 1

[9] S.J. Hefferman, J.N. Chapman, and S. McVitie. In-situ magnetising experiments on small regularly shaped permalloy particles. *Journal of Magnetism and Magnetic Materials*, 95(1):76 – 84, 1991. 1

[10] J. R. Maze, P. L. Stanwix, J. S. Hodges, S. Hong, J. M. Taylor, P. Cappellaro, L. Jiang, M. V. Gurudev Dutt, E. Togan, A. S. Zibrov, A. Yacoby, R. L. Walsworth, and M. D. Lukin. Nanoscale magnetic sensing with an individual electronic spin in diamond. *Nature*, 455:644–647, 2008. 1

[11] G. Balasubramanian, I. Y. Chan, R. Kolesov, M. Al-Hmoud, J. Tisler, C. Shin, C. Kim, A. Wojcik, P. R. Hemmer, A. Krueger, T. Hanke, A. Leitenstorfer, R. Bratschitsch, F. Jelezko, and J. Wrachtrup. Nanoscale imaging magnetometry with diamond spins under ambient conditions. *Nature*, 455:648–651, 2008. 1

[12] Y. Manassen, R. J. Hamers, J. E. Demuth, and A. J. Castellano Jr. Direct observation of the precession of individual paramagnetic spins on oxidized silicon surfaces. *Phys. Rev. Lett.*, 62:2531–2534, May 1989. 1

[13] C. Durkan and M. E. Welland. Electronic spin detection in molecules using scanning-tunneling- microscopy-assisted electron-spin resonance. *Applied Physics Letters*, 80(3):458–460, 2002. 1

[14] T. Chang and J. G. Zhu. Angular dependence measurement of individual barium ferrite recording particles near the single domain size. *Journal of Applied Physics*, 75(10):5553–5555, 1994. 1

[15] M. Lederman, S. Schultz, and M. Ozaki. Measurement of the dynamics of the magnetization reversal in individual single-domain ferromagnetic particles. *Phys. Rev. Lett.*, 73:1986–1989, Oct 1994. 1

[16] D. Rugar, R. Budakian, H. J. Mamin, and B. W. Chui. Single spin detection by magnetic resonance force microscopy. *Nature*, 430:329–332, 2004. 1

[17] L. Theil Kuhn, A. K. Geim, J. G. S. Lok, P. Hedegård, K. Yllänen, J. B. Jensen, E. Johnson, and P. E. Lindelof. Magnetisation of isolated single crystalline fe-nanoparticles measured by a ballistic hall micro-magnetometer. *Eur. Phys. J. D*, 10(2):259–263, 2000. 1

[18] S. Wirth and S. von Molnar. Hall cross size scaling and its application to measurements on nanometer-size iron particle arrays. *Applied Physics Letters*, 76(22):3283–3285, 2000. 1

[19] Y. Li, P. Xiong, S. von Molnar, S. Wirth, Y. Ohno, and H. Ohno. Hall magnetometry on a single iron nanoparticle. *Applied Physics Letters*, 80(24):4644–4646, 2002. 1

[20] R. F. Voss, R. B. Laibowitz, and A. N. Broers. Niobium nanobridge dc SQUID. *Appl. Phys. Lett.*, 37:656–658, 1980. 1, 4

[21] W. Wernsdorfer. Classical and quantum magnetization reversal studied in nanometersized particles and clusters. *Adv. Chem. Phys.*, 118:99–190, 2001. 1

[22] W. Wernsdorfer. From micro- to nano-SQUIDs: applications to nanomagnetism. *Supercond. Sci. Technol.*, 22:064013, 2009. 1, 4

[23] L. Hao, J. C. Macfarlane, J. C. Gallop, D. Cox, J. Beyer, D. Drung, and T. Schurig. Measurement and noise performance of nano-superconducting-quantum-interference devices fabricated by focused ion beam. *Appl. Phys. Lett.*, 92(19):192507, 2008. 1, 4

[24] B. D. Josephson. The discovery of tunnelling supercurrents. *Rev. Mod. Phys.*, 46:251–254, 1974. 2

[25] SQ100 LTS dc SQUID, PC-100 Single-Channel dc SQUID Electronics System, STAR Cryoelectronics, USA. 2, 8

[26] M. Ketchen, D. Awschalom, W. Gallagher, A. Kleinsasser, R. Sandstrom, J. Rozen, and B. Bumble. Design, fabrication, and performance of integrated miniature SQUID susceptometers. *IEEE Trans. Magn.*, 25:1212–1215, 1989. 2, 17

[27] J. Clarke and A. I. Braginski. *The SQUID Handbook: Fundamentals and Technology of SQUIDs and SQUID Systems*. Wiley-VCH, 1 edition, August 2004. 3, 8

[28] R. Meservey and P. M. Tedrow. Measurements of the kinetic inductance of superconducting linear structures. *Journal of Applied Physics*, 40(5):2028–2034, 1969. 3

[29] G. Testa, E. Sarnelli, S. Pagano, C. R. Calidonna, and M. Mango Furnari. Characteristics of asymmetric superconducting quantum interference devices. *J. Appl. Phys.*, 89:5145, 2001. 3

[30] G. Testa, S. Pagano, E. Sarnelli, C. R. Calidonna, and M. Mango Furnari. Improved superconducting quantum interference devices by resistance asymmetry. *Appl. Phys. Lett.*, 79:2943, 2001. 3

[31] G. Testa, C. Granata, C. DiRusso, S. Pagano, M. Russo, and E. Sarnelli. Low-noise magnetometers with asymmetric superconducting quantum interference devices. *Appl. Phys. Lett.*, 79:3989, 2001. 3

[32] V. Bouchiat. Detection of magnetic moments using a nano-SQUID: limits of resolution and sensitivity in near-field SQUID magnetometry. *Supercond. Sci. Technol.*, 22:064002, 2009. 4

[33] E. Dantsker, S. Tanaka, and J. Clarke. High-T_c super conducting quantum interference devices with slots or holes: Low 1/f noise in ambient magnetic fields. *Applied Physics Letters*, 70(15):2037–2039, 1997. 4

[34] J. Du, D.L Tilbrook, J.C Macfarlane, K.E Leslie, and D.S Ore. Noise performance of hts solid and meshed dc squid magnetometers in external magnetic fields. *Physica C: Superconductivity*, 411(1–2):18 – 24, 2004. 4

[35] C. Granata, E. Esposito, A. Vettoliere, L. Petti, and M. Russo. An integrated superconductive magnetic nanosensor for high-sensitivity nanoscale applications. *Nanotechnology*, 19(27):275501, 2008. 4

[36] A. G. P. Troeman, H. Derking, B. Borger, J. Pleikies, D. Veldhuis, and H. Hilgenkamp. NanoSQUIDs based on niobium constrictions. *Nano Lett.*, 7:2152–2156, 2007. 4

[37] V. Bouchiat, M. Faucher, C. Thirion, W. Wernsdorfer, T. Fournier, and B. Pannetier. Josephson junctions and superconducting quantum interference devices made by local oxidation of niobium ultrathin films. *Appl. Phys. Lett.*, 79:123–125, 2001. 4

[38] M. Faucher, P.-O. Jubert, O. Fruchart, W. Wernsdorfer, and V. Bouchiat. Optimizing the flux coupling between a nanoSQUID and a magnetic particle using atomic force microscope nanolithography. *Supercond. Sci. Technol.*, 22:064010, 2009. 4

[39] A. Finkler, Y. Segev, Y. Myasoedov, M. L. Rappaport, L. Ne'eman, D. Vasyukov, E. Zeldov, M. E. Huber, J. Martin, and A. Yacoby. Self-aligned nanoscale SQUID on a tip. *Nano Lett.*, 10:1046–1049, 2010. 4

[40] A. Sharafiev, I. Soloviev, V. Kornev, M. Schmelz, R. Stolz, V. Zakosarenko, S. Anders, and H.-G. Meyer. Bi-squids with submicron cross-type josephson tunnel junctions. *Superconductor Science and Technology*, 25(4):045001, 2012. 4

[41] J.-P. Cleuziou, W. Wernsdorfer, V. Bouchiat, T. Ondarcuhu, and M. Monthioux. Carbon nanotube superconducting quantum interference device. *Nat Nano*, 1(1):53–59, October 2006. 4

[42] Special section: Focus on nanoSQUIDs and their applications. *Supercond. Sci. Technol.*, 22:064001 to 064013, 2009. 4

[43] D. Hagedorn, O. Kieler, R. Dolata, R. Behr, F. Müller, J. Kohlmann, and J. Niemeyer. Modified fabrication of planar sub-μm superconductor-normal metal-superconductor Josephson junctions for use in a Josephson arbitrary waveform synthesizer. *Supercond. Sci. Technol.*, 19:294–298, 2006. 5, 18

[44] O. F. Kieler, R. Iuzzolino, and J. Kohlmann. Sub- μm SNS Josephson junction arrays for the Josephson arbitrary waveform synthesizer. *Applied Superconductivity, IEEE Transactions on*, 19(3):230 –233, june 2009. 5, 18

[45] O. F Kieler, J. Kohlmann, and F. Müller. Improved design of superconductor/normal conductor/superconductor josephson junction series arrays for an ac josephson voltage standard. *Superconductor Science and Technology*, 20(11):S318, 2007. 5

[46] O. F. Kieler, J. Kohlmann, R. Behr, F. Muller, L. Palafox, and J. Niemeyer. Sns josephson junction series arrays for the josephson arbitrary waveform synthesizer. *Applied Superconductivity, IEEE Transactions on*, 17(2):187 –190, june 2007. 5

[47] J. Tomaschko, S. Scharinger, V. Leca, J. Nagel, M. Kemmler, T. Selistrovski, D. Koelle, and R. Kleiner. Phase-sensitive evidence for $d_{x^2-y^2}$-pairing symmetry in the parent-structure high-T_c cuprate superconductor $Sr_{1-x}La_xCuO_2$. *arXiv:1203.5237v1*, 2012. 10

[48] P. Bushev, D. Bothner, J. Nagel, M. Kemmler, K. B. Konovalenko, A. Loerincz, K. Ilin, M. Siegel, D. Koelle, R. Kleiner, and F. Schmidt-Kaler. Trapped electron coupled to superconducting devices. *Eur. Phys. J. D*, 2011. 11

[49] D. Koelle, R. Kleiner, F. Ludwig, E. Dantsker, and J. Clarke. High-transition-temperature superconducting quantum interference devices. *Rev. Mod. Phys.*, 71:631–686, 1999. 15

[50] H. Hilgenkamp, J. Mannhart, and B. Mayer. Implications of $d_{x^2-y^2}$ symmetry and faceting for the transport properties of grain boundaries in high-T_c superconductors. *Phys. Rev. B*, 53:14586–14593, Jun 1996. 16

[51] E. Il'ichev, V. Zakosarenko, R. P. J. IJsselsteijn, V. Schultze, H.-G. Meyer, H. E. Hoenig, H. Hilgenkamp, and J. Mannhart. Nonsinusoidal current-phase relationship of grain boundary josephson junctions in high- T_c superconductors. *Phys. Rev. Lett.*, 81:894–897, Jul 1998. 16

[52] S. J. Rosner, K. Char, and G. Zaharchuk. Microstructure of biepitaxial grain boundary junctions in $YBa_2Cu_3O_7$. *Applied Physics Letters*, 60(8):1010–1012, 1992. 16

[53] J. A. Alarco, E. Olsson, Z. G. Ivanov, P. Å. Nilsson, D. Winkler, E. A. Stepantsov, and A. Y. Tzalenchuk. Microstructure of an artificial grain boundary weak link in an $YBa_2Cu_3O_{7-\sigma}$ thin film grown on a (100)(110), [001]-tilt Y-ZrO_2 bicrystal. *Ultramicroscopy*, 51(1–4):239 – 246, 1993. 16

[54] J. A. Alarco, E. Olsson, Z. G. Ivanov, D. Winkler, E. A. Stepantsov, O. I. Lebedev, A. L. Vasiliev, A. Y. Tzalenchuk, and N. A. Kiselev. Microstructure and properties of artificial grain boundaries in epitaxial $YBa_2Cu_3O_{7-\delta}$ thin films grown on [001] tilt Y-ZrO_2 bicrystals. *Physica C: Superconductivity*, 247(3–4):263 – 279, 1995. 16

[55] M. Kawasaki, P. Chaudari, T. H. Newman, and A. Gupta. Submicron $YBa_2Cu_3O_{7-\delta}$ grain boundary junction dc SQUIDs. *Appl. Phys. Lett.*, 58:2555–2557, 1991. 16

[56] H. Elsner, R. Ijsselsteijn, W. Morgenroth, H. Roth, and H. G. Meyer. Submicrometer patterning of $YBa_2Cu_3O_{7-x}$. *Microelectron. Eng.*, 41–42:407–410, 1998. 16

[57] D. L. Tilbrook. NanoSQUID sensitivity for isolated dipoles and small spin populations. *Supercond. Sci. Technol*, 22:064003, 2009. 17

[58] M. Khapaev, M. Kupriyanov, E. Goldobin, and M. Siegel. Current distribution simulation for superconducting multi-layered structures. *Supercond. Sci. Technol.*, 16:24–27, 2003. 17

[59] X. Meng, L. Zheng, A. Wong, and T. Van Duzer. Micron and submicron Nb/Al-AlOx/Nb tunnel junctions with high critical current densities. *Applied Superconductivity, IEEE Transactions on*, 11(1):365 –368, mar 2001. 18

[60] G. Testa, A. Monaco, E. Sarnelli, A. D'Agostino, D.-J. Kang, E. J. Tarte, S. H. Mennema, C. Bell, and M. G. Blamire. Submicron $YBa_2Cu_3O_{7-x}$ bicrystal grain boundary junctions by focused ion beam. *Supercond. Sci. Technol.*, 17:287–290, 2004. 20

[61] G. Testa, E. Sarnelli, A. Monaco, E. Esposito, M. Ejmaes, D.-J. Kang, S. H. Mennema, E. J. Tarte, and M. G. Blamire. Evidence of midgap-state-mediated transport in 45° symmetric [001] tilt $YBa_2Cu_3O_{7-x}$ bicrystal grain-boundary junctions. *Phys. Rev. B*, 71:134520, 2005. 20

[62] D. Rugar, H. J. Mamin, and P. Guenther. Improved fiber-optic interferometer for atomic force microscopy. *Appl. Phys. Lett.*, 55:2588, 1989. 22

[63] T. Schwarz et.al. $YBa_2Cu_3O_7$ nanoSQUIDs for detection of small spin systems in high magnetic fields. *unpublished*, 2012. 24, 25

[64] L. Chen, W. Wernsdorfer, C. Lampropoulos, G. Christou, and I. Chiorescu. On-chip SQUID measurements in the presence of high magnetic fields. *Nanotechnol.*, 21:405504, 2010. 25

[65] B. Baek, P. D. Dresselhaus, and S. P. Benz. Co-sputtered amorphous $Nb_x Si_{1-x}$ barriers for josephson-junction circuits. *Applied Superconductivity, IEEE Transactions on*, 16(4):1966 –1970, dec. 2006. 28

[66] D. Olaya, P. D. Dresselhaus, S. P. Benz, A. Herr, Q. P. Herr, A. G. Ioannidis, D. L. Miller, and A. W. Kleinsasser. Digital circuits using self-shunted $Nb/Nb_xSi_{1-x}/Nb$ Josephson junctions. *Applied Physics Letters*, 96(21):213510, 2010. 28

Appended publications

Publication 1

Supercond. Sci. Technol. **24** (2011) 015015 (8pp) doi:10.1088/0953-2048/24/1/015015

Resistively shunted $YBa_2Cu_3O_7$ grain boundary junctions and low-noise SQUIDs patterned by a focused ion beam down to 80 nm linewidth

J Nagel[1], K B Konovalenko[1], M Kemmler[1], M Turad[1], R Werner[1], E Kleisz[2], S Menzel[2], R Klingeler[2], B Büchner[2], R Kleiner[1] and D Koelle[1]

[1] Physikalisches Institut—Experimentalphysik II and Center for Collective Quantum Phenomena, Universität Tübingen, Auf der Morgenstelle 14, D-72076 Tübingen, Germany
[2] Leibniz-Institut für Festkörper- und Werkstoffforschung (IFW) Dresden, D-01171 Dresden, Germany

E-mail: koelle@uni-tuebingen.de

Received 20 September 2010, in final form 29 October 2010
Published 15 December 2010
Online at stacks.iop.org/SUST/24/015015

Abstract

$YBa_2Cu_3O_7$ 24° (30°) bicrystal grain boundary junctions (GBJs), shunted with 60 nm (20 nm) thick Au, were fabricated by focused ion beam milling with widths 80 nm $\leqslant w \leqslant$ 7.8 μm. At 4.2 K we find critical current densities j_c in the 10^5 A cm^{-2} range (without a clear dependence on w) and an increase in resistance times junction area ρ_n with an approximate scaling $\rho_n \propto w^{1/2}$. For the narrowest GBJs $j_c\rho_n = I_cR_n \approx 100\ \mu$V (with critical current I_c and junction resistance R_n), which is promising for the realization of sensitive nanoSQUIDs for the detection of small spin systems. We demonstrate that our fabrication process allows the realization of sensitive nanoscale dc SQUIDs; for a SQUID with $w \approx 100$ nm wide GBJs we find an rms magnetic flux noise spectral density of $S_\Phi^{1/2} \approx 4\ \mu\Phi_0$ Hz$^{-1/2}$ in the white noise limit. We also derive an expression for the spin sensitivity $S_\mu^{1/2}$, which depends on $S_\Phi^{1/2}$, on the location and orientation of the magnetic moment of a magnetic particle to be detected by the SQUID, and on the SQUID geometry. For the unoptimized SQUIDs presented here, we estimate $S_\mu^{1/2} = 390\ \mu_B$ Hz$^{-1/2}$, which could be further improved by at least an order of magnitude.

(Some figures in this article are in colour only in the electronic version)

1. Introduction

There is a growing interest in developing sensitive miniaturized superconducting quantum interference devices (SQUIDs) for the investigation of small spin systems and scanning SQUID microscopy with sub-μm spatial resolution [1–3]. A main motivation is measurements on single nanomagnetic particles, and the ultimate goal is the direct detection of switching of a single electronic spin with various potential applications in spintronics, quantum computing and on biomolecules. Although sensitive spectroscopic techniques for single spin detection, such as magnetic resonance force microscopy, have been developed [4, 5], sensors for the direct detection of the switching of magnetization of small spin systems still have to be improved significantly. Using SQUIDs for this application requires the realization of sub-μm Josephson junctions and SQUID loops, both for optimum inductive coupling to nanosized objects and for improving the SQUID sensitivity for operation at switching fields of the magnetic particles up to the Tesla range at temperatures of $T \approx 4$ K and well below (see the pioneering work by Voss *et al* [6] and more recent work, e.g. [2, 7–12] and references therein). Here, we note that one of the main motivations in the field of direct detection of magnetization reversal of small spin systems is

the investigation of tunneling of magnetization, which however typically can be only observed at temperatures well below 4 K. This means that in this case the envisaged operation temperature for miniaturized SQUIDs is at several 100 mK or even further below [12].

Most frequently used techniques for creating superconducting sub-μm thin film structures are based on electron beam lithography, or on focused ion beam (FIB) patterning. While patterning of sub-μm SQUID loops poses no particular problems, the properties of sub-μm Josephson junctions embedded in the SQUID loop have to be carefully optimized in order to realize low-noise SQUIDs. Here, an important figure of merit is the rms spectral density of flux noise $S_\Phi^{1/2}$, which for optimized SQUIDs based on the standard Nb/AlO_x/Nb technology for μm-sized junctions is in the range of $\mu\Phi_0$ $Hz^{-1/2}$ (Φ_0 is the magnetic flux quantum). However, critical current densities $j_c > 1$ kA cm^{-2} are hard to achieve reliably with this technology, yielding too small critical currents $I_c = j_c A_J$ for junction areas A_J in the $(100\ nm)^2$ range. Therefore, research focused on Nb or Al thin film constriction type junctions (with widths $w \gtrsim 50$ nm), sometimes shunted with a thin film normal metal layer (e. g. Au, or W) to ensure non-hysteretic current–voltage-characteristics (IVCs) [3, 6]. This approach often produced SQUIDs with $S_\Phi^{1/2} \gtrsim 1\ m\Phi_0\ Hz^{-1/2}$, with a few exceptions like the early results by Voss *et al* [6], or the recent work by Hao *et al* [13] who reported on highly sensitive Nb SQUIDs with $S_\Phi^{1/2} \approx 0.2\ \mu\Phi_0\ Hz^{-1/2}$. These encouraging results have been obtained with FIB patterned constriction junctions at $T = 6.8$ K.

For operation in high magnetic fields B a small junction size ($\perp \vec{B}$) is required due to the suppression of I_c with increasing magnetic flux in the junction above several Φ_0, which demands a particularly large j_c. Furthermore, the maximum field of operation is limited by the upper critical field B_{c2}, e.g. to $\lesssim$1 T for typical Nb thin film based SQUIDs. Here, high-transition-temperature (high-T_c) SQUIDs offer three advantages: (i) very high B_{c2} in the tens of Tesla regime or even more, (ii) high $j_c > 10^5$ A cm^{-2} for grain boundary junctions (GBJs) operating at $T = 4.2$ K and well below and (iii) a GBJ geometry with the junction barrier perpendicular to the thin film SQUID loop; this allows the application of very large in-plane fields (for switching the magnetization of nanoparticles) which do not couple to the SQUID and which do not reduce I_c. Here, the challenge is to produce sub-μm GBJs with high quality, in particular with high j_c and $\rho_n = R_n A_J$, where R_n is the junction resistance, i.e. with high $j_c\rho_n = I_c R_n$.

At this point, we should mention that, in principle, also constriction type junctions based on HTS, or MgB_2 thin films may fulfill the above mentioned requirements, and in fact such junctions and SQUIDs based on them have been patterned by FIB [14–18]. However, these junctions typically show flux-flow type or hysteretic IVCs at low T, such that their operation temperature is often limited to a narrow T range well above 4 K, and their performance with respect to flux noise so far has never reached the performance of high-T_c low-noise GBJ SQUIDs [19]. Furthermore, we note that due to the small lower critical fields B_{c1}, HTS thin film SQUIDs will be in the mixed state, and strong pinning of vortices will be important, in order to keep low-frequency noise due to vortex motion as small as possible. However, the same applies to, e.g., Nb SQUIDs if they are operated above B_{c1}; this issue has not been studied so far, since SQUIDs usually are operated at the magnetic field of the earth or well below.

Already in the 1990s thin film high-T_c $YBa_2Cu_3O_7$ (YBCO) sub-μm GBJs and SQUIDs have been fabricated using e-beam lithography [20, 21]. However, oxygen loss during processing, in particular for very thin films, may require post-deposition annealing to improve junction characteristics [22]. More recently, sub-μm YBCO GBJs have also been fabricated by FIB [23], and both technologies enabled fundamental studies on transport and noise in high-T_c sub-μm GBJs [22, 24–26]. Still, a significant degradation of j_c for $w \lesssim 500$ nm was found [20, 21, 23], and the use of deep sub-μm GBJs for the realization of nanoSQUIDs has not been explored yet. The motivation for the realization of sub-μm GBJs with widths well below 500 nm is based on the following considerations: first of all, operation in high magnetic fields in the Tesla range, as mentioned above, requires very accurate alignment of the applied magnetic field in the thin film plane in order to reduce coupling of the applied out-of-field component to the GBJ. This requires as small as possible GBJ widths. Furthermore, as will be shown below, the spin sensitivity scales linearly with the rms flux noise $S_\Phi^{1/2}$ of the SQUID. Optimization of $S_\Phi^{1/2}$ requires an as small as possible SQUID loop inductance L [27], i.e. minimization of the dimensions of the SQUID loop, which for topological reasons has to be intersected by the grain boundary. Here, SQUID loop sizes of the order of 100 nm seem to be feasible, according to our experience on FIB patterning of our devices as described below. In order to ensure optimum SQUID performance, one should achieve at least a few SQUID modulations within the Fraunhofer-like $I_c(B)$ modulation of the single GBJs. This in turn requires also shrinking the GBJ widths down to the size of the SQUID loop. Hence, our goal is to demonstrate the feasibility of FIB patterning YBCO GBJs down to junction widths of the order of 100 nm. In order to accomplish this, we investigated the scaling behavior of YBCO GBJ properties with linewidths ranging over two orders of magnitude, from $\sim$8 μm down to 80 nm, and we investigated the electric transport and noise properties of YBCO GBJ dc SQUIDs with the smallest linewidths achieved within this study. We note that we performed so far only investigations on low-field properties of the fabricated GBJs and SQUIDs, as we are at this stage interested in clarifying the intrinsic scaling properties of our devices with GBJ width, although the ultimate goal of this work is to operate such SQUIDs in high magnetic fields in the Tesla range at $T = 4.2$ K and well below.

The remainder of this paper is organized as follows. Section 2 very briefly addresses sample fabrication and layout, including some information on the quality of our YBCO thin films. In section 3 we first describe and discuss the results of electric transport properties of our shunted GBJs, with focus on their dependence on junction width, which was varied over two orders of magnitude (3.1). The second part

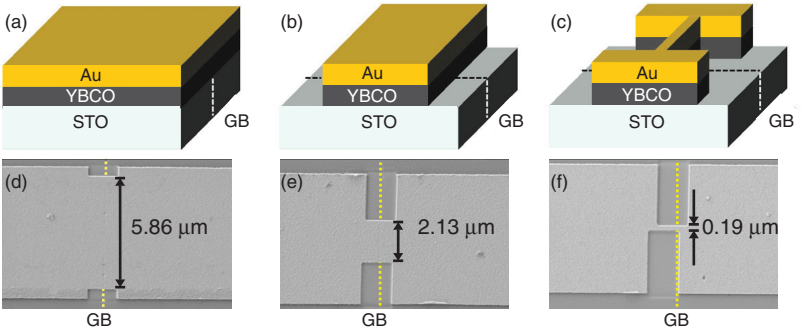

Figure 1. Upper row: schematic illustration of the steps used for fabricating YBCO grain boundary junctions (GBJs). (a) *In situ* deposition of a YBCO/Au bilayer on a bicrystal STO substrate; (b) patterning of 8 μm wide bridges straddling the grain boundary (GB) (by photolithography and Ar ion milling); (c) patterning of a narrow GBJ by FIB. The location of the GB is indicated by dashed lines. The bottom row (d)–(f) shows scanning electron microscopy images of three single junction devices (from *chip-1*) with different widths (indicated on the graphs).

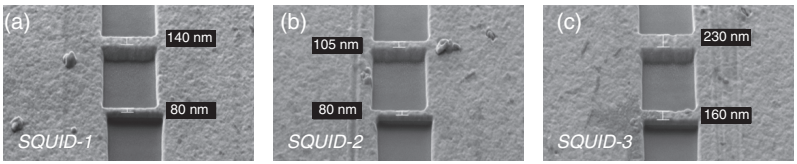

Figure 2. SEM images of the three SQUIDs (loop size 1.0 × 1.2 μm^2) fabricated on *chip-2*. Labels in black boxes give junction widths.

(3.2) of this section describes the results obtained for our SQUIDs, with focus on electric transport and noise properties of the SQUID with the smallest GBJ width used in this study (*SQUID-2*). Having characterized our SQUIDs, we discuss in section 4 the important relation between the flux noise $S_\Phi^{1/2}$ of the SQUIDs and the spin sensitivity $S_\mu^{1/2}$, which is the important figure of merit for detection of small spin particles. Here, we provide a solution for calculating the spin sensitivity for any arbitrary geometry of the SQUID loop as a function of position and orientation of the magnetic moment of a small particle to be detected. We then apply this solution to the particular geometry of *SQUID-2* and finally discuss perspectives for further optimization of $S_\mu^{1/2}$. Section 5 contains our conclusions.

2. Sample fabrication

We fabricated devices on $SrTiO_3$ (STO) symmetric [001] tilt bicrystal substrates with misorientation angle $\theta = 30°$ (*chip-1*) and 24° (*chip-2*). Figures 1(a)–(c) illustrate the fabrication steps. We deposited $d_Y = 50$ nm thick *c*-axis oriented epitaxially grown YBCO by pulsed laser deposition (PLD), followed by *in situ* evaporation of Au (at room temperature) with thickness $d_{Au} = 20$ nm (*chip-1*) and 60 nm (*chip-2*), serving as a resistive shunt and protection layer during FIB milling. For details on PLD growth of our YBCO films on STO substrates, and their structural and electric transport properties, see [28]. In brief, our 50 nm thick YBCO films typically yield 0.1° full width half maximum of the rocking curve at the (005) x-ray diffraction peak, have $T_c = 91$ K with a transition width ∼0.5 K and normal state resistivity $\rho \approx 50$ $\mu\Omega$ cm at $T = 100$ K. On both chips, 8 μm wide bridges straddling the grain boundary were fabricated by photolithography and Ar ion milling and then patterned by FIB with Ga ions (50 pA, 30 kV) to make junctions and dc SQUIDs with junction widths 80 nm $\leqslant w \leqslant$ 7.8 μm. FIB patterning was performed with a dual beam 1540 XB cross beam (Zeiss). This allowed us to apply an optimized FIB cut procedure (soft FIB procedure), with small ion current density and minimum ion exposure time of non-milled areas, i.e. only very brief snapshot imaging prior to milling. Even for imaging by the electron beam, we minimized the exposure time in order to avoid damage of our FIB cut bridges. Figures 1(d)–(f) show scanning electron microscopy (SEM) images of three GBJs fabricated on *chip-1*. In total, we investigated 22 single GBJs and three dc SQUIDs (on *chip-2*; hole size 1.0 × 1.2 μm^2). SEM images of the three SQUIDs are shown in figure 2.

3. Experiments

We characterized our devices at $T = 4.2$ K in a magnetically shielded environment. All results shown below have been

obtained under these conditions. For measurements of IVCs, $I_c(B)$ and $V(B)$ we used a four-point arrangement with a room temperature voltage amplifier. For SQUID noise measurements we preamplified the output signal with a Nb dc SQUID amplifier with 0.1 nV Hz$^{-1/2}$ resolution. For noise measurements, the YBCO SQUID was operated open-loop, i.e. we applied a constant bias current and constant flux bias, and we detected the voltage across the SQUID by connecting voltage leads to the input coil which was inductively coupled to a Nb dc SQUID; a 10 Ω resistor (also at 4.2 K) was in series with the input coil. The Nb SQUID was read out in a flux-locked loop with ac flux bias at modulation frequency $f_{\rm mod} = 256$ kHz (PC-1000 Multi-Channel dc SQUID Electronics System with SQ100 SQUID-Sensor from STAR Cryoelectronics).

3.1. Transport properties versus junction width

All devices showed resistively-and-capacitively-shunted-junction (RCSJ)-type IVCs, which for some of the sub-μm junctions on *chip-1* (thinner Au shunt) had a small hysteresis. Therefore, for *chip-2*, we increased $d_{\rm Au}$ by a factor of three, yielding non-hysteretic IVCs, except for the 530 nm wide junction, which has an exceptionally high $j_c\rho_n$. From the IVCs we determined I_c, and R_n, and calculated j_c and ρ_n, using $d_Y = 50$ nm and w as obtained from SEM images. The results of these measurements are summarized in figure 3, plotted versus w which spans two orders of magnitude. The full symbols in figure 3 show data obtained after FIB patterning; the open symbols show data (for *chip-2*) from the 8 μm wide bridges prior to FIB patterning.

Figure 3(a) shows $j_c(w)$, which is well above 10^5 A cm^{-2} over the entire range of w. The j_c values shown are typical for $\theta = 24°$ and 30° YBCO GBJs at 4.2 K and $w \gtrsim 2$ μm [19]; however, such high j_c values have not been previously observed for widths down to 80 nm. We do find a significant scattering of $j_c(w)$, however without a clear width dependence. The average j_c for *chip-2* is 1.5 times the one for *chip-1*, as expected from the scaling $j_c(\theta)$ of GBJs [29]. The comparison of j_c of the same bridges before and after FIB patterning shows that for most devices j_c even slightly increased after FIB patterning. The positions of the devices on *chip-2* (along the GB of the substrate) are ordered according to their device number (1–15) (cf top axis of figure 3(a)) from the left to the right edge of the substrate. There is a clear trend of increasing j_c by about a factor of two (for the 8 μm wide bridges) along the entire substrate. The origin of this gradient in j_c has not been clarified; however we can rule out a corresponding variation in the YBCO film thickness across the substrate. A possible explanation for the observed gradient in j_c of the 8 μm wide GBJs along *chip-2* could be a gradient in the quality of the GB in the bicrystal substrate, which in turn can cause a gradient in the barrier thickness of the GBJs along the chip.

Figure 3(b) shows an approximate scaling $\rho_n \propto \sqrt{w}$ of unclear origin. We note that the lines shown in figures 3(b) and (c) are not fits to our data. These lines are just drawn to illustrate the trend of decreasing resistivity ρ_n with decreasing

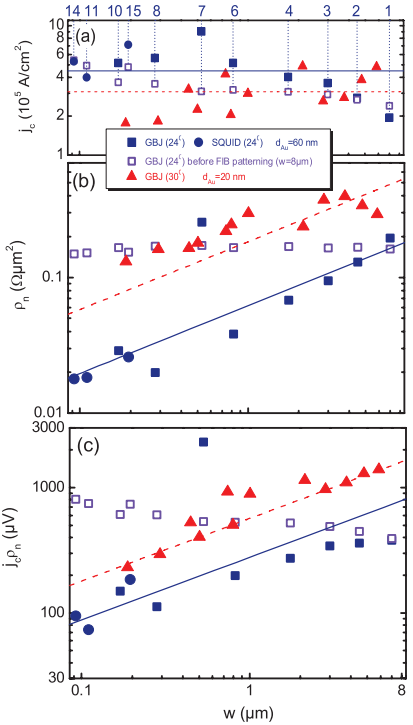

Figure 3. Transport data of YBCO GBJs and SQUIDs versus junction width w (solid symbols): (a) critical current density $j_c(w)$; (b) junction resistance times area $\rho_n(w)$; (c) $j_c\rho_n(w)$. Dashed (solid) lines indicate average j_c values (in (a)) and approximate scaling of $\rho_n(w)$ (in (b)) and $j_c\rho_n(w)$ (in (c)) for *chip-1* (*chip-2*). Open squares are data for the same GBJs on *chip-2*, measured prior to FIB patterning (i.e. $w = 8$ μm). The numbers on the top axis in (a) label the device numbers on *chip-2*.

junction width w. Before FIB patterning, the 8 μm wide GBJs on *chip-2* all had $\rho_n \approx 0.17\,\Omega\ \mu$m^2, which falls onto the observed $\rho_n(w)$ dependence, indicating that this scaling is not specific to FIB patterned GBJs. Furthermore, $\rho_n \approx 0.17\,\Omega\ \mu$m^2 is an order of magnitude below typical values for unshunted GBJs [29], which we attribute to the Au shunt, and which is also consistent with the larger ρ_n of GBJs on *chip-1* with thinner Au. For *chip-1*, $d_{\rm Au} = 20$ nm is close to the 15 nm implantation depth of 30 keV Ga ions in Au [30]. Hence one might expect that FIB induces an increase in the Au resistivity via Ga implantation. This effect should be suppressed for *chip-2* with three times thicker Au. In any case, it is hard to explain why Ga implantation should increase ρ_n for wider junctions. Certainly, Ga implantation is not the only detrimental effect of FIB patterning. In particular, the Ga beam might destroy the crystalline order close to the patterned edges. However, our

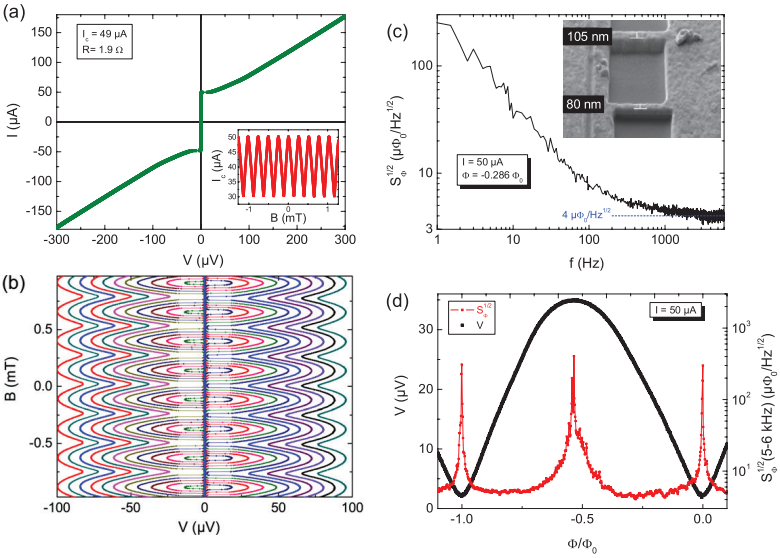

Figure 4. Transport and noise characteristics of *SQUID-2*. (a) IVC at $B = 0$; the inset shows $I_c(B)$. (b) $V(B)$ for $I = -70.8$ to -12.3 and 10.0–68.5 μA (in 3.9 μA steps). (c) Spectral density of rms flux noise $S_\Phi^{1/2}(f)$; inset: SEM image of the SQUID. (d) $V(\Phi)$ and $S_\Phi^{1/2}(\Phi)$ (averaged from $f = 5$ to 6 kHz).

experimental observation of almost constant j_c for GBJ widths down to 80 nm rules out severe edge damage effects on a length scale of several tens of nm. This observation also rules out such effects as a possible explanation for the observed scaling behavior of $\rho_n(w)$. Certainly, the optimization of the transport properties of our shunted YBCO GBJs needs further detailed analysis, such as, e.g., shown in [31].

Figure 3(c) shows $j_c\rho_n(w) \approx 0.1$–1 mV, i.e. at least one order of magnitude below the values for unshunted YBCO GBJs of comparable j_c. This is certainly due to the suppression of $j_c\rho_n$ by the Au shunt required to ensure non-hysteretic IVCs at 4.2 K. The decrease of $j_c\rho_n$ with decreasing w is due to the scaling of $\rho_n(w)$ mentioned above. Still, even for the 80 nm wide GBJs we find reasonable values of $j_c\rho_n$ around 100 μV, which are certainly quite suitable for the realization of sensitive SQUIDs.

3.2. SQUID parameters, transport characteristics and noise performance

The results of transport measurements on all three SQUIDs (on *chip-2*) are summarized in table 1. The SQUID inductance L was calculated with the numerical simulation software 3D-MLSI [32], which is based on a finite element method to solve the London equations for a given film thickness and London penetration depth ($d_Y = 50$ nm and $\lambda_L = 140$ nm, respectively, in our case). As $d_Y \ll \lambda_L$, the kinetic inductance contributes significantly to L. For *SQUID-1* and *SQUID-2*, the GBJ widths w_i ($i = 1, 2$) are below λ_L, which increases L over that of *SQUID-3* with wider junctions. From the calculated L and measured I_c we obtain $\beta_L \equiv LI_c/\Phi_0 \approx 0.3$–0.7, i.e. not far from the optimum value $\beta_L \approx 1$ [33]. The transfer function V_Φ, i.e. the slope of the $V(\Phi)$ curves at optimum bias current and applied flux $\Phi = \pm\frac{1}{4}\Phi_0$, is around 0.1 mV/$\Phi_0$, and the effective area $A_{\rm eff} = \Phi/B \approx 8$ μm^2 for all three SQUIDs.

Table 1. Parameters of YBCO GBJ dc SQUIDs.

#	w_1 (nm)	w_2 (nm)	I_c (μA)	R_n (Ω)	I_cR_n (μV)	L (pH)	β_L	V_Φ (mV/Φ_0)
1	80	140	44	1.7	73	15	0.31	0.08
2	80	105	49	1.9	94	16	0.38	0.11
3	160	230	139	1.3	185	10	0.66	0.13

Figure 4 shows electric transport and noise data obtained for *SQUID-2* (the device with smallest w; see inset in (c)). Figure 4(a) shows an IVC for an applied field $B = 0$ corresponding to a maximum in I_c. The small jump at I_c to $V \neq 0$ indicates that the junctions are at the transition to the underdamped regime. The inset in figure 4(a) shows $I_c(B)$ with 40% modulation. Figure 4(b) shows $V(B)$ for various bias currents I. The small shift in the minima of $V(B)$ upon reversing I is in accordance with the I_c asymmetry of the two GBJs due to their different widths.

Finally, graphs (c) and (d) in figure 4 show the results of noise measurements on *SQUID-2*. Figure 4(c) shows the rms spectral density of flux noise $S_\Phi^{1/2}(f) \propto f^{-x}$ for optimum

flux bias $\Phi = -0.286\Phi_0$ with $x \approx 0.8$ for frequencies $f \lesssim 100$ Hz. The relatively small width (8 μm) of the structures adjacent to the SQUID (cooled and operated in magnetically shielded environment) makes it quite unlikely that Abrikosov vortices are trapped there and cause excess low-frequency noise due to vortex hopping. Instead, it is much more likely that the excess low-frequency noise is due to I_c fluctuations in the GBJs [19]. For larger f we find a white flux noise level $S_{\Phi,w}^{1/2} \approx 4\ \mu\Phi_0\ \mathrm{Hz}^{-1/2}$, which to our knowledge is the lowest value of $S_\Phi^{1/2}$ obtained for a YBCO dc SQUID with sub-μm GBJs so far. Figure 4(d) shows the rms flux noise $S_\Phi^{1/2}$ (averaged from $f = 5$ to 6 kHz) and the SQUID voltage V versus applied flux Φ. We find a rather shallow minimum in $S_\Phi^{1/2}(\Phi)$ for an applied flux where the slope of the $V(\Phi)$ curve (also shown in graph (d)) is close to its maximum. We note that the need to resistively shunt the junctions for low-T operation leads to a reduction in $I_c R_n$, which in turn reduces the transfer function $V_\Phi \propto R_n$ and also increases the flux noise $S_\Phi \propto 1/R$ of the SQUIDs. On the other hand, operation at lower T will reduce the Nyquist noise from the shunt resistors and hence improve S_Φ [34]. Certainly, the optimization of the flux noise of the SQUIDs will require further analysis, e.g. by comparing experimental results with numerical simulations based on the RCSJ model [19, 34].

4. Spin sensitivity

Coming back to the main motivation of this work, i.e. the development of nanoSQUIDs for the detection of small spin systems, we derive an expression for the spin sensitivity $S_\mu^{1/2}$, which we then use to calculate $S_\mu^{1/2}$ for the particular geometry and flux noise of *SQUID-2* as a function of the position of a magnetic particle for a given orientation of its magnetic moment. S_μ is the spectral density of spin noise, which depends on the spectral density of flux noise S_Φ of the SQUID and on the coupling between a magnetic particle with magnetic moment $\vec{\mu} = \mu \cdot \hat{e}_\mu$ and the SQUID via the relation $S_\mu = S_\Phi/\phi_\mu^2$. Here, $\phi_\mu(\hat{e}_\mu, \vec{r}_\mu) \equiv \Phi_\mu(\vec{\mu}, \vec{r}_\mu)/\mu$ is the magnetic flux Φ_μ per magnetic moment μ coupled into the SQUID loop by the magnetic particle, which is located at the position $\vec{r}_\mu$ and which is oriented along $\hat{e}_\mu$. This means that, in order to determine $S_\mu^{1/2}$ for a given $S_\Phi^{1/2}$, one needs to calculate the coupling function $\phi_\mu(\hat{e}_\mu, \vec{r}_\mu)$, which will also depend on the SQUID geometry.

To determine ϕ_μ, we assume that the magnetic moment $\vec{\mu}$ is moved from a distance far away to a position $\vec{r} = \vec{r}_\mu$ close to the SQUID loop. When the magnetic moment approaches $\vec{r}_\mu$, a circulating current $I_\mu(\vec{\mu}, \vec{r}_\mu)$ is induced in the SQUID loop, which compensates the coupled flux Φ_μ, due to the diamagnetic response of the SQUID loop. The magnetic field energy stored in the loop of inductance L is $W_{\mathrm{loop}} = \frac{1}{2} L I_\mu^2$. The work required to place the particle in the magnetic field $\vec{B}_\mu(\vec{r})$ produced by the circulating current I_μ is $W_\mu = -\frac{1}{2}\vec{\mu} \cdot \vec{B}_\mu(I_\mu, \vec{r}_\mu)$. We note that $W_\mu > 0$, due to the diamagnetic response of the SQUID loop. Hence, the total work required to bring the magnetic particle to the position $\vec{r}_\mu$ is

$$W_1 = W_{\mathrm{loop}} + W_\mu = \tfrac{1}{2} L I_\mu^2 - \tfrac{1}{2}\vec{\mu} \cdot \vec{B}_\mu(I_\mu, \vec{r}_\mu). \qquad (1)$$

On the other hand, instead of the SQUID, we may consider a fixed current system producing the same field $\vec{B}_\mu(I_\mu, \vec{r}_\mu)$ as the SQUID, when the particle is in its final position r_μ. In this case, the particle has a (positive) energy

$$W_2 = -\vec{\mu} \cdot \vec{B}_\mu(I_\mu, \vec{r}_\mu). \qquad (2)$$

From $W_1 = W_2$ we obtain $I_\mu^2 = -\vec{\mu} \cdot \vec{B}_\mu / L$. With $\Phi_\mu = L I_\mu$ and with $\vec{B}_\mu / I_\mu = \vec{B}/I \equiv \vec{b}$ one thus obtains

$$\frac{\Phi_\mu(\vec{\mu}, \vec{r}_\mu)}{\mu} \equiv \phi_\mu(\hat{e}_\mu, \vec{r}_\mu) = -\hat{e}_\mu \cdot \vec{b}(\vec{r}_\mu), \qquad (3)$$

where I is an arbitrary current circulating in the SQUID loop, which generates the magnetic field $\vec{B}(I)$ at the position $\vec{r}_\mu$ of the magnetic particle.

Equation (3) reproduces the results of [8, 10, 35], derived for a circular filamentary SQUID loop. Moreover, equation (3) provides a solution of the problem, valid for any *arbitrary* geometry of the superconducting loop, if one can find the normalized magnetic field distribution $\vec{b}(\vec{r})$ outside the SQUID loop. For a given $\vec{b}(\vec{r})$ (determined by the SQUID geometry only) and given flux noise, one can use equation (3) to easily calculate the spin sensitivity $S_\mu^{1/2} = S_\Phi^{1/2}/\phi_\mu$ for any orientation $\hat{e}_\mu$ and location of the magnetic particle.

For the geometry of *SQUID-2*, we calculated the spatial distribution of the current density in the SQUID loop and the corresponding three-dimensional magnetic field distribution $\vec{b}(\vec{r})$ outside the SQUID loop with 3D-MLSI [32]. Figure 5 shows the resulting spin sensitivity of *SQUID-2* (with $S_\Phi^{1/2} = 4\,\mu\Phi_0\ \mathrm{Hz}^{-1/2}$) for the detection of a magnetic particle located in the (x, z) plane (at $y = 0$) with its magnetic moment pointing along the x direction, i.e. $\hat{e}_\mu = \hat{e}_x$. That is, the magnetic moment of the particle is aligned parallel to the thin film plane of the SQUID, and perpendicular to the current through the GBJs.

The contour plot of the spin sensitivity shows clear minima right above the superconducting bridges straddling the grain boundary. The upper graph shows a line scan $S_\mu^{1/2}(x)$ of the spin sensitivity at a height $z = d_{\mathrm{Au}} + d_{\mathrm{Y}}/2 = 85$ nm above the ring (i.e. for our SQUID the minimum vertical distance due to the Au layer on top of the YBCO film). The lowest value of the spin sensitivity along this line scan is 390 $\mu_{\mathrm{B}}\ \mathrm{Hz}^{-1/2}$, which could be further improved by reducing the thickness of the Au layer. This can be done even without affecting the GBJ properties if the Au layer is not removed right above the GBJ. Removing the gold layer (and placing the magnetic particle at $z = d_{\mathrm{Y}}/2 = 25$ nm) would improve $S_\mu^{1/2}$ by more than a factor of two down to 180 $\mu_{\mathrm{B}}\ \mathrm{Hz}^{-1/2}$, as can be seen in the right graph, which shows the vertical dependence $S_\mu^{1/2}(z)$ at $x = 0.63$ μm, i.e. right above the center of the YBCO bridge. Moreover, further improvements in $S_\mu^{1/2}$ are feasible by improving $S_\Phi^{1/2}$, which is by no means optimized for the SQUIDs presented here. For example, our FIB technology allows for a reduction in the size of the SQUID loop down to $\sim$100 nm and a concomitant reduction in SQUID inductance L down to $\sim$1 pH. This, in turn, can lead to a significant improvement in $S_\Phi^{1/2}$ by at least an order of magnitude, which would bring $S_\mu^{1/2}$ down to $\approx$20 $\mu_{\mathrm{B}}\ \mathrm{Hz}^{-1/2}$.

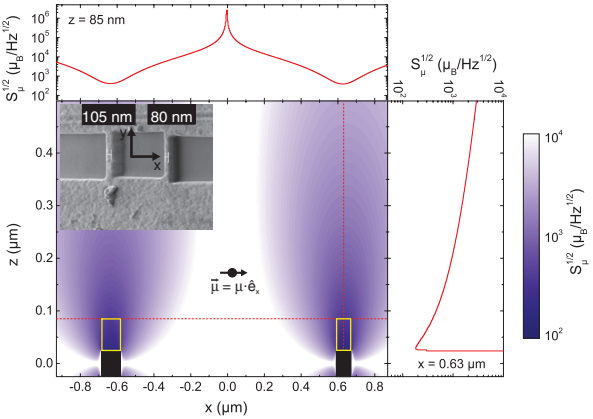

Figure 5. Calculated spin sensitivity $S_\mu^{1/2}$ for *SQUID-2* with $S_\Phi^{1/2} = 4\ \mu\Phi_0\ \mathrm{Hz}^{-1/2}$ for the detection of the magnetic moment of a small spin particle aligned along the x axis in the (x, y) plane of the SQUID loop (cf inset in main graph). The main graph shows a contour plot of $S_\mu^{1/2}$ as a function of the position of the particle in the (x, z) plane at $y = 0$. The location of the YBCO bridges is indicated by the black rectangles; the rectangles (yellow lines) on top of them indicate the position of the Au layer. The line scan above the main graph shows $S_\mu^{1/2}(x)$ for $z = 85$ nm, and the line scan to the right of the main graph shows $S_\mu^{1/2}(z)$ for $x = 0.63\ \mu$m. The locations of these line scans are indicated by the dashed (red) lines in the main graph.

5. Conclusions

In conclusion, we have fabricated YBCO grain boundary junctions and dc SQUIDs by FIB patterning with junction widths ranging from 7.8 μm down to 80 nm. Using an Au thin film shunt on top of the junctions, we achieved non-hysteretic current–voltage-characteristics for operation of YBCO dc SQUIDs at 4.2 K and below. We demonstrated that FIB pattering enables the fabrication of deep sub-μm GBJs without degradation of critical current densities, and comparable to GBJs with widths above 1 μm. We do find a systematic dependence of the resistance times area ρ_n of our GBJs, which scales approximately with the junction width w as $\rho_n \propto \sqrt{w}$. The origin of this scaling could not be resolved and requires further studies. Still, we obtain values of $I_c R_n$ for our GBJs around 100 μV for junctions on the 100 nm scale, which is promising for the fabrication of sensitive nanoSQUIDs. We demonstrated low-noise performance for such devices in the $\mu\Phi_0\ \mathrm{Hz}^{-1/2}$ range, which still can be improved significantly, in particular by reducing the size of the SQUID loop and hence the SQUID inductance, and which makes them promising candidates for applications in magnetic nanoparticle detection and measurements at high magnetic fields. Certainly, the next step will be to investigate the electric transport and noise properties of optimized YBCO nanoSQUIDs in strong magnetic fields, up to above 1 T. Several issues may play an important role here, like low-frequency excess noise due to motion of Abrikosov vortices, or proper alignment of the large applied (in-plane) magnetic field, which should be perpendicular to the plane of the grain boundary in order to avoid suppression of the critical current. In the latter case, the impact of faceting of the GBJs [29] may also become important, which has to be studied in high fields. Our very preliminary studies of high-field operation of YBCO GBJ SQUIDs with 2 μm wide junctions demonstrate that such devices can operate in large in-plane fields of 1 T [36]. The presented solution for calculating the spin sensitivity for arbitrary SQUID geometries—as a function of position and orientation of the magnetization of small spin particles—provides an important tool for the systematic optimization of the spin sensitivity using nanoSQUIDs as sensitive devices for direct detection of magnetization switching of small spin particles. If the expected spin sensitivity for optimized YBCO GBJ SQUIDs can be reached at strong magnetic fields, these sensors should be clearly superior to commonly used Hall sensors [5].

Acknowledgments

We gratefully acknowledge Thomas Dahm for helpful discussions. J Nagel and M Kemmler acknowledge support by the Carl-Zeiss Stiftung, K Konovalenko acknowledges support by the Otto Benecke Stiftung and R Werner acknowledges support by the Cusanuswerk, Bischöfliche Studienförderung. This work was funded by the Deutsche Forschungsgemeinschaft (DFG) via the SFB/TRR 21.

References

[1] Wernsdorfer W, Mailly D and Benoit A 2000 Single nanoparticle measurement techniques *J. Appl. Phys.* **87** 5094–6

[2] Gallop J 2003 SQUIDs: some limits to measurement *Supercond. Sci. Technol.* **16** 1575–82

[3] Foley C P and Hilgenkamp H 2009 Why nanoSQUIDs are important: an introduction to the focus issue *Supercond. Sci. Technol.* **22** 064001

[4] Rugar D, Budakian R, Mamin H J and Chui B W 2004 Single spin detection by magnetic resonance force microscopy *Nature* **430** 329–32

[5] Degen C 2008 Nanoscale magnetometry: microscopy with single spins *Nat. Nanotechnol.* **3** 643–4

[6] Voss R F, Laibowitz R B and Broers A N 1980 Niobium nanobridge dc SQUID *Appl. Phys. Lett.* **37** 656–8

[7] Troeman A G P, Derking H, Borger B, Pleikies J, Veldhuis D and Hilgenkamp H 2007 NanoSQUIDs based on niobium constrictions *Nano Lett.* **7** 2152–6

[8] Granata C, Esposito E, Vettoliere A, Petti L and Russo M 2008 An integrated superconductive magnetic nanosensor for high-sensitivity nanoscale applications *Nanotechnology* **19** 275501

[9] Bouchiat V 2009 Detection of magnetic moments using a nano-squid: limits of resolution and sensitivity in near-field squid magnetometry *Supercond. Sci. Technol.* **22** 064002

[10] Tilbrook D L 2009 Nano SQUID sensitivity for isolated dipoles and small spin populations *Supercond. Sci. Technol.* **22** 064003

[11] Vohralik P F and Lam S K H 2009 NanoSQUID detection of magnetization from ferritin nanoparticles *Supercond. Sci. Technol.* **22** 064007

[12] Wernsdorfer W 2009 From micro- to nano-SQUIDs: applications to nanomagnetism *Supercond. Sci. Technol.* **22** 064013

[13] Hao L, Macfarlane J C, Gallop J C, Cox D, Beyer J, Drung D and Schurig T 2008 Measurement and noise performance of nano-superconducting-quantum-interference devices fabricated by focused ion beam *Appl. Phys. Lett.* **92** 192507

[14] Blank D H A, Booij W, Hilgenkamp H, Vulink B, Veldhuis D and Rogalla H 1995 $YBa_2Cu_3O_7$ nano-bridge junctions and dc SQUIDs made by focused ion beam milling *IEEE Trans. Appl. Supercond.* **5** 2786–9

[15] Pedyash M V, Blank D H A and Rogalla H 1996 Superconducting quantum interference devices based on YBaCuO nanobridges *Appl. Phys. Lett.* **68** 1156–8

[16] Brinkman A, Veldhuis D, Mijatovic D, Rijnders G, Blank D H A, Hilgenkamp H and Rogalla H 2001 Superconducting quantum interference device based on MgB_2 nanobridges *Appl. Phys. Lett.* **79** 2420

[17] Burnel G, Kang D-J, Ansell D A, Lee H-N, Moon S-H, Tarte E J and Blamire M G 2002 Directly coupled superconducting quantum interference device magnetometer fabricated in magnesium diboride by focused ion beam *Appl. Phys. Lett.* **81** 102

[18] Wu C H, Chou Y T, Kuo W C, Chen J H, Wang L M, Chen J C, Chen K L, Sou U C, Yang H C and Jeng J T 2008 Fabrication and characterization of high-T_c $YBa_2Cu_3O_{7-x}$ nanoSQUIDs made by focused ion beam milling *Nanotechnology* **19** 315304

[19] Koelle D, Kleiner R, Ludwig F, Dantsker E and Clarke J 1999 High-transition-temperature superconducting quantum interference devices *Rev. Mod. Phys.* **71** 631–86

[20] Kawasaki M, Chaudari P, Newman T H and Gupta A 1991 Submicron $YBa_2Cu_3O_{7-\delta}$ grain boundary junction dc SQUIDs *Appl. Phys. Lett.* **58** 2555–7

[21] Elsner H, Ijsselsteijn R, Morgenroth W, Roth H and Meyer H G 1998 Submicrometer patterning of $YBa_2Cu_3O_{7-x}$ *Microelectron. Eng.* **41/42** 407–10

[22] Herbstritt F, Kemen T, Alff L, Marx A and Gross R 2001 Transport and noise characteristics of submicron high-temperature superconductor grain-boundary junctions *Appl. Phys. Lett.* **78** 955

[23] Testa G, Monaco A, Sarnelli E, D'Agostino A, Kang D-J, Tarte E J, Mennema S H, Bell C and Blamire M G 2004 Submicron $YBa_2Cu_3O_{7-x}$ bicrystal grain boundary junctions by focused ion beam *Supercond. Sci. Technol.* **17** 287–90

[24] Il'ichev E *et al* 2001 Degenerate ground state in a mesoscopic $YBa_2Cu_3O_{7-x}$ grain boundary Josephson junction *Phys. Rev. Lett.* **86** 5369–72

[25] Tzalenchuk A Ya, Lindström T, Charlebois S A, Stepantsov E A, Ivanov Z and Zagoskin A M 2003 Mesoscopic Josephson junctions of high-T_c superconductors *Phys. Rev.* B **68** 100501(R)

[26] Testa G, Sarnelli E, Monaco A, Esposito E, Ejmaes M, Kang D-J, Mennema S H, Tarte E J and Blamire M G 2005 Evidence of midgap-state-mediated transport in 45° symmetric [001] tilt $YBa_2Cu_3O_{7-x}$ bicrystal grain-boundary junctions *Phys. Rev.* B **71** 134520

[27] Tesche C D and Clarke J 1977 DC SQUID: noise and optimization *J. Low Temp. Phys.* **29** 301–31

[28] Werner R *et al* 2010 $YBa_2Cu_3O_7/La_{0.7}Ca_{0.3}MnO_3$ bilayers: interface coupling and electric transport properties *Phys. Rev.* B **82** 224509

[29] Hilgenkamp H and Mannhart J 2002 Grain boundaries in high-T_c superconductors *Rev. Mod. Phys.* **74** 485

[30] Rubanov S and Munroe P R 2003 The effect of the gold sputter-coated films in minimising damage in FIB-produced TEM specimens *Mater. Lett.* **57** 2238–41

[31] Klushin A, Golubov A, Prusseit W and Kohlstedt H 1997 Comparative study of shunted bicrystal Josephson junctions *J. Low Temp. Phys.* **106** 265–9

[32] Khapaev M, Kupriyanov M, Goldobin E and Siegel M 2003 Current distribution simulation for superconducting multi-layered structures *Supercond. Sci. Technol.* **16** 24–7

[33] Kleiner R, Koelle D, Ludwig F and Clarke J 2004 Superconducting QUantum interference devices: state-of-the-art and applications *Proc. IEEE* **92** 1534–48

[34] Chesca B, Kleiner R and Koelle D 2004 SQUID theory *The SQUD Handbook* vol 1 *Fundamentals and Technology of SQUIDs and SQUID Systems* ed J Clarke and A I Braginski (Weinheim: Wiley–VCH) chapter 2, pp 29–92

[35] Ketchen M, Awschalom D, Gallagher W, Kleinsasser A, Sandstrom R, Rozen J and Bumble B 1989 Design, fabrication, and performance of integrated miniature SQUID susceptometers *IEEE Trans. Magn.* **25** 1212–5

[36] Bushev P *et al* 2010 Trapped electron coupled to superconducting devices arXiv:1009.3425v1 [cond-mat.supr-con]

Publication 2

Superconducting quantum interference devices with submicron Nb/HfTi/Nb junctions for investigation of small magnetic particles

J. Nagel,[1] O. F. Kieler,[2] T. Weimann,[2] R. Wölbing,[1] J. Kohlmann,[2] A. B. Zorin,[2] R. Kleiner,[1] D. Koelle,[1] and M. Kemmler[1,a)]

[1]*Physikalisches Institut–Experimentalphysik II and Center for Collective Quantum Phenomena in LISA$^+$, Universität Tübingen, Auf der Morgenstelle 14, D-72076 Tübingen, Germany*

[2]*Fachbereich 2.4 "Quantenelektronik," Physikalisch-Technische Bundesanstalt, Bundesallee 100, 38116 Braunschweig, Germany*

(Received 9 June 2011; accepted 28 June 2011; published online 21 July 2011)

We investigated, at temperature 4.2 K, electric transport, flux noise, and resulting spin sensitivity of miniaturized Nb direct current superconducting quantum interference devices (SQUIDs) based on submicron Josephson junctions with HfTi barriers. The SQUIDs are either of the magnetometer-type or gradiometric in layout. In the white noise regime, for the best magnetometer we obtain a flux noise $S_\Phi^{1/2} = 250\,\mathrm{n}\Phi_0/\mathrm{Hz}^{1/2}$, corresponding to a spin sensitivity $S_\mu^{1/2} \geq 29\,\mu_B/\mathrm{Hz}^{1/2}$. For the gradiometer we find $S_\Phi^{1/2} = 300\,\mathrm{n}\Phi_0/\mathrm{Hz}^{1/2}$ and $S_\mu^{1/2} \geq 44\,\mu_B/\mathrm{Hz}^{1/2}$. The devices can still be optimized with respect to flux noise and coupling between a magnetic particle and the SQUID, leaving room for further improvement towards single spin resolution. © *2011 American Institute of Physics*. [doi:10.1063/1.3614437]

Growing interest in the investigation of small spin systems like molecular magnets,[1–3] single electrons,[4] or cold atom clouds[5] demands for proper detection schemes. Compared to, e.g., magnetic resonance force microscopy[6] or magneto-optic spin detection,[7,8] superconducting quantum interference devices (SQUIDs) offer the advantage of direct measurement of changes of the magnetization in small spin systems.[1,9] High spin sensitivity requires SQUIDs with low flux noise and strong magnetic coupling between particle(s) and SQUID loop. These needs can be met by nano-scaling the devices,[10–12] e.g., by focused ion beam milling,[13,14] electron-beam lithography,[15] atomic force microscopy anodization,[16,17] shadow evaporation[18] or by coupling small pickup loops to larger SQUIDs.[19] While nanopatterning of the SQUID loop yields no basic technical difficulties, the creation of overdamped Josephson junctions (JJs), as required for direct current (dc) SQUIDs, with submicron dimensions is more challenging.

A widely used approach is to use constriction JJs. In some cases this yielded dc SQUIDs[14,15] with root mean square (rms) flux noise $S_\Phi^{1/2}$ down to 0.2 $\mu\Phi_0/\mathrm{Hz}^{1/2}$ (Φ_0 is the magnetic flux quantum), which, however, are suitable only for operation in a limited range of temperature T. Even smaller $S_\Phi^{1/2} = 17\,\mathrm{n}\Phi_0/\mathrm{Hz}^{1/2}$ has been reported for larger SQUIDs based on superconductor-insulator-superconductor (SIS) tunnel JJs with external resistive shunts.[20] In this Letter, we report on the realization of small and sensitive dc SQUIDs based on superconductor-normal conductor-superconductor (SNS) sandwich-type JJs, without resistive shunts, which simplifies SQUID miniaturization.

Our JJs are based on a Nb/HfTi/Nb trilayer process,[21] which was developed for the fabrication of submicron SNS junctions.[22] All JJs are square shaped with lateral dimensions $200 \times 200\ \mathrm{nm}^2$. The JJs with barrier thickness $d_{\mathrm{HfTi}} = 24$ nm have a critical current density $j_c \approx 200$–$300\ \mathrm{kA/cm}^2$ at $T = 4.2$ K and a resistance times junction area $\rho_n \approx 14$–$19\ \mathrm{m}\Omega\mu\mathrm{m}^2$, leading to a characteristic voltage $V_c = j_c\rho_n \approx 40\ \mu$V. The three SQUIDs presented in this paper have different layouts. *G1* [see Fig. 1(a)] has a gradiometric design. The gradiometer line in the top Nb layer carries the bias current I (flowing through the junctions to the bottom Nb layer) and in addition allows for the (on-chip) application of magnetic flux Φ to the gradiometer (referred to one loop) via a current I_{mod} without the need of external coils. *M1* [see Fig. 1(b)] is of the magnetometer-type. *M2* [see inset of Fig. 1(b)], which is similar to *M1*, has a washer, allowing flux modulation with relatively small external magnetic fields ($B/\Phi = 0.5\ \mathrm{mT}/\Phi_0$).

All measurements were performed at $T = 4.2$ K in a high-frequency shielding chamber with the sample mounted inside a magnetic shield. All currents were applied by battery powered low-noise current sources. For the noise measurements we used a commercial Nb dc SQUID amplifier surrounded by a superconducting Nb shield.[23] The SQUID is connected in parallel to the input coil of the SQUID amplifier, with an input resistor R_{in} connected in series with the coil. A separate

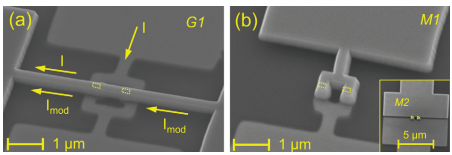

FIG. 1. (Color online) Scanning electron microscopy (SEM) images of the SQUIDs. The JJs with size $200 \times 200\ \mathrm{nm}^2$ are indicated as dotted lines in the top Nb layer. (a) Gradiometer *G1* with line width 250 nm and outer loop size $1.5 \times 1.5\ \mu\mathrm{m}^2$; arrows indicate scheme of current flow. (b) Magnetometer *M1* with line width 250 nm and SQUID hole $500 \times 500\ \mathrm{nm}^2$. Inset: washer-type magnetometer *M2* with washer area $10 \times 10\ \mu\mathrm{m}^2$ and SQUID hole $500 \times 500\ \mathrm{nm}^2$.

a)Electronic mail: matthias.kemmler@uni-tuebingen.de.

feedback (and modulation) coil of the SQUID amplifier allows for a flux locked loop operation of the SQUID amplifier with a sensitivity $S_{V,\mathrm{amp}}^{1/2} \approx 40\ \mathrm{pV/Hz^{1/2}}$ for $R_{\mathrm{in}} = 3.3\ \Omega$ at $T = 4.2$ K. The typical bandwidth of the amplifier is of the order of few tens of kHz. To determine the rms flux noise of our SQUIDs we measured the voltage noise at the output of the amplifier. After subtracting the noise contribution from the amplifier, we obtain the spectral density of voltage noise $S_{V,\mathrm{SQUID}}$ for the SQUID and calculate the corresponding rms flux noise $S_\Phi^{1/2} = S_{V,\mathrm{SQUID}}^{1/2}/|\partial V/\partial\Phi|$. Here, V is the voltage across the SQUID and $\partial V/\partial\Phi$ is the transfer coefficient.

Figure 2(a) shows the current voltage characteristic (IVC) of *G1* measured at $I_{\mathrm{mod}} = 0$. The IVC is resistively shunted junction (RSJ)-like, with a critical current $I_c = 178$ μA and resistance $R = 233$ mΩ, yielding $V_c = 41.5$ μV. The inset of Fig. 2(a) shows $I_c(I_{\mathrm{mod}})$ together with a simulated curve based on the RSJ model (including thermal noise and inductance asymmetry), which yields $\beta_L \equiv 2I_0L/\Phi_0 = 0.18$. Here, I_0 is the average maximum critical current of the two JJs and L is the inductance of the gradiometric SQUID, i.e., half the inductance of one loop of the gradiometer. With $2I_0 = 178$ μA we obtain $L = 2.1$ *p*H. From the measured period of $I_c(I_{\mathrm{mod}})$ we obtain $\Phi/I_{\mathrm{mod}} = 227$ mΦ_0/mA. The small but finite shift $\Delta I_{\mathrm{mod}} = 95$ μA of the maxima in $I_c(I_{\mathrm{mod}})$ for opposite polarity can be solely attributed to an inductance asymmetry due to the asymmetric current bias, i.e., the asymmetry in the critical currents of the JJs is negligibly small. Figure 2(b) shows $V(I_{\mathrm{mod}})$ for different values of I. For $I \approx 185$ μA we obtain a maximum transfer coefficient $V_\Phi \approx 100$ μV/Φ_0. The inset of Fig. 2(c) shows $V(I_{\mathrm{mod}})$ and $S_{\Phi,\mathrm{w}}^{1/2}(I_{\mathrm{mod}})$ in the white noise regime (determined by averaging the spectra from $f = 2$ to 3 kHz) for $I = 185$ μA. This yields minima in $S_{\Phi,\mathrm{w}}^{1/2}(I_{\mathrm{mod}})$ at the optimum flux bias point (indicated by the dashed line), for which the main graph of Fig. 2(c) shows $S_\Phi^{1/2}$ vs frequency f. For low frequencies $f \leq 10$ Hz we find $S_\Phi(f) \propto 1/f^2$, which can be attributed to a single fluctuator (flux or I_c) producing random telegraph noise in the time trace $V(t)$. For higher frequencies $10\ \mathrm{Hz} \leq f \leq 1$ kHz the frequency dependence is more $1/f$ like, which might be caused by an admixture of noise from a few additional fluctuators with higher characteristic frequencies. The peak in $S_\Phi(f)$ near $f = 12$ Hz presumably results from mechanical vibrations. The spectrum in the white noise limit above 1 kHz yields $S_{\Phi,\mathrm{w}}^{1/2} \approx 300\ \mathrm{n\Phi_0/Hz^{1/2}}$, with a cutoff at $f \approx 2 \times 10^4$ Hz due to the SQUID amplifier electronics. The magnetometer-type devices *M1* and *M2* had similar characteristics, with $S_{\Phi,\mathrm{w}}^{1/2} \approx 250\ \mathrm{n\Phi_0/Hz^{1/2}}$ and $\approx 270\ \mathrm{n\Phi_0/Hz^{1/2}}$, respectively.

Finally, we turn to the spin sensitivity $S_\mu^{1/2} = S_\Phi^{1/2}/\phi_\mu$ of our devices which, besides the flux noise, depends on the coupling factor ϕ_μ, i.e., the amount of flux coupled into the SQUID by a magnetic particle is divided by the modulus $|\vec{\mu}|$

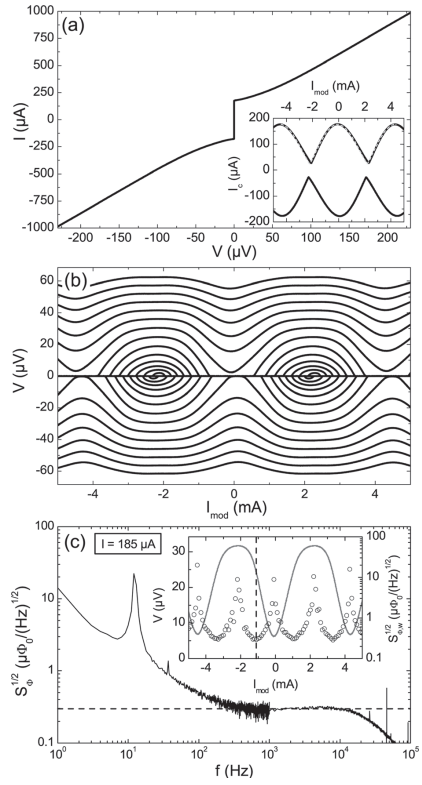

FIG. 2. Transport and noise characteristics of *G1* at $T = 4.2$ *K*: (a) IVC at $I_{\mathrm{mod}} = 0$; inset shows measured $I_c(I_{\mathrm{mod}})$ (solid line) and simulated curve (dashed line). (b) $V(I_{\mathrm{mod}})$ for $I = -297 \ldots 300$ μA (in 20.1 μA steps). (c) Spectral density of rms flux noise $S_\Phi^{1/2}(f)$ at optimal working point (cf., dashed line in inset); dashed line indicates 300 nΦ_0/Hz$^{1/2}$. Inset: $V(I_{\mathrm{mod}})$ (solid line) and $S_{\Phi,\mathrm{w}}^{1/2}(I_{\mathrm{mod}})$ (open circles; averaged from $f = 2$–3 kHz).

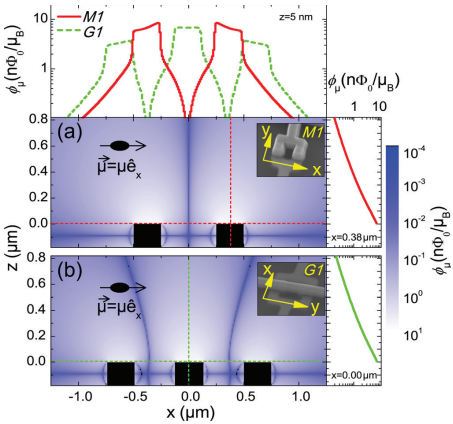

FIG. 3. (Color online) Calculated coupling factor ϕ_μ vs particle position. Main graphs: contour plots $\phi_\mu(x,z)$ for (a) magnetometer *M1* and (b) gradiometer *G1*; Nb structures are indicated by black rectangles. Insets: SEM images of the SQUIDs. Dashed lines indicate position of linescans $\phi_\mu(x)$ [above (a)] and $\phi_\mu(z)$ [to the right of (a) and (b)].

of its magnetic moment. Taking into account the SQUID geometry, Fig. 3 shows the calculated coupling factor of *M1* and *G1* vs. the position $\vec{r}$ of a point-like magnetic particle with its magnetic moment $\vec{\mu}$ pointing in-plane of the SQUID loop. A detailed description of the calculation procedure for non-gradiometric SQUIDs can be found in Ref. 12. For the gradiometric SQUID *G1* one has to consider the magnetic field distribution $\vec{B}(\vec{r})$ created by two circular currents $I_{1,2} = \pm I_B$ in each loop. In this case the coupling factor ϕ_μ is given by $\vec{B}(\vec{r})/2I_B$. For an in-plane magnetization of the particle, layout *M1* provides the highest coupling factor if the particle is placed directly on top of the SQUID loop. For *G1* the optimum coupling can be achieved if the particle is placed on the center conductor line. At this position the particle couples flux of opposite sign into both loops of the gradiometric SQUID, which leads to an approximately twice as large coupling factor as compared to placing the particle on the outer conductors. For a particle with 10 nm diameter, placed directly on top of the SQUID, we take a vertical distance $z = 5$ nm from the SQUID surface, which yields $\phi_\mu = 8.5\ \mathrm{n}\Phi_0/\mu_B$ (μ_B is the Bohr magneton) for *M1* and 6.8 $\mathrm{n}\Phi_0/\mu_B$ for *G1* at the center conductor. With $S_\Phi^{1/2} \approx 250\,\mathrm{n}\Phi_0/\mathrm{Hz}^{1/2}$ we calculate the spin sensitivity of *M1* to $S_\mu^{1/2} = 29\,\mu_B/\mathrm{Hz}^{1/2}$. For the gradiometric SQUID we calculate $S_\mu^{1/2} = 44\,\mu_B/\mathrm{Hz}^{1/2}$.

In conclusion, we have shown that miniaturized dc SQUIDs based on sandwich-type overdamped SNS Josephson junctions have a compact design and can be operated with very promising values of flux noise and spin sensitivity. Although our devices are not optimized, flux noise values down to 250 $\mathrm{n}\Phi_0/\mathrm{Hz}^{1/2}$ have been achieved, yielding an estimated spin sensitivity as low as 29 $\mu_B/\mathrm{Hz}^{1/2}$. Further improvements are feasible; e.g., placing the two SQUID arms on top of each other[20] reduces the SQUID inductance and hence the flux noise. Furthermore, the coupling can be improved by patterning an additional constriction within the SQUID loop.

This work was supported by the Nachwuchswissenschaftlerprogramm of the Universität Tübingen, by the Deutsche Forschungsgemeinschaft (DFG) via the SFB TRR21 and by the European Research Council via SOCATHES. J. Nagel and M. Kemmler gratefully acknowledge support by the Carl-Zeiss Stiftung.

[1]W. Wernsdorfer, Adv. Chem. Phys. **118**, 99 (2001).
[2]D. Gatteschi and R. Sessoli, Angew. Chem., Int. Ed. **42**, 268 (2003).
[3]L. Bogani and W. Wernsdorfer, Nat. Mater. **7**, 179 (2008).
[4]P. Bushev, D. Bothner, J. Nagel, M. Kemmler, K. B. Konovalenko, A. Loerincz, K. Ilin, M. Siegel, D. Koelle, R. Kleiner, and F. Schmidt-Kaler, Eur. Phys. J. D **63**, 9 (2011).
[5]J. Fortágh and C. Zimmermann, Science **307**, 860 (2005).
[6]D. Rugar, R. Budakian, H. J. Mamin, and B. W. Chui, Nature **430**, 329 (2004).
[7]J. R. Maze, P. L. Stanwix, J. S. Hodges, S. Hong, J. M. Taylor, P. Cappellaro, L. Jiang, M. V. G. Dutt, E. Togan, A. S. Zibrov, A. Yacoby, R. L. Walsworth, and M. D. Lukin, Nature **455**, 644 (2008).
[8]G. Balasubramanian, I. Y. Chan, R. Kolesov, M. Al-Hmoud, J. Tisler, C. Shin, C. Kim, A. Wojcik, P. R. Hemmer, A. Krueger, T. Hanke, A. Leitenstorfer, R. Bratschitsch, F. Jelezko, and J. Wrachtrup, Nature **455**, 648 (2008).
[9]J. Gallop, Supercond. Sci. Technol. **16**, 1575 (2003).
[10]C. P. Foley and H. Hilgenkamp, Supercond. Sci. Technol. **22**, 064001 (2009).
[11]V. Bouchiat, Supercond. Sci. Technol. **22**, 064002 (2009).
[12]J. Nagel, K. B. Konovalenko, M. Kemmler, M. Turad, R. Werner, E. Kleisz, S. Menzel, R. Klingeler, B. Büchner, R. Kleiner, and D. Koelle, Supercond. Sci. Technol. **24**, 015015 (2011).
[13]A. G. P. Troeman, H. Derking, B. Borger, J. Pleikies, D. Veldhuis, and H. Hilgenkamp, Nano Lett. **7**, 2152 (2007).
[14]L. Hao, J. C. Macfarlane, J. C. Gallop, D. Cox, J. Beyer, D. Drung, and T. Schurig, Appl. Phys. Lett. **92**, 192507 (2008).
[15]R. F. Voss, R. B. Laibowitz, and A. N. Broers, Appl. Phys. Lett. **37**, 656 (1980).
[16]V. Bouchiat, M. Faucher, C. Thirion, W. Wernsdorfer, T. Fournier, and B. Pannetier, Appl. Phys. Lett. **79**, 123 (2001).
[17]M. Faucher, P.-O. Jubert, O. Fruchart, W. Wernsdorfer, and V. Bouchiat, Supercond. Sci. Technol. **22**, 064010 (2009).
[18]A. Finkler, Y. Segev, Y. Myasoedov, M. L. Rappaport, L. Neeman, D. Vasyukov, E. Zeldov, M. E. Huber, J. Martin, and A. Yacoby, Nano Lett. **10**, 1046 (2010).
[19]N. C. Koshnick, M. E. Huber, J. A. Bert, C. W. Hicks, J. Large, H. Edwards, and K. A. Moler, Appl. Phys. Lett. **93**, 243101 (2008).
[20]D. J. Van Harlingen, R. H. Koch, and J. Clarke, Appl. Phys. Lett. **41**, 197 (1982).
[21]D. Hagedorn, R. Dolata, F.-I. Buchholz, and J. Niemeyer, Physica C **372–376**, 7 (2002).
[22]D. Hagedorn, O. Kieler, R. Dolata, R. Behr, F. Müller, J. Kohlmann, and J. Niemeyer, Supercond. Sci. Technol. **19**, 294 (2006).
[23]*SQ100 LTS dc SQUID, PC-100 Single-Channel dc SQUID Electronics System, STAR Cryoelectronics*, USA.

Publication 3

Direct current superconducting quantum interferometers with asymmetric shunt resistors

M. Rudolph,[1] J. Nagel,[1] J. M. Meckbach,[2] M. Kemmler,[1] M. Siegel,[2] K. Ilin,[2] D. Koelle,[1] and R. Kleiner[1,a)]

[1]*Physikalisches Institut—Experimentalphysik II and Center for Collective Quantum Phenomena in LISA$^+$, Universität Tübingen, Auf der Morgenstelle 14, D-72076 Tübingen, Germany*

[2]*Institut für Mikro- und Nanoelektronische Systeme, Karlsruhe Institute of Technology, Hertzstr. 16, D-76187 Karlsruhe, Germany*

(Received 26 June 2012; accepted 16 July 2012; published online 30 July 2012)

We have investigated asymmetrically shunted Nb/Al-AlO$_x$/Nb direct current (dc) superconducting quantum interference devices (SQUIDs). While keeping the total resistance R identical to a comparable symmetric SQUID with $R^{-1} = R_1^{-1} + R_2^{-1}$, we shunted only one of the two Josephson junctions with $R = R_{1,2}/2$. Simulations predict that the optimum energy resolution ϵ and thus also the noise performance of such an asymmetric SQUID can be 3–4 times better than that of its symmetric counterpart. Experiments at a temperature of 4.2 K yielded $\epsilon \approx 32\,\hbar$ for an asymmetric SQUID with an inductance of 22 pH. For a comparable symmetric device, $\epsilon = 110\,\hbar$ was achieved, confirming our simulation results. © *2012 American Institute of Physics*. [http://dx.doi.org/10.1063/1.4739850]

The transport characteristics and noise performance of direct current (dc) superconducting quantum interference devices superconducting quantum interference devices (SQUIDs) having symmetric Josephson junctions have been intensively studied from the 1970s. Numerical simulations of the Langevin equations describing the SQUID dynamics reliably helped to understand the modulation patterns $V(\Phi_a, I)$ and the low-frequency voltage noise power $S_V(\Phi_a, I)$, where V is the dc voltage across the SQUID, I is the bias current, and Φ_a is the applied flux. With the flux-to-voltage transfer function $V_\Phi = |dV/d\Phi_a|$, one obtains the flux noise power $S_\Phi = S_V/V_\Phi^2$ or energy resolution $\epsilon = S_\Phi/2L$, where L is the SQUID inductance. For an optimized device, one obtains in the limit of small thermal fluctuations an energy resolution $\epsilon = (8-9)k_BTL/R$ for an inductance parameter $\beta_L = 2I_0L/\Phi_0$ somewhat below 1.[1,2] Here, I_0 and R, respectively, denote the junction critical current and resistance. Φ_0 is the flux quantum. Although ϵ can be very low—for example, in Ref. 3 a value of $\sim 3\hbar$ has been reported at 4.2 K for a 2 pH device—one may ask whether or not it still can be improved by introducing asymmetries in the junction parameters or perhaps by adding new elements to the SQUID. Early simulations have shown that asymmetries in the junction critical currents and resistances can enhance V_Φ, although for the prize of asymmetric $V(\Phi_a)$ patterns.[1] It has also been predicted that an additional damping resistor can enhance V_Φ.[4,5] Several works addressed junction asymmetries and additional damping resistors in more detail,[6–11] with the result that the transfer function can be increased and flux noise be decreased. The above investigations, however, explored only a very limited range of parameters and often addressed devices where the symmetric counterpart was far from optimum.

Let us start with a theoretical analysis, using the standard Langevin equations[1] where the Josephson junctions are described by the resistively and capacitively shunted junction model.[12,13] With $i = I/I_0$ the normalized currents through the junctions $k = 1, 2$ are given by

$$\frac{i}{2} \pm j = \beta_c(1 \pm \alpha_c)\ddot{\delta}_k + (1 \pm \alpha_r)\dot{\delta}_k + (1 \pm \alpha_i)\sin(\delta_k) + i_{N,k}, \quad (1)$$

where α_c, α_r, and α_i denote the asymmetries in capacitance, resistance, and critical current, respectively. The junction critical currents are $I_{0,k} = I_0(1 \pm \alpha_i)$, their resistances $R/(1 \pm \alpha_r)$ and their capacitances $C_k = C(1 \pm \alpha_c)$. "$\pm$" refers to junctions 1 and 2, respectively. δ_k denotes the phase of junction k, $j = J/I_0$ is the normalized circulating current in the SQUID loop and $\beta_c = 2\pi I_0R^2C/\Phi_0$ is the Stewart-McCumber parameter. Dots denote derivative with respect to normalized time $\tau = \Phi_0/2\pi I_0R$. The normalized noise current $i_{N,k}$ has a spectral power density 4Γ, with $\Gamma = 2\pi k_BT/I_0\Phi_0$. The δ_k are related by

$$\delta_2 - \delta_1 = 2\pi\Phi/\Phi_0 + \pi\beta_L\left(j + \frac{\alpha_L}{2}i\right), \quad (2)$$

where Φ is the total flux through the SQUID. $L = L_1 + L_2$, where L_1 and L_2 are the inductances of the two SQUID arms, related to the inductance asymmetry α_L via $L_k = L(1 \pm \alpha_L)/2$.

From Eqs. (1) and (2), one obtains the normalized dc voltage $v = V/I_0R$, and thus the current voltage characteristic (IVC) by taking the time average of $u = (\dot{\delta}_1 + \dot{\delta}_2)/2$. From a Fourier transform of u, one obtains the normalized correlation functions $s_v = S_V 2\pi I_0R/\Phi_0^3$, $s_\phi = S_\Phi I_0R/(2\Phi_0k_BT)$, and $e = s_\phi/2\Gamma\beta_L$.

The quantity we are interested in most is the optimized normalized energy resolution e_{opt}, where optimization is done for some or even all SQUID parameters. Recently, we have performed a systematic optimization of the noise performance of the rf SQUID, optimizing all of its parameters.[14,15] We now apply the same procedure to fully optimize e of the dc SQUID, with respect to $i, \phi_a = \Phi_a/\Phi_0, \beta_L$,

a)Electronic mail: kleiner@uni-tuebingen.de.

$\beta_c, \alpha_i, \alpha_c$, and α_r, i.e., for a given value of one or some of these parameters we find all others so that $e_{\rm opt}$ is minimized. The inductance asymmetry α_L does not appear in the above list, since, for a given bias current, it only causes a phase shift in $v(\phi_a)$ and also the noise correlation functions. Since in practice the junction capacitance is always nonzero, the McCumber parameter β_c should be as large as possible to obtain large values of I_0R. It turns out that β_c values below 0.8 are uncritical in the sense that the other parameters can be tuned so that $e_{\rm opt}$ attains its minimum value irrespective of β_c.

Fig. 1(a) shows $e_{\rm opt}$ vs. α_r for $\alpha_i = \alpha_c = 0$ (full circles) and for variable $\alpha_i = \alpha_c$ (open circles). Fixed parameters are $\beta_c = 0.7$ and $\Gamma = 0.01$. The parameters i, ϕ_a, and β_L have been varied to minimize e. We have used $\alpha_i = \alpha_c$, having in mind junctions where both I_0 and C scale with the junction area and R can be chosen independently by shunting. The value for Γ was chosen as typical for operation at 4.2 K. For $\alpha_i = 0$, $e_{\rm opt}$ vs. α_r decreases from ~ 1.6 to 0.7 for $\alpha_r \to 1$. In case of variable α_i the minimum $e_{\rm opt}$ is about 0.4, i.e., a factor of 4 lower than the energy resolution of a comparable symmetric SQUID. Note that each point in the graph corresponds to different values of i, ϕ_a, β_L. We do not list the value of these parameters explicitly but note that in all cases β_L was in the range 0.4–0.5. $\alpha_i = \alpha_c \approx 0.3-0.5$ was found in case these parameters were varied.

In Fig. 1(b), we show $e_{\rm opt}$ vs. $\alpha_i = \alpha_c$ for variable β_L and fixed $\beta_c = 0.7$ and $\Gamma = 0.01$ and $\alpha_r = 0.99$. The lowest values of $e_{\rm opt}$ are achieved for α_i near 0.5. For lower values of α_i, $e_{\rm opt}$ monotonically increases. In particular, $e_{\rm opt}$ is achieved when α_i and α_r have the same sign, i.e., the junction having the *lower* resistance should have the *higher* I_0. We have obtained similar results, giving almost the same lowest values for $e_{\rm opt}$, also for higher values of Γ (up to 0.1). $e_{\rm opt}$ is thus a robust quantity.

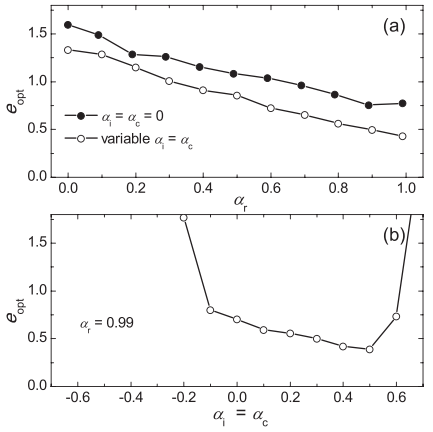

FIG. 1. Optimized normalized energy resolution $e_{\rm opt}$ vs. (a) resistance asymmetry α_r and (b) junction critical current and capacitance asymmetry $\alpha_i = \alpha_c$. Fixed parameters are $\Gamma = 0.01$ and $\beta_c = 0.7$. For all data points, β_L has been varied.

In dimensioned units $\epsilon = e \cdot 2\Phi_0 k_B T / I_0 R$. To maximize I_0 for $\beta_L \approx 0.5$, L should be as small as possible. Then, to maximize R and keep β_c below 1, C should be as small as possible, which for a given capacitance per area means to keep the junction area as small. If junction asymmetries are considered, given a constant critical current density, the size of the weaker junction is presumably limited by the fabrication process and, to obtain an α_i of, e.g., 0.3, the average junction area is increased by about 40% from its minimum value. This basically compensates the gain in $e_{\rm opt}$. Asymmetries in α_i are thus not necessarily helpful. Thus, below we discuss an experimental design having $\alpha_i = \alpha_c = 0$.

We also note that for α_r very close to 1, $e_{\rm opt}$ increases slightly again with increasing α_r for $\alpha_i = \alpha_c = 0$. This is related to chaotic dynamics which appears in some ranges of i and ϕ_a. Below, we will address this issue in comparison to experimental data. Nonetheless, if small values of $e_{\rm opt}$ can be retained for $\alpha_r \to 1$, the easiest way to realize the corresponding SQUID experimentally is to "move" the shunt from junction 1 to junction 2, leaving junction 1 unshunted and junction 2 shunted with a resistance $R/2$. In the following, we discuss the performance of such a Nb/Al-AlO$_x$/Nb SQUID and compare it to simulations, as well as to the performance of a corresponding symmetric SQUID.

Figs. 2(a) and 2(b) show optical images of an asymmetric and a symmetric SQUID. The SQUIDs have been fabricated using a Nb/Al-AlO$_x$/Nb technology based on optical photolithography. By a combination of reactive ion etching (RIE) employing CF_4 and O_2 and ion beam etching (IBE), the ground-electrode was defined. The subsequent definition of the junction area was done by RIE and anodic oxidation in an aqueous solution of $(NH_4)B_5O_8$ and $C_2H_6O_2$. Before the definition of the vias (RIE-IBE), the connecting bridges for the anodization between the individual SQUIDs were removed. The following definitions of the resistor, insulation layer, and wiring layer were all done using a lift-off technique. For the resistor material, a 76 nm thick Palladium layer was deposited, resulting in a sheet resistance of 1 Ω/sq

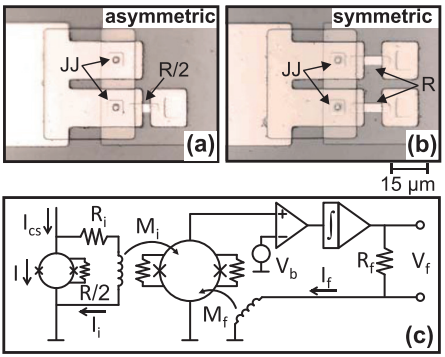

FIG. 2. Optical image of the (a) asymmetric and (b) symmetric SQUID. The Josephson junctions are labeled by "JJ" and the shunt resistors by R and R/2. (c) Readout scheme of the asymmetric SQUID using a SQUID amplifier operated in flux-locked loop.

at $T = 4.2$ K. The ~300 nm thick SiO insulation layer was deposited using thermal evaporation, while the samples were mounted on a water cooled copper plate ($T_{\text{process}} \leq 26\,^{\circ}\text{C}$). After *in-situ* pre-cleaning, the final Nb wiring layer connecting the junctions, vias, and shunt-resistors was dc-magnetron sputtered at room temperature.

Transport and noise measurements were performed at $T = 4.2$ K in a magnetically and electrically shielded environment. Dc characteristics (IVC, $V(\Phi_a)$, critical current $I_c(\Phi_a)$) were measured in a standard four-point configuration, using low noise current sources and a high impedance room temperature voltage amplifier (RTA). For the noise measurements, the RTA was not sensitive enough. Thus, V was preamplified with a commercial SQUID amplifier[16] having a $60\,\text{pV}/\text{Hz}^{1/2}$ resolution, operated in a flux-locked loop with ac flux bias at modulation frequency $f_{\text{mod}} = 256$ kHz. The SQUIDs were operated open loop at fixed I and Φ_a. V was measured by connecting the input coil of the SQUID amplifier in parallel to the SQUID. A 5 Ω resistor R_i was in series to the input coil, as shown in Fig. 2(c). Due to the low input impedance of the amplifier, the current I_{cs} from the current source divides into I and the current I_{i} through the input coil. At given I_{cs}, I varies when changing Φ_a, affecting V_Φ and thus the determination of the energy resolution. Using Kirchhoff's laws and the condition for flux-locked loop operation, $I_i \text{M}_\text{i} = I_f \text{M}_\text{f}$, with M_i (M_f) being the mutual inductance between the amplifier SQUID and the input (feedback) coil, one obtains $I_i = (\text{M}_\text{f}/\text{M}_\text{i})(V_f/R_f)$. Since M_i, M_f, and R_f are constants, I_i can be determined by measuring V_f. To determine $V(\Phi_a)$ for constant I, a software control-loop was implemented adjusting I_{cs} such that, for each value of Φ_a, $I = I_{\text{cs}} - I_i$ was fixed. The ratio $(\text{M}_\text{f}/\text{M}_\text{i})$ slightly differed for different samples and was adjusted for each device until the bias corrected $V(\Phi_a)$ curve measured with the SQUID amplifier fitted the corresponding $V(\Phi_a)$ curve measured with the RTA; all other measurements for a given device were then performed with fixed $(\text{M}_\text{f}/\text{M}_\text{i})$.

Fig. 3(a) shows IVCs of the asymmetric SQUID. Solid black line is for $\Phi_a = 0$, solid gray line for $\Phi_a = 0.5\,\Phi_0$. The critical current is $I_c \approx 2I_0 = I_{01} + I_{02} = 62.0\,\mu$A and for $R/2$ we obtain $0.57\,\Omega$, yielding $I_cR = 35.3\,\mu$V. One notes that, in contrast to IVCs of symmetric devices, the IVC of the asymmetric SQUID exhibits several structures, including regions of negative differential resistance. These structures are reproduced in simulations, cf. dashed lines. The negative differential resistance in fact separates a high-current regime having chaotic dynamics from a more stable low-current regime. For the simulation, we have used parameters $\beta_L = 0.675$, $\beta_c = 0.27$, $\Gamma = 0.0065$, $\alpha_r = 0.999$, $\alpha_i = \alpha_c = 0$. These parameters have been inferred partly by fitting the IVC but also by fitting $I_c(\Phi_a)$. The corresponding data for $I_c(\Phi_a)$ are shown by solid black lines in the lower right inset of Fig. 3(a). The dashed line in this graph shows the calculated curve. Finally, from β_L and I_0, we obtain $L = 21.7$ pH, which is close to the design value of 23.9 pH. The upper left inset of Fig. 3(a) shows by solid black line the IVC taken at $\Phi_a = 0.843\,\Phi_0$. For this particular flux value, the best energy resolution was found at the voltage indicated by the arrow. The dashed line is a calculated curve, using the parameters given above. A family of curves $V(\Phi_a)$ for variable I is shown in Fig. 3(b). Experimental data for different I are shown by solid black lines. The corresponding calculated curves, shown by dashed lines, fit the data reasonably well, showing that the dc characteristics of our device can be understood by the SQUID Langevin equations. In the $V(\Phi_a)$ curves, one notes that the slope $\text{d}V/\text{d}\Phi_a$ is very steep for $\Phi_a \geq 0.5\,\Phi_0$, in fact reaching maximum values of about $1.2\,\text{mV}/\Phi_0$ near $I = 56\,\mu$A.

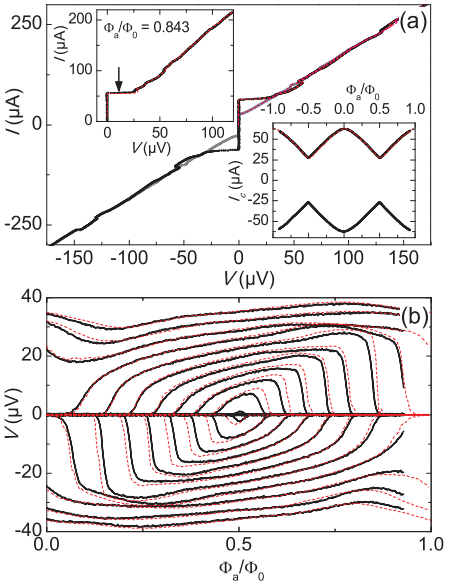

FIG. 3. Dc characteristics of the asymmetric SQUID: (a) IVCs at $\Phi_a = 0$ (solid black line) and at $\Phi_a = 0.5\,\Phi_0$ (solid gray line). Lower right inset: $I_c(\Phi_a)$. Upper left inset: IVC at $\Phi_a = 0.843\,\Phi_0$. The arrow indicates the voltage for the lowest energy resolution. Theoretical curves are shown by dashed lines. (b) $V(\Phi_a)$ (solid black line), for $I = -76.4\,\mu\text{A} - 75.9\,\mu\text{A}$ (in $4.9\,\mu$A steps). Corresponding theoretical curves are shown by dashed lines.

Our central results are shown in Fig. 4. Figure 4(a) shows $V(\Phi_a)$ for the optimum bias current of $56\,\mu$A. Dots represent the experimental data, as taken by the SQUID amplifier. For comparison, the solid black line represents the corresponding data taken by the RTA. The two curves are well on top of each other, justifying our method of correcting the bias current in measurements using the SQUID amplifier. The line with symbols is the theoretical curve obtained from numerical simulations, which agrees well with the experimental curves. Figures 4(b) and 4(c), respectively, show by dots the experimental V_Φ and the white voltage noise $S_V^{1/2}$, and in comparison the corresponding calculated curves (lines plus symbols). For experimental data, $S_V^{1/2}$ has been averaged between $100\,\text{Hz} \leq f \leq 3\,\text{kHz}$. The voltage noise of the SQUID amplifier has been subtracted. Figure 4(d) displays ϵ and e, calculated from the graphs shown in (b) and (c). For this device, the optimum energy resolution is $32\hbar$; in normalized units, $e_{\text{opt}} = 0.52$. While Φ_a has to be carefully adjusted for minimum ϵ, the dependence on I was less critical. Similar

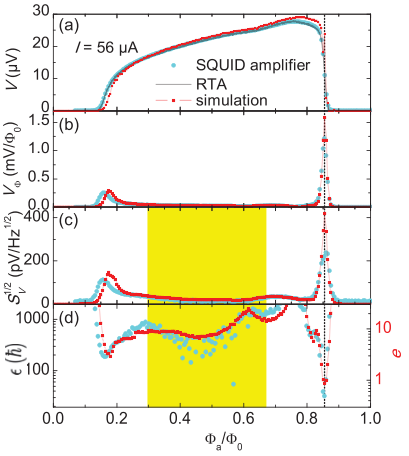

FIG. 4. Electric transport and noise vs. Φ_e for the asymmetric SQUID at optimum $I = 56\,\mu$A, measured with SQUID amplifier (dots) in comparison with numerical simulations (line plus symbol): (a) Voltage across the SQUID; solid black line shows corresponding curve measured with a high impedance room temperature amplifier. (b) Transfer function $V_\Phi = dV/d\Phi_e$. (c) Voltage noise $S_V^{1/2}$, experimental data averaged between 100 Hz $\leq f \leq$ 3 kHz (white noise regime). (d) Absolute (left) and normalized (right) energy resolution. In (c) and (d), the noise of the SQUID amplifier has been subtracted; within the shaded area the SQUID amplifier noise was above the noise of the asymmetric SQUID, resulting in large errors when calculating ϵ and e. The vertical dotted line indicates the position of minimum ϵ.

results with $e_{\rm opt} \leq 0.55$ were measured for $52\,\mu\text{A} \leq I \leq 56\,\mu$A. Surprisingly, the theoretical value for $e_{\rm opt} = 0.85$ is higher. The reason for this is an instability in the calculations, appearing as a chaotic switching between two nearby voltage states.[17] This seems to be absent in the experimental device. The minimum rms flux noise was $133\,n\Phi_0/\text{Hz}^{1/2}$ which is also quite low. For comparison, for the symmetric SQUID having parameters $I_0R = 37.07\,\mu$V, $\beta_L = 0.74$, $\beta_c = 0.18$, and $\Gamma = 0.00526$, we obtained $\epsilon_{\rm opt} = 110\,\hbar$ ($e_{\rm opt} = 1.79$) and $S_\Phi^{1/2} = 361\,n\Phi_0/\text{Hz}^{1/2}$, i.e., a factor of 3.4 higher $e_{\rm opt}$ than for our asymmetric device. Further note that for the asymmetric SQUID, β_c was only 0.27, allowing in principle to increase R by a factor of ~1.5, potentially decreasing ϵ to ~20$\hbar$.

In conclusion, we have shown that asymmetries in the junction parameters of a dc SQUID can help to significantly improve its noise performance over a SQUID with symmetric junctions. The most practical way to achieve this is to leave one junction unshunted, while the other junction is shunted by half of the resistance of the shunts of a symmetric device. Experimentally, we have found a factor of 3.4 improvement of the SQUID energy resolution over a symmetric device with comparable parameters. At least in simulations the drawback of the asymmetric shunt is to introduce chaotic behavior of the SQUID for certain regimes of bias current and applied flux. Our experimental device seems to be less sensitive to chaos. Thus, the asymmetrically shunted SQUID may be useful for applications where ultra-low values of energy resolutions are desired.

This work was supported by the European Research Council via ERC advanced grant SOCATHES, by the DFG via SFB/TRR 21 and in part by the DFG Centre of Functional Nanostructures Project No. B1.5. J. Nagel acknowledges support by the Carl-Zeiss-Stiftung.

[1]C. D. Tesche and J. Clarke, J. Low Temp. Phys. **29**, 301 (1977).
[2]J. J. P. Bruines, V. J. de Waal, and J. E. Mooij, J. Low Temp. Phys. **46**, 383 (1982).
[3]D. J. Van Harlingen, R. H. Koch, and J. Clarke, Appl. Phys. Lett. **41**, 197 (1982).
[4]K. Enpuku, K. Sueoka, K. Yoshida, and F. Irie, J. Appl. Phys. **57**, 1691 (1985).
[5]K. Enpuku, T. Muta, K. Yoshida, and F. Irie, J. Appl. Phys. **58**, 1916 (1985).
[6]R. Kleiner, D. Koelle, F. Ludwig, E. Dantsker, A. H. Miklich, and J. Clarke, J. Appl. Phys. **79**, 1129 (1996).
[7]J. Müller, S. Weiss, R. Gross, R. Kleiner, and D. Koelle, IEEE Trans. Appl. Supercond. **11**, 912 (2001).
[8]G. Testa, E. Sarnelli, S. Pagano, C. R. Calidonna, and M. M. Furnari, J. Appl. Phys. **89**, 5145 (2001).
[9]G. Testa, S. Pagano, E. Sarnelli, C. R. Calidonna, and M. M. Furnari, Appl. Phys. Lett. **79**, 2943 (2001).
[10]G. Testa, C. Granata, C. DiRusso, S. Pagano, M. Russo, and E. Sarnelli, Appl. Phys. Lett. **79**, 3989 (2001).
[11]F. Kahlmann, W. E. Booij, M. G. Blamire, P. F. McBrien, N. H. Peng, C. Jeynes, E. J. Romans, C. M. Pegrum, and E. J. Tarte, IEEE Trans. Appl. Supercond. **11**, 916 (2001).
[12]W. C. Stewart, Appl. Phys. Lett. **12**, 277 (1968).
[13]D. E. McCumber, J. Appl. Phys. **39**, 3113 (1968).
[14]R. Kleiner, D. Koelle, and J. Clarke, J. Low Temp. Phys. **149**, 230 (2007).
[15]R. Kleiner, D. Koelle, and J. Clarke, J. Low Temp. Phys. **149**, 261 (2007).
[16]SQ100 LTS dc SQUID, PC-100 Single-Channel dc SQUID Electronics System, STAR Cryoelectronics, USA.
[17]I. Goldhirsch, Y. Imry, G. Wasserman, and E. Ben-Jacob, Phys. Rev. B **29**, 1218 (1984).

Publication 4

Nanoscale multifunctional sensor formed by a Ni nanotube and a scanning Nb nanoSQUID

J. Nagel,[1] A. Buchter,[2] F. Xue,[2] O. F. Kieler,[3] T. Weimann,[3] J. Kohlmann,[3] A. B. Zorin,[3]
D. Rüffer,[4] E. Russo-Averchi,[4] R. Huber,[5] P. Berberich,[5] A. Fontcuberta i Morral,[4]
D. Grundler,[5,6] R. Kleiner,[1] D. Koelle,[1] M. Poggio,[2] and M. Kemmler[1]

[1] *Physikalisches Institut and Center for Collective Quantum Phenomena in LISA$^+$, Universität Tübingen, Auf der Morgenstelle 14, D-72076 Tübingen, Germany*
[2] *Department of Physics, University of Basel, Klingelbergstrasse 82, CH-4056 Basel, Switzerland*
[3] *Fachbereich 2.4 "Quantenelektronik", Physikalisch-Technische Bundesanstalt, Bundesallee 100, 38116 Braunschweig, Germany*
[4] *Laboratoire des Matériaux Semiconducteurs, Institut des Matériaux, Ecole Polytechnique Fédérale de Lausanne, CH-1015 Lausanne, Switzerland*
[5] *Physik-Department E11, Technische Universität München, Garching, Germany*
[6] *STI, Faculté Sciences et Technique de l'Ingénieur, Ecole Polytechnique Fédérale de Lausanne, CH-1015 Lausanne, Switzerland*

We report on measurements using a multifunctional combination of a scanning Nb nanoSQUID and a Ni nanotube attached to an ultrasoft cantilever as a magnetic tip. Using the functionality of the Ni cantilever beam, we demonstrate imaging of an Abrikosov vortex trapped in the Nb structure. With the SQUID as a sensor for magnetic flux Φ induced by the Ni tip at position $\vec{r}$, we determine the magnetic coupling $\Phi(\vec{r})$ for a large section of the 3D half-space above the nanoSQUID. These results are in good agreement with numerical calculations based on London theory, which take into account the geometry of the nanoSQUID. Furthermore, we find that the nanoSQUID can be used as a highly sensitive detector of displacement of the Ni nanotube, with an estimated optimum displacement sensitivity $S_r^{1/2} = 110\,\mathrm{fm}/\sqrt{\mathrm{Hz}}$. This value can be further improved by reducing the linewidth of the nanoSQUID loop and by using a magnetic tip material with larger magnetization and more strongly confined geometry.

PACS numbers: 85.25.Dq, 74.78.Na, 68.37.Rt 75.75.+a

There is a growing interest in the investigation of small spin systems, such as molecular magnets,[1–3] single chain magnets,[4] single electrons,[5] or cold atom clouds.[6] Various detection schemes, e.g., magneto-optical spin detection,[7, 8] magnetic resonance force microscopy,[9] or scanning-tunneling-microscopy assisted electron spin resonance,[10, 11] have been developed in order to detect such systems. In contrast to these techniques, superconducting quantum interference devices (SQUIDs) offer the advantage of direct measurement of magnetic hysteresis curves of a small magnetic particle (SMP) with a large bandwidth.[12, 13] Hence, many efforts have focused on the optimization of SQUIDs for SMP detection. A direct current (dc) SQUID is a superconducting loop, intersected by two Josephson junctions, and works as a flux-to-voltage transducer, i.e., the magnetic flux Φ threading the loop is converted into a voltage V across the junctions, yielding a periodic $V(\Phi)$ characteristics with a period of one magnetic flux quantum $\Phi_0 = h/2e$.[14] Since the magnetic field distribution of a SMP is very close to that of a magnetic dipole, the figure of merit for such SQUIDs is the spin sensitivity $S_\mu = S_\Phi/\phi_\mu^2$, where S_Φ is the spectral density of flux noise power and $\phi_\mu \equiv \Phi/\mu$ is the coupling factor, i.e., the amount of magnetic flux coupled into the SQUID loop per magnetic moment $\mu \equiv |\vec{\mu}|$ of the SMP. Both, S_Φ and ϕ_μ can be optimized by scaling the SQUID down to nanometer dimensions.[15–18] Various fabrication techniques, e.g. electron-beam lithography,[19, 20] focused ion beam milling,[18, 21, 22] atomic force microscopy anodization,[23, 24] self-aligned shadow evaporation,[25] or a combination of electron-beam lithography with the use of carbon nanotube junctions,[26] have been used to realize nanoSQUIDs.

The experimental determination of S_Φ poses no basic difficulties and was performed for various nanoSQUIDs that were fabricated, in some cases yielding very low values for $S_\Phi^{1/2} \approx 0.2 - 0.3\,\mu\Phi_0/\sqrt{\mathrm{Hz}}$.[19, 20, 22]. In contrast, the determination of ϕ_μ is not straightforward, as it depends on the position $\vec{r}_p$ and orientation $\hat{e}_\mu$ of the magnetic moment of a SMP relative to the SQUID loop and on the geometry of the SQUID. Up to now, ϕ_μ has been determined only by numerical or analytical calculations, which often rely on strongly simplifying assumptions (e.g. on the SQUID geometry or position and orientation of the SMP), restricting the validity of such approaches.[16, 17, 27] Recently, we proposed a routine for calculating $\phi_\mu(\hat{e}_\mu, \vec{r}_p)$, for a point-like particle in the 3-dimensional (3D) space above the SQUID loop.[18, 20] This routine takes explicitly into account the geometry in the plane of the SQUID loop, and is based on the numerical simulation of the 2-dimensional (2D) sheet current density in the SQUID loop, using London theory.[28] Still, this approach neglects the finite size of a SMP and the full 3D geometry of a SQUID. Altogether, the determination of the spin sensitivity S_μ of nanoSQUIDs, as a figure of merit for SMP detection, requires the reliable determination of the coupling factor ϕ_μ. Hence,

the experimental determination of ϕ_μ could serve as an important step forward, in order to test the theoretical approaches described above.

Here, we present a multifunctional sensor system, consisting of a combination of a low-temperature magnetic force microscope (LTMFM) with a nanoSQUID. This system allows for magnetization measurements of nanoscaled magnetic samples using very different measuring principles, as presented elsewhere.[29] In the case of LTMFM, forces acting on the magnetic tip are detected, e.g. allowing for the imaging of Abrikosov vortices in superconductors[30, 31]. In the first part of the manuscript, with this technique we identify the position of trapped flux in the superconducting lead of the nanoSQUID operated in high magnetic fields. In contrast to the LTMFM, the nanoSQUID directly measures the stray flux from the magnetic tip coupled to the SQUID loop. Therefore, in the second part, we present measurements of $\Phi(\vec{r})$ for the half space above a nanoSQUID by scanning a LTMFM with a Ni nanotube at position $\vec{r}$ as a magnetic tip. Furthermore, we show that the nanoSQUID can be used as a highly sensitive detector of displacement of the Ni nanotube.

For the experiments presented here, we use a dc SQUID which has a sandwich-like geometry (see Fig. 1), i.e., the two arms of the SQUID loop lie directly on top of each other, and are connected via two $200 \times 200\,\mathrm{nm}^2$ planar Nb/HfTi/Nb Josephson junctions.[32, 33] For this geometry, the size of the SQUID loop (in the $x-z$ plane) is given by the gap ($\sim 225\,\mathrm{nm}$) between top and bottom Nb layers and the lateral distance ($\sim 1.8\,\mu\mathrm{m}$) between the two junctions. Using such a geometry, a very small loop size, and hence a small loop inductance of a few pH or even lower can be achieved, which is essential for obtaining very low values for S_Φ.[34] The rms flux noise for the SQUID used here is $S_\Phi^{1/2} \approx 220\,\mathrm{n}\Phi_0/\sqrt{\mathrm{Hz}}$ (in the white noise limit above $\sim 1\,\mathrm{kHz}$). This value was measured in a separate, magnetically and electrically shielded setup, using a sensitive cryogenic amplifier for SQUID readout. Details on the transport and noise properties on our Nb nanoSQUIDs will be given elsewhere.[35]

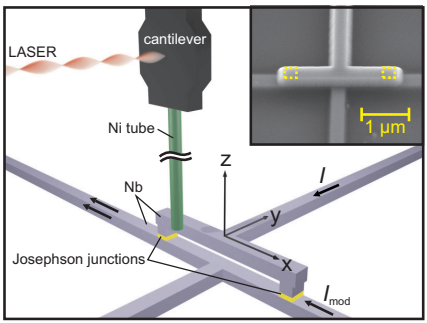

FIG. 1. (Color online) Schematic view (not to scale) of the nanoSQUID and Ni nanotube geometry, indicating x, y, z directions as used below, with the origin centered on the surface of the upper Nb layer. Thick arrows indicate flow of applied bias current I and modulation current I_{mod}. Inset shows scanning electron microscopy (SEM) image of the Nb nanoSQUID; dotted lines indicate the two Josephson junctions.

The nanoSQUID is mounted in a vacuum chamber (pressure $\lesssim 1 \times 10^{-6}\,\mathrm{mbar}$) at the bottom of a continuous-flow ^{3}He cryostat. The SQUID is biased at a current I slightly above its critical current and at a magnetic flux $\Phi_{\mathrm{mod}} \propto I_{\mathrm{mod}}$ coupled via the modulation current I_{mod} to the loop (cf. Fig. 1). In order to maintain operation of the SQUID at its optimum working point, i.e., at the maximum slope of its $V(\Phi)$ curve, we use a flux-locked loop (FLL) with a room-temperature voltage preamplifier. The FLL couples a feedback flux $\Phi_f = -\Phi$ in order to compensate for any flux signal Φ. Using such a scheme, the output voltage $V_{\mathrm{out}} \propto I_{\mathrm{mod}}$ provided by the feedback loop is directly proportional to Φ; in our case $V_{\mathrm{out}}/\Phi = 2.55\,\mathrm{V}/\Phi_0$.

The magnetic tip used in our LTMFM setup is a $\ell = 6\,\mu\mathrm{m}$ long Ni nanotube with $D_a \approx 175\,\mathrm{nm}$ outer diameter and $t \approx 40\,\mathrm{nm}$ thickness, yielding a volume $V_{\mathrm{Ni}} = \pi t(D_a - t)\ell \approx 0.10\,\mu\mathrm{m}^3$. It is fabricated by atomic layer deposition of Ni and a $\sim 10\,\mathrm{nm}$ thick AlO_x interlayer on a 75 nm diameter GaAs nanowire.[36] The Ni nanotube is affixed parallel to the cantilever axis (z-axis) such that it protrudes from the cantilever end by $4\,\mu\mathrm{m}$. We define the position $\vec{r} = (x, y, z)$ of the Ni tip (relative to the SQUID) as the intersection point of its cylindrical axis with the bottom end of the tube. The cantilever hangs above the SQUID in the pendulum geometry, i.e., perpendicular to the scanned surface (in the x-y plane; cf. Fig. 1).[37] A 3D piezo-electric positioning stage (Attocube Systems AG) moves the SQUID relative to the Ni nano-magnet. In non-contact scanning force microscopy, the above described configuration prevents the tip of the cantilever from snapping into contact with the sample surface and thus allows for the use of particularly soft – and therefore sensitive – cantilevers (spring constant $\lesssim 1\,\mathrm{mN/m}$). The single-crystal Si cantilever used here is $90\,\mu\mathrm{m}$ long, $4\,\mu\mathrm{m}$ wide, and $0.1\,\mu\mathrm{m}$ thick and includes a $15\,\mu\mathrm{m}$ long, $1\,\mu\mathrm{m}$ thick mass on its end.[38] The oscillation of the lever along y-direction is detected using laser light focused onto a $10\,\mu\mathrm{m}$ wide paddle near the mass-loaded end and reflected back into an optical fiber interferometer.[39] 100 nW of light are incident on the paddle from a temperature-tuned 1550 nm distributed feedback laser diode.

At temperature $T = 4.3\,\mathrm{K}$ and applied magnetic field $H = 0$, the nano-magnet-loaded cantilever has a resonance frequency $f_{\mathrm{res}} = 3413\,\mathrm{Hz}$ and an intrinsic quality factor $Q_0 = 3.4 \times 10^4$. Its spring constant is determined to be $k = 90\,\mu\mathrm{N/m}$ through measurements of its thermal noise spectrum at several different temperatures. As a result, far from the SQUID, where surface interactions do not play a role,[40, 41] the cantilever has a thermally

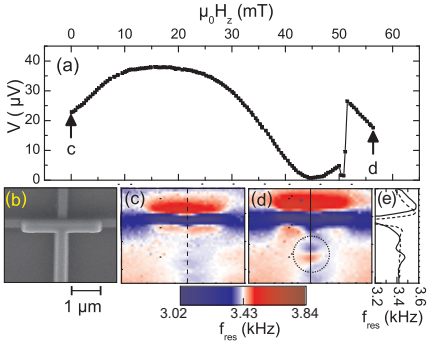

FIG. 2. MFM imaging of trapped flux: (a) $V(H)$ for a single sweep from 0 to 56 mT; labels c, d indicate field values for LTMFM images shown in (c) and (d). (b) SEM image of the nanoSQUID. (c,d) LTMFM images $f_{res}(x, y)$, without trapped vortices at $H = 0$ (c) and with a trapped vortex (indicated by dotted circle) at $\mu_0 H = 56$ mT (d). (e) linescans along dashed line in (c) (dashed curve) and solid line in (d) (solid curve).

limited force sensitivity of $10\,\mathrm{aN}/\sqrt{\mathrm{Hz}}$. The interferometric cantilever deflection signal is fed through a field programmable gate array (FPGA) (National Instruments) circuit back to a piezoelectric element which is mechanically coupled to the cantilever. In this way, it is possible to self-oscillate the cantilever at its fundamental resonance frequency and at a desired amplitude.

We produce non-contact force microscopy images by scanning (in the x-y plane for fixed z) the position of the nanomagnet-tipped cantilever over the SQUID and simultaneously measuring the cantilever resonance frequency $f_{res}(x, y)$, which is proportional to the force gradient $\partial F/\partial y$ acting on the nanomagnet-tipped cantilever. From such images we can identify the topography of the nanoSQUID, allowing us to precisely position the Ni nanotube with respect to the nanoSQUID. At the same time, due to the magnetization of the Ni nanotube tip, the images show features produced by the diamagnetic response of the superconductor.

Prior to the measurements of the magnetic flux coupled by the Ni tip to the SQUID, we investigate a possible impact of an applied magnetic field on the nanoSQUID, since Abrikosov vortices may enter the superconducting areas, degrading its performance. H is aligned along z direction, with a possible tilt of a few degrees. The trapping of a vortex appears as a voltage jump in the periodic $V(H)$ characteristics, when the SQUID voltage is measured directly, rather than using the FLL readout. Note that the SQUID voltage oscillates with increasing H, due to the non-perfect alignment of H along the z direction, i.e., H has a finite in-plane component, which induces magnetic flux threading the SQUID loop. From the effective area of the SQUID and the oscillation period of $V(H)$, we estimate a tilt of the applied field of $\sim 2^\circ$ with respect to the z axis. An example for a vortex trapping process is shown in Fig. 2(a), where a huge jump in $V(H)$ occurs near $\mu_0 H = 50$ mT. We note that during the field sweep, the Ni tip was retracted from the SQUID. For further improvement of the SQUID layout the knowledge of the position of trapped vortices is indispensable. The ability of the LTMFM setup to image stray fields can be used to image vortices in the superconductors as well as the magnetic field of the screening currents of the nanoSQUID itself. In Fig. 2(d), taken at a magnetic field above the jump in $V(H)$, such a vortex is visible in the superconducting lead (top Nb layer) of the nanoSQUID. The vortex appears as a distortion in the otherwise flat resonance frequency f_{res} distribution along the Nb-line (cf. linescans in Fig. 2(e)). In the given setup $\Delta f_{\mathrm{res}} \propto \partial^2 B_z/\partial y^2$, a tripolar response is expected, which might be distorted due to the influence of the screening currents in the SQUID or a remaining magnetization of the Ni nanotube in the x-y-plane. In contrast, at fields below the jump the trapped vortex is absent [see Fig. 2(c)]. For the subsequent investigations, we operate the SQUID in nominally zero field only, i.e., trapped vortices do not play a role.

In order to determine $\Phi(\vec{r})$ we measure the nanoSQUID signal, i.e., the magnetic flux Φ through the SQUID loop as a function of the Ni nanotube position (x, y) for fixed z. Such measurements produce images $\Phi(x, y)$ of the spatially dependent magnetic coupling of the Ni nanotube to the nanoSQUID. The experiment was performed in the following way: First, we bring the Ni nanotube into a well-defined saturated magnetic state along its easy axis. This is done by a half magnetization cycle, i.e., a sweep of H (aligned along z direction, as above) from zero to $\mu_0 H_{\mathrm{max}} = -150$ mT and back to $H = 0$. From previous experiments, we know that H_{max} is strong enough to saturate the magnetization of the Ni nanotube.[36, 42] In order to avoid trapped flux in the SQUID, the magnetization cycle is performed at $T = 14$ K, i.e., significantly above the transition temperature $T_c \sim 9$ K of the Nb SQUID. Subsequently, we zero-field cool the SQUID to its operation temperature $T = 4.3$ K, and then set up the FLL readout for the SQUID. For various distances z between the tip and the top Nb layer of the SQUID we make scans in the x-y plane with a scan range of about $6 \times 7\,\mu\mathrm{m}^2$ corresponding to 81×81 pixels. The scans start at the largest distance of $z \approx 700$ nm. In steps of 50 nm the distance is subsequently reduced until the tip touches the top Nb layer of the SQUID (at $z = 0$), which is detected as a loss of the oscillation of the cantilever. The touchpoint is also necessary for the calibration of the $z = 0$ position.

Figure 3(a,b) shows two representative $\Phi(x, y)$ images taken at $z = 100$ nm (a) and $z = 710$ nm (b). The images show a bipolar flux response, i.e., when the tip crosses the SQUID loop the flux signal is inverted. For the closer distance [Fig. 3(a)] the induced flux is stronger

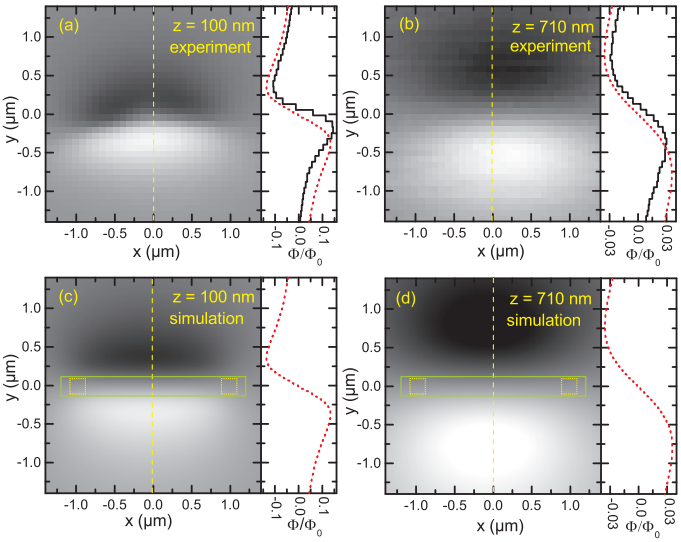

FIG. 3. Magnetic flux Φ generated in the SQUID vs x-y position of the Ni nanotube (magnetized along z-axis). In (c) and (d), solid rectangle and dotted squares indicate position of the SQUID and the two junctions, respectively. Vertical dashed lines indicate position of linescans $\Phi(y)$ to the right of each image. Upper graphs (a, b) show experimental results and lower graphs (c, d) show corresponding simulation results for $z = 100\,\mathrm{nm}$ (left graphs) and $z = 710\,\mathrm{nm}$ (right graphs). For the simulation we assumed $M_s = 1.9 \times 10^5$ A/m. Linescans in (a,b) also include calculated linescans from (c,d).

and spatially more confined as compared with the larger distance [Fig. 3(b)]. At $z = 100\,\mathrm{nm}$, we obtain $\Delta\Phi = \Phi_{\max} - \Phi_{\min} \approx 0.26\,\Phi_0$, with the positions of the maximum $\Phi_{\max}$ and minimum $\Phi_{\min}$ in the linescan $\Phi(y)$ (at $x = 0$) being separated by $\Delta y = 370\,\mathrm{nm}$. For $z = 710\,\mathrm{nm}$, we find $\Delta\Phi \approx 0.06\Phi_0$ and $\Delta y = 750\,\mathrm{nm}$.

In order to analyze the measured flux signals, we start from numerical simulations of $\phi_\mu(\vec{r}_p)$ for a point-like SMP at position $\vec{r}_p$. Figure 4 shows the calculated coupling factor ϕ_μ in the y-z plane, with the SQUID loop in the x-z plane and the magnetic moment pointing along the $-z$-direction. ϕ_μ decreases with increasing distance from the SQUID loop and inverts when crossing the SQUID loop. This spatial dependence has a strong impact on the magnetic flux $\Phi(\vec{r})$ which is coupled by a Ni nanotube (at position $\vec{r}$) with finite size into the SQUID. For the calculation of $\Phi(\vec{r})$ we integrate ϕ_μ over the volume V_{Ni} of the Ni nanotube at position $\vec{r}$ and multiply this with the Ni saturation magnetization M_s, i.e., $\Phi(\vec{r}) = M_s \int_{V_{\mathrm{Ni}}(\vec{r})} \phi_\mu(\vec{r}_p) dV$, assuming a homogeneous M_s over the entire volume of the Ni nanotube.

Figure 3 (c) and (d) show calculated flux images $\Phi(x, y)$ for $z = 100$ and $710\,\mathrm{nm}$, respectively, of a tube with the above mentioned geometric dimensions and a saturation magnetization M_s along $-z$-direction [cf. Fig.4]. The bipolar flux response and the positions of the minima $\Phi_{\min}$ and maxima $\Phi_{\max}$ in $\Phi(y)$ (for $x = 0$) are reproduced well by the simulations.

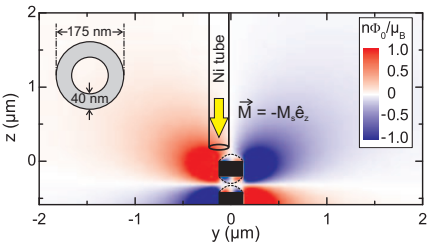

FIG. 4. (color online) Calculated coupling factor ϕ_μ in the y-z plane ($x = 0$) for a point-like magnetic particle with magnetic moment $\vec{\mu}$ along $-\hat{e}_z$. Black rectangles indicate position of the Nb top and bottom layer; dotted lines include regions for which the simulations produce unphysical results.[43] A sketch of the bottom part of the Ni nanotube (drawn to scale) is shown within the coupling map in order to illustrate the spatial dependence of the coupling factor within the volume of the tube. Upper left inset schematically shows a zoomed cross-section of the Ni nanotube.

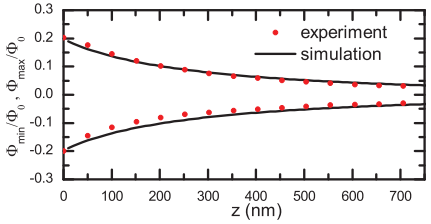

FIG. 5. Experimental and simulated minimum and maximum flux signals, $\Phi_{\min}$ and $\Phi_{\max}$, versus distance z. For the simulation we assumed $M_s = 1.9 \times 10^5$ A/m.

For a quantitative analysis, Fig. 5 compares experimentally obtained $\Phi_{\min}$ and $\Phi_{\max}$ for all investigated distances to the simulated ones. For the best quantitative agreement we assume a homogeneous saturation magnetization $M_s = 1.9 \times 10^5$ A/m of the Ni nanotube. This is a factor of 2.1 less than the value 4×10^5 A/m from literature.[44] This could be due to e.g. different geometrical dimensions of the Ni nanotube, voids in the Ni layer,[36] magnetically dead layers (e.g. due to surface oxidation) or a multi-domain state. We note, however, that the formation of a multidomain state close to the bottom of the Ni is unlikely, as hysteresis curves $M(H)$ measured both with SQUID and cantilever magnetometry indicate no reduction of magnetic signal upon sweeping H from $\pm H_{\max}$ back to zero.[29] In the experiment we also find an asymmetry in $\Phi(y)$, i.e. $\Phi_{\max} \geq |\Phi_{\min}|$. This effect is most likely caused by flux focusing effects of the feed lines in the top and bottom Nb layers, which are not considered in the simulations. The flux focusing effects are also visible in the distorted flux image (broken horizontal symmetry) in Fig.3(a). An additional asymmetry may be caused by a slightly tilted tube with respect to the SQUID plane. In our case however, this effect is considered to be small, since the tilt angle is measured to be less than 5°.

Finally, we discuss the sensitivity of our setup for the detection of the oscillatory motion of the cantilever by the SQUID.[45, 46] While the absolute flux signal from the Ni nanotube is optimally detected at the positions yielding $\Phi_{\max}$ and $\Phi_{\min}$, for the cantilever displacement detection, a large gradient $\partial\Phi/\partial y$ is required. The linescans in Fig. 3 clearly show that the optimum position for displacement detection is directly above the SQUID. For our device, we find for $z = 50$ nm a gradient $\Phi_y \equiv \partial\Phi/\partial y = 2 \times 10^6\,\Phi_0/\mathrm{m}$. With the flux noise $S_\Phi^{1/2} = 220\,\mathrm{n}\Phi_0/\sqrt{\mathrm{Hz}}$, this yields an extremely low value for the predicted displacement sensitivity $S_r^{1/2} = S_\Phi^{1/2}/\Phi_y = 110\,\mathrm{fm}/\sqrt{\mathrm{Hz}}$, which is already more than one order of magnitude below the values found in literature.[45, 46] Still, S_r is by far not optimized and could be further improved by using a reduced linewidth for the SQUID arm in the top Nb layer and by increasing the number of spins in the magnet.

In conclusion, we experimentally determined the spatial dependence of the magnetic coupling between a Ni nanotube and a Nb nanoSQUID. Operating the nanoSQUID in a flux locked loop, we measured the flux through the SQUID loop $\Phi(\vec{r})$ generated by the Ni nanotube during the scan of the tip in 3D space above the nanoSQUID. Our results are in good agreement with a recently developed routine for numerical calculation of the coupling factor between a small magnetic particle and a nanoSQUID. This provides an important step toward the development of optimized nanoSQUIDs for the investigation of small magnetic particles. With the presented measurement system, we demonstrate a reliable and non-destructive *in situ* tool for the challenging task of positioning a nano-scaled magnet to the position of highest coupling of a nanoSQUID. Furthermore, with a proper readout technique, our highly flux-sensitive nanoSQUID can be used for displacement detection of the cantilever in an MFM with extremely good displacement sensitivity, which still can be further improved. Finally, by using an MFM imaging mode, we also demonstrate the imaging of Abrikosov vortices, which are trapped at high magnetic fields in the superconducting leads of the nanoSQUID. This technique is useful for the improvement of the high-field suitability of nanoSQUIDs.

J. Nagel acknowledges support by the Carl-Zeiss-Stiftung. This work was funded by the Deutsche Forschungsgemeinschaft (DFG) via the SFB/TRR 21, by the European Research Council via ERC advanced grant SOCATHES, by the Canton Aargau, and by the Swiss National Science Foundation (SNF, Grant No. 200020-140478). The research leading to these results has received funding from the European Community's Seventh Framework Programme (FP7/2007-2013) under Grant Agreement No. 228673 MAGNONICS.

[1] L. Thomas, F. Lionti, R. Ballou, D. Gatteschi, R. Sessoli, and B. Barbara. Macroscopic quantum tunnelling of magnetization in a single crystal of nanomagnets. Nature, 383:145–147, 1996.

[2] D. Gatteschi and R. Sessoli. Quantum tunneling of magnetization and related phenomena in molecular materials. Angew. Chem., Int. Ed., 42:268–297, 2003.

[3] L. Bogani and W. Wernsdorfer. Molecular spintronics using single-molecule magnets. Nature Materials, 7:179–186, 2008.

[4] L. Bogani, A. Vindigni, R. Sessoli, and D. Gatteschi. Single chain magnets: where to from here? J. Mater. Chem., 18:4750–4758, 2008.

[5] P. Bushev, D. Bothner, J. Nagel, M. Kemmler, K. B.

Konovalenko, A. Loerincz, K. Ilin, M. Siegel, D. Koelle, R. Kleiner, and F. Schmidt-Kaler. Trapped electron coupled to superconducting devices. Eur. Phys. J. D, 63:9–16, 2011.

[6] J. Fortágh and C. Zimmermann. Toward atom chips. Science, 307:860–861, 2005.

[7] J. R. Maze, P. L. Stanwix, J. S. Hodges, S. Hong, J. M. Taylor, P. Cappellaro, L. Jiang, M. V. Gurudev Dutt, E. Togan, A. S. Zibrov, A. Yacoby, R. L. Walsworth, and M. D. Lukin. Nanoscale magnetic sensing with an individual electronic spin in diamond. Nature, 455:644–647, 2008.

[8] G. Balasubramanian, I. Y. Chan, R. Kolesov, M. Al-Hmoud, J. Tisler, C. Shin, C. Kim, A. Wojcik, P. R. Hemmer, A. Krueger, T. Hanke, A. Leitenstorfer, R. Bratschitsch, F. Jelezko, and J. Wrachtrup. Nanoscale imaging magnetometry with diamond spins under ambient conditions. Nature, 455:648–651, 2008.

[9] D. Rugar, R. Budakian, H. J. Mamin, and B. W. Chui. Single spin detection by magnetic resonance force microscopy. Nature, 430:329–332, 2004.

[10] Y. Manassen, R. J. Hamers, J. E. Demuth, and A. J. Castellano Jr. Direct observation of the precession of individual paramagnetic spins on oxidized silicon surfaces. Phys. Rev. Lett., 62:2531–2534, 1989.

[11] C. Durkan and M. E. Welland. Electronic spin detection in molecules using scanning-tunneling- microscopy-assisted electron-spin resonance. Appl. Phys. Lett., 80(3):458–460, 2002.

[12] W. Wernsdorfer. Classical and quantum magnetization reversal studied in nanometersized particles and clusters. Adv. Chem. Phys., 118:99–190, 2001.

[13] J. Gallop. SQUIDs: some limits to measurement. Supercond. Sci. Technol., 16:1575–1582, 2003.

[14] R. Kleiner, D. Koelle, F. Ludwig, and J. Clarke. Superconducting Quantum Interference Devices: State-of-the-Art and Applications. Proc. IEEE, 92:1534–1548, 2004.

[15] C. P. Foley and H. Hilgenkamp. Why NanoSQUIDs are important: an introduction to the focus issue. Supercond. Sci. Technol., 22:064001, 2009.

[16] M. Ketchen, D. Awschalom, W. Gallagher, A. Kleinsasser, R. Sandstrom, J. Rozen, and B. Bumble. Design, fabrication, and performance of integrated miniature SQUID susceptometers. IEEE Trans. Magn., 25:1212–1215, 1989.

[17] V. Bouchiat. Detection of magnetic moments using a nano-squid: limits of resolution and sensitivity in near-field squid magnetometry. Supercond. Sci. Technol., 22:064002, 2009.

[18] J. Nagel, K. B. Konovalenko, M. Kemmler, M. Turad, R. Werner, E. Kleisz, S. Menzel, R. Klingeler, B. Büchner, R. Kleiner, and D. Koelle. Resistively shunted $YBa_2Cu_3O_7$ grain boundary junctions and low-noise SQUIDs patterned by a focused ion beam down to 80 nm linewidth. Supercond. Sci. Technol., 24:015015, 2011.

[19] R. F. Voss, R. B. Laibowitz, and A. N. Broers. Niobium nanobridge dc SQUID. Appl. Phys. Lett., 37:656–658, 1980.

[20] J. Nagel, O. F. Kieler, T. Weimann, R. Wölbing, J. Kohlmann, A. B. Zorin, R. Kleiner, D. Koelle, and M. Kemmler. Superconducting quantum interference devices with submicron Nb/HfTi/Nb junctions for investigation of small magnetic particles. Appl. Phys. Lett., 99:032506, 2011.

[21] A. G. P. Troeman, H. Derking, B. Borger, J. Pleikies, D. Veldhuis, and H. Hilgenkamp. NanoSQUIDs based on niobium constrictions. Nano Lett., 7:2152–2156, 2007.

[22] L. Hao, J. C. Macfarlane, J. C. Gallop, D. Cox, J. Beyer, D. Drung, and T. Schurig. Measurement and noise performance of nano-superconducting-quantum-interference devices fabricated by focused ion beam. Appl. Phys. Lett., 92(19):192507, 2008.

[23] V. Bouchiat, M. Faucher, C. Thirion, W. Wernsdorfer, T. Fournier, and B. Pannetier. Josephson junctions and superconducting quantum interference devices made by local oxidation of niobium ultrathin films. Appl. Phys. Lett., 79:123–125, 2001.

[24] M. Faucher, P.-O. Jubert, O. Fruchart, W. Wernsdorfer, and V. Bouchiat. Optimizing the flux coupling between a nanoSQUID and a magnetic particle using atomic force microscope nanolithography. Supercond. Sci. Technol., 22:064010, 2009.

[25] A. Finkler, Y. Segev, Y. Myasoedov, M. L. Rappaport, L. Neeman, D. Vasyukov, E. Zeldov, M. E. Huber, J. Martin, and A. Yacoby. Self-aligned nanoscale SQUID on a tip. Nano Lett., 10:1046–1049, 2010.

[26] J.-P. Cleuziou, W. Wernsdorfer, V. Bouchiat, T. Ondarcuhu, and M. Monthioux. Carbon nanotube superconducting quantum interference device. Nature Nanotechnology, 1:53–59, 2006.

[27] C. Granata, A. Vettoliere, R. Russo, E. Esposito, M. Russo, and B. Ruggiero. Supercurrent decay in nano-superconducting quantum interference devices for intrinsic magnetic flux resolution. Appl. Phys. Lett., 94:062503, 2009.

[28] M. M. Khapaev, A. Yu. Kidiyarova-Shevchenko, P. Magnelind, and M. Yu. Kupriyanov. 3D-MLSI: Software package for inductance calculation in multilayer superconducting integrated circuits. IEEE Trans. Appl. Supercond., 11:1090–1093, 2001.

[29] A. Buchter et al. unpublished, 2012.

[30] A. Moser, H. J. Hug, I. Parashikov, B. Stiefel, O. Fritz, H. Thomas, A. Baratoff, and H.-J. Güntherodt. Observation of single vortices condensed into a vortex-glass phase by magnetic force microscopy. Phys. Rev. Lett., 74:1847–1850, 1995.

[31] A. Volodin, K. Temst, C. Van Haesendonck, Y. Bruynseraede, M. I. Montero, and I. K. Schuller. Magnetic-force microscopy of vortices in thin niobium films: Correlation between the vortex distribution and the thickness-dependent film morphology. Europhys. Lett., 58:582–588, 2002.

[32] D. Hagedorn, R. Dolata, F.-Im. Buchholz, and J. Niemeyer. Properties of SNS Josephson junctions with HfTi interlayers. Physica C, 372–376:7–10, 2002.

[33] D. Hagedorn, O. Kieler, R. Dolata, R. Behr, F. Müller, J. Kohlmann, and J. Niemeyer. Modified fabrication of planar sub-μm superconductor-normal metal-superconductor Josephson junctions for use in a Josephson arbitrary waveform synthesizer. Supercond. Sci. Technol., 19:294–298, 2006.

[34] D. J. Van Harlingen, R. H. Koch, and J. Clarke. Superconducting quantum interference device with very low magnetic flux noise energy. Appl. Phys. Lett., 41:197–199, 1982.

[35] R. Wölbing et al. unpublished, 2012.

[36] D. Rüffer, R. Huber, P. Berberich, S. Albert, E. Russo-

Averchi, M. Heiss, J. Arbiol, A. Fontcuberta i Morral, and D. Grundler. Magnetic states of an individual Ni nanotube probed by anisotropic magnetoresistance. Nanoscale, 2012.

[37] U. Gysin, S. Rast, M. Kisiel, C. Werle, and E. Meyer. Low temperature ultrahigh vacuum noncontact atomic force microscope in the pendulum geometry. Rev. Sci. Instrum., 82:023705, 2011.

[38] B.W. Chui, Y. Hishinuma, R. Budakian, H.J. Mamin, T.W. Kenny, and D. Rugar. Mass-loaded cantilevers with suppressed higher-order modes for magnetic resonance force microscopy. 12th International Conference on Solid-State Sensors, Actuators and Microsystems (Transducers '03), 2:1120–1123, 2003.

[39] D. Rugar, H. J. Mamin, and P. Guenther. Improved fiber-optic interferometer for atomic force microscopy. Appl. Phys. Lett., 55:2588–2590, 1989.

[40] B. C. Stipe, H. J. Mamin, T. D. Stowe, T. W. Kenny, and D. Rugar. Noncontact friction and force fluctuations between closely spaced bodies. Phys. Rev. Lett., 87:096801, 2001.

[41] S. Kuehn, R. F. Loring, and J. A. Marohn. Dielectric fluctuations and the origins of noncontact friction. Phys. Rev. Lett., 96:156103, 2006.

[42] D. P. Weber et al. unpublished, 2012.

[43] For simulating the current distribution, we have to assume that the currents are flowing in surface sheets rather than across the entire width of the two Nb lines (in y-direction). This assumption allows for coupling of flux between the suface sheets, which produces the localized minima and maxima very close to the two SQUID arms, as visible in Fig. 4.

[44] C. Kittel. Introduction to Solid State Physics, 8th edition. J. Wiley & Sons, New York, 2005.

[45] O. Usenko, A. Vinante, G. Wijts, and T. H. Oosterkamp. A superconducting quantum interference device based read-out of a subattonewton force sensor operating at millikelvin temperatures. Appl. Phys. Lett., 98:133105, 2011.

[46] A. Vinante, G. Wijts, O. Usenko, L. Schinkelshoek, and T.H. Oosterkamp. Magnetic resonance force microscopy of paramagnetic electron spins at millikelvin temperatures. Nature Communications, 2:572, 2011.

Publication 5

Low-noise nanoSQUIDs operating in Tesla magnetic fields – towards detection of small spin systems with single-spin resolution

T. Schwarz, J. Nagel, R. Wölbing, R. Kleiner,[a] D. Koelle, and M. Kemmler
Physikalisches Institut – Experimentalphysik II and Center for Collective Quantum Phenomena in LISA$^+$, Universität Tübingen, Auf der Morgenstelle 14, D-72076 Tübingen, Germany

We investigate the noise performance of a $YBa_2Cu_3O_7$ nanoSQUID in magnetic fields up to $B = 1\,\mathrm{T}$. The dc SQUID incorporates two grain boundary Josephson junctions and a 90 nm wide constriction which is used to modulate the flux through the SQUID loop. The white flux noise of the device increases only slightly from $1.3\,\mu\Phi_0/\mathrm{Hz}^{1/2}$ at B=0 to $2.3\,\mu\Phi_0/\mathrm{Hz}^{1/2}$ at 1 T. Assuming that a small particle is placed directly on top of the YBCO film at the constriction, we calculate a spin sensitivity $S_\mu^{1/2}$=$62\,\mu_B/\mathrm{Hz}^{1/2}$ at $B = 0$ and $110\,\mu_B/\mathrm{Hz}^{1/2}$ at 1 T. We also present a systematic optimization study of this type of device; this shows that $S_\mu^{1/2}$ of a few $\mu_B/\mathrm{Hz}^{1/2}$ should be feasible for optimized geometrical and electrical parameters.

PACS numbers: 85.25.CP, 85.25.Dq, 74.78.Na, 74.72.-h 74.25.F- 74.40.De

Growing interest in the detection and investigation of small spin systems like single-molecular/single chain magnets[1,2], cold atom clouds[3] or even single electrons/atoms[4] demands for sensors that are sensitive to very small changes of the magnetization of small particles with the ultimate goal of single spin detection. The interest for the investigation of such particles affects many fields of research such as material science, information technology, medical and biological science or studies of quantum effects in mesoscopic matter. In order to meet the challenge of detecting a single spin, various types of detection techniques like magnetic resonance force microscopy[5], magneto-optic spin detection[6,7], Hall voltage measurements[8,9] and SQUID magnetometry[10–25] have been adapted. A crucial point is that in many cases very large magnetic fields in the Tesla range need to be applied to the sample. At the same time one would like to operate the magnetometer continuously, allowing, e.g. to record flux noise spectra of the sample under investigation. Miniaturized nanoSQUIDs have been operated in impressive background fields of up to 7 T[26]. These SQUIDs were made of $d_F \sim 5.5\,\mathrm{nm}$ thin Nb films and incorporated nanobridges as Josephson junctions. However, there are two drawbacks in this design. First, the very low thickness of the Nb films causes the (kinetic) SQUID inductance $L(\propto d_F^{-1})$ and consequently the SQUID flux noise power S_ϕ ($\propto L$) to be large, i.e., typically about six orders of magnitude above the values obtained for sensitive state-of-the-art SQUIDs[27] (with $S_\Phi^{1/2} \sim 1\mu\Phi_0/\mathrm{Hz}^{1/2}$) optimized for operation in magnetic fields well below the earth's field. Second, the Josephson junctions have a hysteretic current voltage characteristic (IVC), preventing continuous measurements while having the SQUIDs biased at a small voltage slightly above the critical current I_c.

There is thus a clear need to develop "conventional" SQUIDs that can be operated at high background fields. The Josephson junctions should have nonhysteretic IVCs and the thickness of the SQUID should not be too low to allow for a small value of L. As for the ultrathin Nb SQUIDs[26] the "conventional" SQUID should incorporate at least one very thin and narrow section where the magnetic particle is placed, allowing for a good coupling of the magnetic flux of the particle to the SQUID. This all calls for a superconductor which has a very high critical field and allows for patterning nanosized structures and not too large Josephson junctions. The high-transition temperature superconductor $YBa_2Cu_3O_7$ (YBCO) fulfills these requirements. Compared to Nb, YBCO is not a mature material and grain-boundary type Josephson junctions exhibit a large $1/f$ noise as well as an appreciable scatter in their electrical parameters. Nonetheless, single SQUIDs with high spin sensitivity can be fabricated reproducibly. YBCO SQUIDs have already been used to measure magnetization curves of microscale magnets in fields above 0.1 T[28]. Below we show that this field scale can be extended to above 1 T and, as we will see below, allow, at least in principle, for a continuous detection of magnetic moments down to a few Bohr magnetons in high fields.

The YBCO nanoSQUIDs were made in a similar way, as described in Ref. 29. First, using pulsed laser deposition, epitaxial c-axis oriented YBCO thin films of thickness $d_F = 50\,\mathrm{nm}$ were grown on $SrTiO_3$ (STO) [001] bicrystal substrates with misorientation angle $\Theta = 24°$. Subsequently, a 60 nm thick Au layer was evaporated in-situ, serving as shunt resistance for the YBCO grain boundary junctions (providing nonhysteretic IVCs) and also acting as a protection layer during focused ion beam (FIB) milling. The critical temperature T_c of the YBCO film, measured inductively, was about 91 K. To obtain the nanoSQUID, structures with linewidths down to 1 μm (at the region of the grain boundary) were prepatterned by photolithography and Ar ion milling. Subsequently, two nanoscaled Josephson junctions and a constriction next to the SQUID loop, that permits modulation of the SQUID by applying an additional current I_{mod}, were pat-

[a] Electronic mail: kleiner@uni-tuebingen.de

terned by FIB using a FEI Dualbeam Strata 235. Parameters for FIB milling needed to be chosen carefully, as this patterning step can suppress superconductivity of YBCO even in regions outside the lateral penetration depth of the ions due to heating or electric charging. In the cutting scheme which finally permitted the fabrication of nanoscaled Josephson junctions with no significant reduction of the critical current density j_c, Ga ion currents where adjusted to 30 pA at an acceleration voltage of 30 kV. Four rectangular patterns cut line-by line (cleaning cross section cut), with cutting directions pointing away from the Josephson junctions, were placed at the grain boundary to form the final SQUID layout. Cutting deep into the STO substrate results in sloped junction edges due to redeposition of amorphous YBCO and STO which prevents oxygen outdiffusion from the YBCO film. With this procedure we could fabricate high performance SQUIDs with junction widths down to 80 nm. The SQUIDs had almost identical transport and noise characteristics. Below we discuss data of one device.

Fig. 1 shows a scanning electron microscope (SEM) image of the nanoSQUID. The grain boundary is indicated by the dashed line. The SQUID hole size is 300 nm × 400 nm. The junctions have a width $w_J \approx$ 130 nm. The lengths of the SQUID arms containing the junctions are $l_J \approx 400$ nm. The constriction has a length $l_c = 300$ nm and a width $w_c \approx 90$ nm. A bias current I_b flowing across the junctions, as well as a modulation current $I_{\rm mod}$ flowing across the constriction are applied as indicated by arrows in the graph.

The transport and noise measurements were performed at $T = 4.2$ K in an electrically shielded environment. We used a four terminal configuration with filtered lines to measure IVCs, I_c vs $I_{\rm mod}$ and V vs. $I_{\rm mod}$. For transport measurements, the voltage V across the SQUID was amplified using a room temperature amplifier. All currents were applied by battery powered current sources. Magnetic fields up to 7 T could be applied by a split coil superconducting magnet. As magnetic fields that couple into the Josephson junctions of the SQUID suppress their critical current and hence the modulation amplitude of the SQUID, the SQUID loop needed to be aligned with high accuracy parallel to the magnetic field and the in-plane field was aligned perpendicular to the grain boundary.

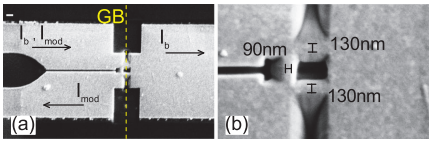

FIG. 1. (Color online) SEM images of the nanoSQUID. The grain boundary (GB) is indicated by the vertical dashed (yellow) line. In (a) the direction of the modulation and bias currents $I_{\rm mod}$ and I_b are indicated by arrows. In (b) the widths of the most narrow sections of the nanoSQUID are indicated.

To do so the sample was mounted on two goniometers with perpendicular tilt axes (minimum step size 10^{-4} deg.) and a rotator (minimum step size 10^{-4} deg.). Alignment was done by monitoring and maximizing I_c in a ~ 1 T background field. For noise measurements the voltage drop across the nanoSQUID was preamplified by a dc SQUID amplifier[30] with 0.1 nV/Hz$^{1/2}$ resolution and ~ 30 kHz bandwidth. To minimize stray fields the SQUID amplifier was placed inside a Nb shield mounted inside the cryostat at a position of minimum magnetic field. Still, for applied magnetic fields of about 1.5 T the SQUID amplifier trapped flux preventing noise measurements at higher fields.

Figure 2(a) shows the IVC of the nanoSQUID at zero applied field B and $I_{\rm mod} = 0$. The resistance of the device is $R/2 = 3.5\,\Omega$ (with R referring to the average junction resistance) and the critical current $I_c \approx 37\,\mu$A. Very slightly above I_c the voltage across the SQUID increases continuously from zero but then the IVC develops a small hysteresis between 15 and 70 μV. This is presumably caused by some Fiske or LC type resonance but prevented to accurately fit the resistive part of this IVC to a resistively and capacitively shunted junction (RCSJ) model[31,32]. Simulations using Langevin equations[33] were still possible for I_c vs applied field (or, respectively, I_c vs. $I_{\rm mod}$). The inset of 2(a) shows by the solid black line the measured I_c vs $I_{\rm mod}$ at $B = 0$. The data are fitted well by the Langevin simulations. For the simulations we have used a noise parameter $\Gamma = 2\pi k_B T/I_0 R = 0.01$, where $I_0 = 18.5\,\mu$A is the average junction critical current. We further used an inductance asymmetry $\alpha_L = (L_2 - L_1)/(L_1 + L_2) = 0.175$; L_1 and L_2 are the inductance of, respectively, the left and right arm of the SQUID, caused by asymmetric biasing of the device (cf. Fig. 1). We also used a junction critical current asymmetry $\alpha_i = (I_{02} - I_{01})/(I_{01} + I_{02}) = 0.22$ and further obtain $I_0 R = 130\,\mu$V. For the inductance parameter we obtain $\beta_L = 2I_0 L/\Phi_0 = 0.65$ and from here $L = 36$ pH. From the modulation period of I_c vs $I_{\rm mod}$ of $3.1\,{\rm m}\Phi_0/\mu$A we find for the inductance L_c of the constriction a value of 6.4 pH. Using $L_2 - L_1 \approx L_c$ we obtain $\alpha_{\rm L} \approx 0.18$ in agreement with the value found independently by fitting I_c vs. $I_{\rm mod}$. The final parameter to be determined is the Stewart-McCumber parameter $\beta_C \equiv 2\pi I_0 R^2/\Phi_0$. Since we cannot fit the experimental IVC accurately we cannot infer a precise number here, but the fact that small hysteresis show up in limited ranges of bias current and applied flux we assume that β_C is of the order of 1. Fig. 2(b) shows the V vs Φ characteristics of the device, plotted for bias currents ranging from $-49.5\,\mu$A to $49.5\,\mu$A. Near $I = I_c$ the curves are hysteretic. The maximum transfer function, i.e. the maximum slope of the $V(\Phi)$ curves at $B = 0$ determined for the nonhysteretic curves is $V_\Phi = 500\,\mu{\rm V}/\Phi_0$.

For further measurements the nanoSQUID was shunted by the input circuit of the SQUID amplifier with an input resistance $R_{\rm inp} = 10\,\Omega$. The additional shunt resistance reduces β_C yielding nonhysteretic IVCs and V

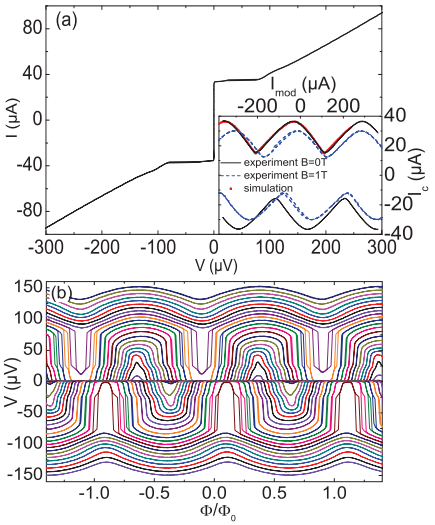

FIG. 2. (Color online) Transport characteristics of the nanoSQUID: (a) IVC at $I_{\rm mod} = 0\,\mu$A and zero applied field, $B = 0$. Inset shows measurement (black line) and numerical simulation (red squares) of the I_c vs $I_{\rm mod}$ characteristics for $B = 0$. Blue dashed line shows I_c vs. $I_{\rm mod}$ characteristics for $B = 1\,$T. (b) V vs $I_{\rm mod}$ at $B = 0$ for $I = -49.5 \ldots 49.5\,\mu$A (in $1.5\,\mu$A steps.)

vs $I_{\rm mod}$ characteristics. In this case the transfer function $|V_\Phi|$ is about $450\,\mu$V/Φ_0. At $B = 1\,$T (cf. dashed blue line in the inset of Fig. 2(a)) the I_c vs $I_{\rm mod}$ characteristics shows a slightly suppressed maximum critical current $I_c(1\text{T}) = 30\,\mu$A. This pattern is shifted in comparison to the $B = 0$ data, as the SQUID is not perfectly aligned to the magnetic field and flux couples into the Josephson junctions and the SQUID loop. In addition, when sweeping $I_{\rm mod}$ back and forth, a hysteresis becomes visible in a small interval of $I_{\rm mod}$, presumably caused by Abrikosov vortices trapped in the bias leads. Flux jumps caused by Abrikosov vortices also affect the modulation period, reducing it by about 5% in the interval plotted in Fig. 2(a). Magnetic fields were increased up to 3 T and still I_c vs $I_{\rm mod}$ characteristics with only a slightly suppressed maximum critical current $I_c = 24\,\mu$A could be measured. But as mentioned before, noise measurements could not be performed for fields much higher than 1 T since the amplifier trapped flux.

Figure 3 summarizes the flux noise spectra of the nanoSQUID at $B = 0$ and $B = 1\,$T at the optimum working point. As measurements were performed without magnetic shielding noise spikes occur on both spectra. The noise measurements were corrected for the noise contribution of the amplifier. In both cases $S_\Phi^{1/2}$ increases for frequencies below ∼3 kHz, a behavior which at least for $B = 0$ is known to arise from critical current fluctuations of the junctions. This contribution can in principle be eliminated by proper modulation techniques (bias reversal)[34]. At $B = 1\,$T there are presumably additional contributions due to fluctuating Abrikosov vortices. Note, however, that between ∼300 Hz and 3 kHz the noise level is less than a factor of 2 higher at $B = 1\,$T compared to $B = 0$. The decrease in $S_\Phi^{1/2}$ above 10 kHz is caused by the limited bandwidth of our measurement setup. At $B = 0$ the white noise level averaged between 6 and 7 kHz is $1.3\,\mu\Phi_0/\text{Hz}^{1/2}$. For $B = 1\,$T we determine a rms flux noise of $2.3\,\mu\Phi_0/\text{Hz}^{1/2}$ averaged between 6 and 7 kHz.

These numbers may be compared to the theoretical expression obtained from Langevin simulations,

$$S_\Phi \approx f(\beta_L)\Phi_0 k_B T L/I_0 R, \qquad (1)$$

which is valid for $\beta_C < 1$[35]. For $\beta_L > 0.4$, $f(\beta_L) \approx 4(1+\beta_L)$. For lower values of β_L, S_Φ increases. For the parameter of our device one obtains for $S_\Phi^{1/2}$ a value of $0.23\,\mu\Phi_0/\text{Hz}^{1/2}$, i.e. a factor of almost 6 less than the experimental value at $B = 0$. Such an excess noise is not unusual for YBCO SQUIDs[34].

In order to estimate the spin sensitivity $S_\mu^{1/2}$ of the nanoSQUID we numerically calculated the coupling factor ϕ_μ, i.e. the flux coupled into the SQUID loop by one Bohr magneton μ_B using 3DMLSI[36]. Details about the calculation procedure can be found in Ref. 29. In brief, one calculates the magnetic field distribution $B(\vec{r})$ generated by a current I circulating around the SQUID hole.

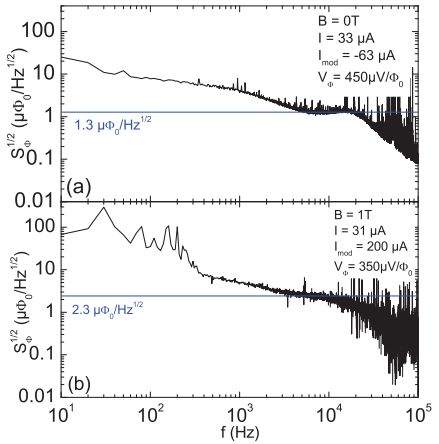

FIG. 3. (Color Line) Noise spectra of the nanoSQUID at optimum working points (a) at $B = 0\,$T and (b) at $B = 1\,$T. The horizontal (blue) lines indicate the white noise levels.

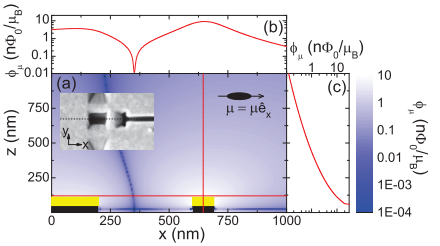

FIG. 4. (Color online) (a) Coupling factor ϕ_μ vs position of a magnetic moment pointing in x-direction. (b) horizontal linescan of ϕ_μ in a distance of 10 nm above the Au layer. (c) vertical linescan of ϕ_μ at the center of the constriction.

The coupling factor is obtained from $\phi_\mu = -\widehat{e}_\mu B(\vec{r})/I$. Here, $\widehat{e}_\mu$ is the direction of the magnetic moment at position $\vec{r}$. The results of these calculations are summarized in Fig. 4. The contour plot (a) shows ϕ_μ for a plane perpendicular to the nanoSQUID loop, indicated by the dotted line in the inset. The magnetic moment is assumed to point in x-direction. Figure 4(b) shows a linescan through this plane, as indicated by the horizontal line in (a). The linescan is taken at a distance of 10 nm above the Au layer. ϕ_μ has a maximum of $9.2\,\mathrm{n}\Phi_0/\mu_\mathrm{B}$ at the position of the constriction at $x \approx 0.64\,\mu$m. Figure 4(c) shows a linescan taken along the vertical line in graph (a). ϕ_μ decreases strongly with increasing z. Calculating the spin sensitivity $S_\mu^{1/2} = S_\Phi^{1/2}/\phi_\mu$ at $B = 0$ we obtain $141\,\mu_B/\mathrm{Hz}^{1/2}$. For $B = 1\,\mathrm{T}$ the spin sensitivity is $250\,\mu_B/\mathrm{Hz}^{1/2}$. In principle the Au layer could be removed above the constriction and a particle could indeed be positioned here. In this case $\phi_\mu = 21\,\mathrm{n}\Phi_0/\mu_\mathrm{B}$ and $S_\mu^{1/2} = 62\,\mu_B/\mathrm{Hz}^{1/2}$ at $B = 0$ and $S_\mu^{1/2} = 110\,\mu_B/\mathrm{Hz}^{1/2}$ at $B = 1\,\mathrm{T}$.

Optimizing the SQUID for spin sensitivity means to minimize the ratio S_Φ/ϕ_μ^2. The maximum value for ϕ_μ is essentially determined by the geometry of the constriction, i.e., its length l_c, width w_c and thickness d_c. S_Φ depends on the inductance of the SQUID, as well as on the junction parameters I_0, R and C. If the constriction could be made not only arbitrarily thin and narrow, but also arbitrarily short, one could envision a scenario, where ϕ_μ reaches a value around $0.5\,\Phi_0/\mu_B$,[13] while, at the same time, the inductance of the constriction remains small. Then, S_Φ could be optimized independently by proper choice of the SQUID size and the junction properties. For the type of device we discuss here, this is certainly not the case and we thus look for an optimization, which is compatible with technological limitations. We will assume, that the film thickness d_F is the same everywhere, and in particular we will use $d_c = d_F$. We will further assume a minimum, technologically limited length $l_c = 200\,\mathrm{nm}$ for the constriction. A large coupling ϕ_μ demands as narrow as possible constrictions. On the other hand, for too narrow constrictions, given a fixed value of d_F, its inductance L_c and thus also the total inductance L of the SQUID may become too large, possibly degrading the flux noise. This may be counterbalanced by choosing a different film thickness and changing, e.g., the junction width w_J.

To quantify all this we start from $S_\mu = S_\Phi/\phi_\mu^2$ and use Eq. (1) to calculate S_Φ. I_0R cannot be arbitrarily large, since $\beta_C < 1$ is required for keeping the junctions nonhysteretic. In a first step we will fix β_C at some value $\beta_{C0}(\sim 0.7)$ by choosing a proper value for R. To some extent, R can be controlled by the thickness of the Au layer covering the junctions. It is natural to assume that $C \propto w_J$. Further, if the stray capacitance between the junction and the substrate dominates, C will be independent of d_F, i.e. $C = C'w_J$, where C' is the junction capacitance per length (50–70 aF/nm)[37]. For a given junction critical current density $j_0{=}I_0/(w_Jd_F)$ (below we use $2\times10^5\,\mathrm{A/cm^2}$) we have $\beta_{C0}{=}\frac{2\pi}{\Phi_0}j_0C'{\cdot}w_J^2d_FR^2$ and thus $R \propto (w_J\sqrt{d_F})^{-1}$ and $I_0R{=}\ c_0\sqrt{d_F}$, with $c_0 \equiv (\frac{\Phi_0}{2\pi}\frac{j_0\beta_{C0}}{C'})^{1/2}$. We next fix β_L to some value β_{L0}, to be calculated later. We achieve this for given L and d_F by changing I_0 via w_J, i.e., we use $w_J = \Phi_0\beta_{L0}/2j_0d_FL$. Then, the quantity to be minimized is $s_\mu = f(\beta_{L0})Ld_F^{-1/2}/\phi_\mu^2$. S_μ is obtained via $S_\mu = s_\mu k_BT\Phi_0/c_0$.

Varying w_J also changes L, which we thus will have to find self-consistently. We write $L = L_c + 2L_J + L_r$, where L_c and L_J, respectively, denote the inductance of the constriction and one of the SQUID arms containing a junction. We assume that these SQUID arms are symmetric. L_r denotes all other contributions to L. We should find L_c (L_r) as functions of constriction (junction arm) thickness w_c (w_J) and length l_c (l_J), and as a function of d_F. Trivially, l_c and l_J should be as small as possible. Below we use $l_c{=}\ 200\,\mathrm{nm}$ and $l_J = 400\,\mathrm{nm}$. From simulations, using 3DMLSI with $\lambda_L = 350\,\mathrm{nm}$[38], we find the parametrization $L_c(w_c, d_F, l_c) \approx L'{\cdot}l_c/(w_cd_F)$, where $L'{=}\,155\,\mathrm{pH{\cdot}nm}$. This expression fits the simulated L_c well in the range $40\,\mathrm{nm} < w_c < 200\,\mathrm{nm}$, $40\,\mathrm{nm} < d_F < 500\,\mathrm{nm}$. We use the same functional dependencies for the SQUID arms containing a junction, and further $L_r = L_{r0}/(d_F/50\ \mathrm{nm})$. Below, we use $L_{r0} = 1\,\mathrm{pH}$. Then $L = L_c(w_c, d_F, l_c){+}2L_c(w_J, d_F, l_J){+}L_r(d_F)$, which can be solved self-consistently, yielding values for L and w_J.

With 3DMLSI we further calculated ϕ_μ at a distance of 10 nm above the constriction (without an Au layer) in the range $40\,\mathrm{nm} < w_c$, $d_F < 200\,\mathrm{nm}$ and find the dependence $\phi_\mu \approx \gamma_\mu(w_0/w_c)^{0.7}\cdot(12.3 + d_0/d_F)$, with $d_0 = 320\,\mathrm{nm}$, $w_0 = 1\,\mathrm{nm}$ and $\gamma_\mu = 23\,\mathrm{n}\Phi_0/\mu_B$.

Figure 5 shows s_μ vs β_{L0} for various values of d_F. All curves exhibit a shallow minimum near $\beta_{L0} = 0.78$. Further, in the range shown s_μ simply decreases with increasing d_F. In other words, one should make d_F as large as possible, respecting technological constraints. A value around 300 nm may be reasonable. Then, for $d_F = 300\,\mathrm{nm}$, $l_J = 400\,\mathrm{nm}$, $w_c = 50\,\mathrm{nm}$, $l_c = 200\,\mathrm{nm}$ we obtain

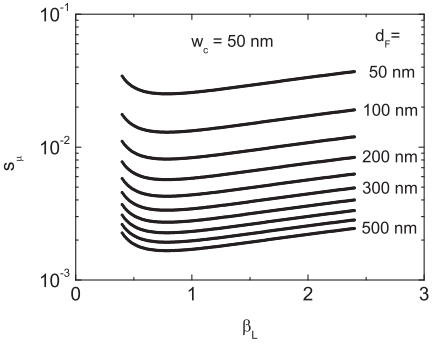

FIG. 5. Reduced spin sensitivity s_μ, used for optimizing the YBCO nanoSQUID, as a function of β_{L0} for 10 values of film thickness d_F, with $\Delta d_F = 50\,\mathrm{nm}$. The width of the constriction was set to 50 nm. Other parameters are $\lambda_L = 350\,\mathrm{nm}$, $l_c = 200\,\mathrm{nm}$, $l_J = 400\,\mathrm{nm}$.

$w_J = 417\,\mathrm{nm}$, $L = 3.22\,\mathrm{pH}$, $L_c = 2.07\,\mathrm{pH}$, $L_J = 0.49\,\mathrm{pH}$, $L_r = 0.17\,\mathrm{pH}$ and $s_\mu = 3.3{\cdot}10^{-3}\ \mathrm{pHnm}^{-1/2}(\mathrm{n}\Phi_0/\mu_B)^{-2}$.

We further obtain $I_0 = 250\,\mu\mathrm{A}$ and estimate $C \approx 25\,\mathrm{fF}$. Then, with $\beta_{C0} = 0.7$, we find $R \approx 6\,\Omega$ and $I_0R \approx 1.5\,\mathrm{mV}$. At $T = 4.2\,\mathrm{K}$ this would correspond to $S_\Phi^{1/2} \approx 21\ \mathrm{n}\Phi_0/\mathrm{Hz}^{1/2}$. For ϕ_μ one obtains $19.9\,\mathrm{n}\Phi_0/\mu_B$ and, finally, $S_\mu^{1/2} \approx 1\,\mu_B/\mathrm{Hz}^{1/2}$.

This is a drastic improvement, compared to $S_\mu^{1/2}$ of our (non-optimized) experimental device. Let us thus investigate and discuss the main factors entering the spin sensitivity.

Let us first look at ϕ_μ. Note that due to the counterbalancing effects of a 2 times smaller constriction width w_c and a 6 times higher film thickness d_F on the coupling factor ϕ_μ the values obtained for our experimental device and our optimized sample are almost identical. We should also note here, that some uncertainty determining ϕ_μ arises from the fact, that $d_F = 6w_c$ in our calculations. 3DMLSI uses supercurrents that flow only within a 2D layer. We have chosen a film thickness comparable to λ_L, so that this restriction will have no drastic consequences in the SQUID regions that have a large width e.g. for the SQUID arms containing the junctions). However, in the constriction region there may be a nontrivial 3D current flow. 3DMLSI predicts a saturation of ϕ_μ, which may not be correct – in other words we would not be surprised if the real ϕ_μ is different by a factor of 2 or so for the aspect ratio chosen. On the other hand, it is possible to thin the YBCO film in the region of the constriction.

The main improvement of $S_\mu^{1/2}$ comes from $S_\Phi^{1/2}$. Before discussing the various factors improving this quantity, we should say, however, that even the best YBCO SQUIDs are known to have a S_Φ, which is a factor of 2 or so higher than the theoretical predictions[34] (for the experimental device discussed above S_Φ was even a factor 6 higher than predicted by Eq.1). In this respect we expect the theoretical $S_\Phi^{1/2}$ to be by a factor ~ 2–10 too low, even if all factors entering $S_\Phi^{1/2}$ are feasible. One major improvement of $S_\Phi^{1/2}$ arises from the total SQUID inductance L, which is an order of magnitude lower than the inductance of our experimental device. This is because of the much larger value of d_F, but also because we have made the lengths of the constriction and junction arms smaller. The low value of L seems realistic, provided that 300 nm thick YBCO films can be patterned properly. In terms of geometrical factors, $w_c = 50\,\mathrm{nm}$ and lengths l_c and l_J of the constrictions and the SQUID arms containing the junctions are chosen sportive, but not impossible. Another big improvement of $S_\Phi^{1/2}$ comes from the optimized value of I_0R, which is by a factor of 11 higher than that of our experimental device. For narrow ($w_J \sim 100\,\mathrm{nm}$) and thin ($d_F \sim 50\,\mathrm{nm}$) junctions this would be impossible to achieve. However, the optimization yielded wide ($w_J \sim 500\,\mathrm{nm}$) and thick ($d_F \sim 300\,\mathrm{nm}$) junctions, where we indeed expect, that large values of I_0R are feasible. YBCO grain boundary junctions not shunted by gold layers are hysteretic at low temperatures (i.e., $\beta_C > 1$). Thus, moderate shunting should allow for the value $\beta_C = 0.7$ used for the optimization and also should allow for an I_0R product of 1.5 mV.

Finally, we note that, if we take more easily achievable values $d_F = 200\,\mathrm{nm}$ and $w_c = 100\,\mathrm{nm}$ (other input parameters are the same as for the initial optimization), we still get $S_\mu^{1/2} = 1.6\ \mu_B/\mathrm{Hz}^{1/2}$, and the parameter values $w_J = 777\,\mathrm{nm}$, L= 1.6 pH, $I_0R = 1.2\,\mathrm{mV}$, $R = 4.0\,\Omega$. The resulting $S_\mu^{1/2}$ is less than a factor of 2 different from the value obtained for the initial input parameters, so that we are optimistic that the design discussed in this paper is indeed capable to obtain a spin sensitivity in the range of a few $\mu_B/\mathrm{Hz}^{-1/2}$.

In summary we have investigated the noise performance of a YBCO nanoSQUID in magnetic fields up to 1 T. The design incorporates a 90 nm wide constriction which was used to modulate the flux through the SQUID loop. At zero applied field the white flux noise of the device at 7 kHz was $1.3\,\mu\Phi_0/\mathrm{Hz}^{1/2}$, increasing to $2.3\,\mu\Phi_0/\mathrm{Hz}^{1/2}$ at 1 T. For the spin sensitivity, assuming that a small particle is placed onto the constriction directly on top of the YBCO film, we calculated values of $62\,\mu_B/\mathrm{Hz}^{1/2}$ at $B = 0$ and of $110\,\mu_B/\mathrm{Hz}^{1/2}$ at 1 T. The device investigated experimentally was not optimized yet in terms of its geometrical and electrical parameters. Such an optimization predicts a spin sensitivity of a few $\mu_B/\mathrm{Hz}^{1/2}$. It remains to be shown whether or not such values can be achieved in high fields.

ACKNOWLEDGMENTS

J. Nagel and T. Schwarz acknowledge support by the Carl-Zeiss-Stiftung. This work was funded by

the Deutsche Forschungsgemeinschaft (DFG) via the SFB/TRR 21.

[1] D. Gatteschi and R. Sessoli, Angew. Chem., Int. Ed. **42**, 268 (2003).

[2] L. Bogani, A. Vindigni, R. Sessoli, and D. Gatteschi, J. Mater. Chem. **18**, 4750 (2008).

[3] J. Fortágh and C. Zimmermann, Science **307**, 860 (2005).

[4] P. Bushev, D. Bothner, J. Nagel, M. Kemmler, K. B. Konovalenko, A. Loerincz, K. Ilin, M. Siegel, D. Koelle, R. Kleiner, and F. Schmidt-Kaler, Eur. Phys. J. D **63**, 9 (2011).

[5] D. Rugar, R. Budakian, H. J. Mamin, and B. W. Chui, Nature **430**, 329 (2004).

[6] J. R. Maze, P. L. Stanwix, J. S. Hodges, S. Hong, J. M. Taylor, P. Cappellaro, L. Jiang, M. V. Gurudev Dutt, E. Togan, A. S. Zibrov, A. Yacoby, R. L. Walsworth, and M. D. Lukin, Nature **455**, 644 (2008).

[7] G. Balasubramanian, I. Y. Chan, R. Kolesov, M. Al-Hmoud, J. Tisler, C. Shin, C. Kim, A. Wojcik, P. R. Hemmer, A. Krueger, T. Hanke, A. Leitenstorfer, R. Bratschitsch, F. Jelezko, and J. Wrachtrup, Nature **455**, 648 (2008).

[8] L. T. Kuhn, A. K. Geim, J. G. S. Lok, P. Hedegård, K. Ylänen, J. B. Jensen, E. Johnson, and P. E. Lindelof, Eur. Phys. J. D **10**, 259 (2000).

[9] O. Kazakova, V. Panchal, J. Gallop, P. See, D. C. Cox, M. Spasova, and L. F. Cohen, J. Appl. Phys. **107**, 09E708 (2010).

[10] W. Wernsdorfer, Adv. Chem. Phys. **118**, 99 (2001).

[11] L. Hao, C. Aßmann, J. C. Gallop, D. Cox, F. Ruede, O. Kazakova, P. Josephs-Franks, D. Drung, and T. Schurig, Appl. Phys. Lett. **98**, 092504 (2011).

[12] S. K. H. Lam, J. R. Clem, and W. Yang, Nanotechnol. **22**, 455501 (2011).

[13] V. Bouchiat, Supercond. Sci. Technol. **22**, 064002 (2009).

[14] M. Faucher, P.-O. Jubert, O. Fruchart, W. Wernsdorfer, and V. Bouchiat, Supercond. Sci. Technol. **22**, 064010 (2009).

[15] M. E. Huber, N. C. Koshnick, H. Bluhm, L. J. Archuleta, T. Azua, P. G. Björnsson, B. W. Gardner, S. T. Halloran, E. A. Lucero, and K. A. Moler, Rev. Sci. Instr. **79**, 053704 (2008).

[16] J.-P. Cleuziou, W. Wernsdorfer, V. Bouchiat, T. Ondarçuhu, and M. Monthioux, Nature Nanotechnology **1**, 53 (2006).

[17] S. K. H. Lam and D. L. Tilbrook, Appl. Phys. Lett. **82**, 1078 (2003).

[18] A. G. P. Troeman, H. Derking, B. Borger, J. Pleikies, D. Veldhuis, and H. Hilgenkamp, Nano Lett. **7**, 2152 (2007).

[19] P. F. Vohralik and S. K. H. Lam, Supercond. Sci. Technol **22**, 064007 (2009).

[20] C. Granata, E. Esposito, A. Vettoliere, L. Petti, and M. Russo, Nanotechnology **19**, 275501 (2008).

[21] A. Finkler, Y. Segev, Y. Myasoedov, M. L. Rappaport, L. Neeman, D. Vasyukov, E. Zeldov, M. E. Huber, J. Martin, and A. Yacoby, Nano Lett. **10**, 1046 (2010).

[22] N. C. Koshnick, M. E. Huber, J. A. Bert, C. W. Hicks, J. Large, H. Edwards, and K. A. Moler, Appl. Phys. Lett. **93**, 243101 (2008).

[23] C. P. Foley and H. Hilgenkamp, Supercond. Sci. Technol. **22**, 064001 (2009).

[24] R. F. Voss, R. B. Laibowitz, and A. N. Broers, Appl. Phys. Lett. **37**, 656 (1980).

[25] J. Nagel, O. F. Kieler, T. Weimann, R. Wölbing, J. Kohlmann, A. B. Zorin, R. Kleiner, D. Koelle, and M. Kemmler, Appl. Phys. Lett. **99**, 032506 (2011).

[26] L. Chen, W. Wernsdorfer, C. Lampropoulos, G. Christou, and I. Chiorescu, Nanotechnol. **21**, 405504 (2010).

[27] R. Kleiner, D. Koelle, F. Ludwig, and J. Clarke, Proc. IEEE **92**, 1534 (2004).

[28] K. Takeda, H. Mori, A. Yamaguchi, H. Ishimoto, T. Nakamura, S. Kuriki, T. Hozumi, and S. ichi Ohkoshi, Rev. Sci. Instr. **79**, 033909 (2008).

[29] J. Nagel, K. B. Konovalenko, M. Kemmler, M. Turad, R. Werner, E. Kleisz, S. Menzel, R. Klingeler, B. Büchner, R. Kleiner, and D. Koelle, Supercond. Sci. Technol. **24**, 015015 (2011).

[30] SQ100 LTS dc SQUID, PC-100 Single-Channel dc SQUID Electronics System, STAR Cryoelectronics, USA.

[31] W. C. Stewart, Appl. Phys. Lett. **12**, 277 (1968).

[32] D. McCumber, J. Appl. Phys. **39**, 3113 (1968).

[33] C. D. Tesche and J. Clarke, J. Low Temp. Phys. **29**, 301 (1977).

[34] D. Koelle, R. Kleiner, F. Ludwig, E. Dantsker, and J. Clarke, Rev. Mod. Phys. **71**, 631 (1999).

[35] J. Clarke and A. I. Braginski, The SQUID Handbook, 1st ed. (Wiley-VCH, 2004) ISBN 3527402292.

[36] M. Khapaev, M. Kupriyanov, E. Goldobin, and M. Siegel, Supercond. Sci. Technol. **16**, 24 (2003).

[37] A. Beck, O. Froehlich, D. Koelle, R. Gross, H. Sato, and M. Naito, Appl. Phys. Lett. **68**, 3341 (1996).

[38] For YBCO SQUIDs, 3DMLSI is known to predict too low inductances if a proper value for λ_L ($\approx 180\,\mathrm{nm}$) is used. The reason is unclear but may have to do with the layered structure and anisotropy of YBCO. In our simulations we have increased λ_L to be consistent with the experimentally determined values of L.